

Copyright

by

Paul Michael Haney

2007

The Dissertation Committee for Paul Michael Haney
certifies that this is the approved version of the following dissertation:

**Spintronics in Ferromagnets and Antiferromagnets
From First Principles**

Committee:

Allan Hugh MacDonald, Supervisor

Maxim Tsoi

Alex Demkov

Zhen Yao

Peter Rossky

**Spintronics in Ferromagnets and Antiferromagnets
From First Principles**

by

Paul Michael Haney, B.S.

Dissertation

Presented to the Faculty of the Graduate School of

The University of Texas at Austin

in Partial Fulfillment

of the Requirements

for the Degree of

Doctor of Philosophy

The University of Texas at Austin

August 2007

For my parents.

Acknowledgments

I would like to express my heartfelt gratitude to my advisor Allan MacDonald. I was fortunate to have learned how to approach physics from one of the very best. He has always shown me and everyone else an extraordinary degree of patience, kindness, and humor. He always showed a belief in me, and opened many doors of opportunity for me, which is all that anyone can ask for. I have had the pleasure of working with many others along the way. I would like to specifically thank Hong Guo of McGill University, whose enthusiasm and support helped ease my introduction to first principles methods, Joaquín Fernández-Rossier of University of Alicante, whose collaboration formed the seeds of all the work contained here, and Olle Heinonen of Seagate, who showed me how physics is practiced in the “real world”. I look back on my time in Alicante, Montreal, and Minneapolis with great fondness. Thanks as well goes to Maxim Tsoi, who always took the time to explain things from an experimentalist’s point of view.

I must also acknowledge several fellow students: Alvaro Núñez, who helped to blaze the trail followed in this work, Derek Waldron, mastermind of code development who showed me how computer science is really done, and Rembert Duine, a great friend who taught me both about physics and death metal. I also thank my dear friend Sandra Nashif for her support - our conversations over dinner were the perfect respite from the long days of work.

Thanks to Becky Drake for all of her patience and help. Without significant

help in tackling the administrative tasks of graduate school, I'm not sure if I would have been kicked out after the first week, or remained at UT forever.

Finally, I would like to thank my family and parents. This work was made possible by their unwavering support, along with the periodic admonition to “work hard, boy.”

PAUL MICHAEL HANEY

The University of Texas at Austin

August 2007

Spintronics in Ferromagnets and Antiferromagnets

From First Principles

Publication No. _____

Paul Michael Haney, Ph.D.
The University of Texas at Austin, 2007

Supervisor: Allan Hugh MacDonald

In nanoscale magnetic metals, transport properties like the conductance depend on the magnetic configuration of the structure, an effect known as giant magnetoresistance. Conversely, electron transport can induce changes in the magnetic configuration through an effect known as spin transfer. These two effects underlie the field of magnetic metal spintronics. In this thesis, these effects are studied from an ab-initio perspective.

A general microscopic theory of spin transfer is implemented in an ab-initio formalism. The view of this phenomena developed and exploited in this thesis is one in which transport quasiparticles near the Fermi energy influence the collective

behavior of states far from the Fermi energy, and in particular their total spin magnetization.

The microscopic picture of the influence of transport currents on magnetic configurations, in which they lead to effective torques which act on each orbital of each atom, is the principle original contribution of the research reported on in this thesis. The technical nonequilibrium Green's function + density functional theory implementation necessary to apply this idea to real materials is a second important achievement. The idea that giant magnetoresistance and current-induced spin-torques occur in antiferromagnetic metals, and the exploration of some of the consequences of this idea is the most important result which has so far emerged from this research effort.

As far as the specific systems considered in this work, we first study a ferromagnetic spin valve structure composed of Co magnetic layers separated by Cu spacers. The spin torque per current is found in the ballistic and diffusive regimes and compared to experimental values. We next consider an antiferromagnetic spin valve, with antiferromagnetic Cr layers separated by a Au spacer, and find nonzero magnetoresistance and spin transfer torques. Finally we consider a system with ferromagnetic Co adjacent to antiferromagnetic NiMn. We find a qualitatively new form of spin transfer for this system, and predict that unusual magnetic configurations will occur under the action of this novel form of spin transfer torque.

Contents

Acknowledgments	v
Abstract	vii
List of Figures	xiv
Chapter 1 Introduction	1
1.1 Spintronics	3
1.2 Outline of thesis	4
Chapter 2 Spintronics	6
2.1 Introduction	6
2.2 Metallic magnetism	8
2.3 Magnetoresistance	10
2.3.1 Giant magnetoresistance	10
2.3.2 Tunnelling magnetoresistance	14
2.3.3 Molecular GMR	16
2.4 Spin transfer	17
2.5 Exchange bias	18
2.5.1 Meiklejohn and Bean - direct exchange	19

Chapter 3	Transport in Mesoscopic Systems	21
3.1	Introduction	21
3.2	Landauer	23
3.3	From Landauer to Boltzmann.	27
3.4	The scattering matrix	28
3.4.1	Scattering matrices and interface resistance	30
3.5	Conductance of materials in the diffusive regime	31
Chapter 4	Keldysh	36
4.1	Green's functions in equilibrium systems	36
4.2	Nonequilibrium Green's function	41
4.3	Application to the 2-probe geometry	46
4.4	Implementation	52
4.4.1	Boundary conditions	52
4.4.2	Self-energy calculation	54
4.4.3	Calculating the transmission	57
Chapter 5	Density Functional Theory	58
5.1	Introduction	58
5.2	General formulation - Hohenberg Kohn theorem	59
5.2.1	Kohn-Sham equations	62
5.2.2	Total energy	64
5.2.3	Local density approximation	65
5.3	Pseudopotential approximation	66
5.3.1	Seperable pseudopotentials	71
5.3.2	Addition of screening potentials	71
5.4	Basis set: Linear Combination of Atomic Orbitals	72
5.5	Solution of Kohn-Sham Equations	75

5.5.1	The density matrix	75
5.5.2	Periodic systems	76
5.5.3	Self-consistent procedure	78
5.6	Exchange-correlation functionals	78
5.6.1	LSDA	78
5.6.2	Non-collinear spin	79
Chapter 6 Spin Transfer		82
6.1	Introduction	82
6.2	Spin dynamics: The Landau-Lifshitz equation.	83
6.3	Phenomenology of spin dynamics in the presence of current	86
6.3.1	Spin torques and spin fluxes in FM	88
6.3.2	Current induced magnetization switching	92
6.4	Microscopic theory of spin dynamics	92
6.4.1	Adiabatic approximation	94
6.5	Equilibrium dynamics - stiffness calculation	96
6.5.1	Torque method for stiffness	98
6.6	Nonequilibrium dynamics - STT calculation	101
6.6.1	Nonequilibrium torques and spin current fluxes	102
6.7	Implementation	105
Chapter 7 Spin Torques in Ferromagnetic Metal structures		107
7.1	Introduction	107
7.2	Calculation details	108
7.3	Co-Cu-Co trilayer	111
7.3.1	STT in Co-Cu-Co trilayers	113
7.4	Ballistic vs Diffusive calculations	116
7.5	Ballistic calculation - 2 vs 3 interface results	121

7.6	Dual Spin Filter	124
Chapter 8 Spintronics in Antiferromagnets		128
8.1	Introduction	128
8.2	Antiferromagnets - general properties	129
8.3	GMR and CIT in an AFM - toy model approach	130
8.3.1	General properties	130
8.3.2	AGMR in toy model	132
8.3.3	CIT in AFM toy model	133
8.4	GMR and CITs in Cr-Au-Cr	136
8.4.1	System details	136
8.4.2	AGMR in Cr-Au	139
8.4.3	CIT in Cr-Au	144
Chapter 9 Spin Torques Between FM and AFM layers.		148
9.1	Introduction	148
9.2	NiMn-Co – Equilibrium properties	149
9.2.1	General properties	150
9.2.2	Spin transfer torques in AFM-FM system	151
9.3	Effect of $\sin 2\theta$ torque in single domain magnetics	155
9.4	Effect on switching field	166
9.4.1	Effect on exchange bias model	167
9.4.2	Effect of current on uniform spin distribution	168
9.4.3	Direct torque on FM	172
9.5	AGMR in compensated AFM systems	174
Chapter 10 Conclusion.		177
Appendices		179

Appendix A Exchange-Correlation Parameterizations	180
Appendix B Derivations for equilibrium and nonequilibrium spin torques	182
B.1 Exchange parameters from energy and torques.	182
B.2 Spin current operator	184
B.2.1 Spin-dependent hopping	186
Appendix C Toy scattering formulation	189
Appendix D Stability analysis of Landau Lifshitz equation	192
Bibliography	194
Vita	204

List of Figures

2.1	Schematic of a spin valve. The AFM layer pins the fixed layer's orientation with the exchange bias effect.	11
2.2	History of magnetic storage density with key innovations labelled. Inset shows total capacity of hard drives shipped per year. Fig. taken from Ref. [1], CGR stands for "compound growth rate", AFC is "antiferromagnetically coupled media", which represents an improvement in recording media design not of interest to us here.	13
2.3	Schematic of the two channel model of GMR. The boxes labelling $R_{\uparrow/\downarrow}$ represent the spin-dependent resistance of a ferromagnet-normal metal interface.	14
2.4	A schematic for the electronic structure of a Co-Cu spin valve	15
2.5	Julliere's model of TMR. In this model TMR is due to spin-dependent density of states the the Fermi level.	16
2.6	Cartoon showing spin transfer torque. The electron spin enters the free ferromagnet point up, and is rotated by the magnetization so that it leaves in a different direction. Spin transfer is the back-action torque on the magnetization by the electron spin.	19

2.7	Geometry in direct exchange model: (a) is a low energy configuration, while (b) is a high energy configuration. The difference in energy leads to unidirectional anisotropy for the FM, or exchange bias.	19
3.1	Length scales relevant for mesoscopic systems. Figure adapted from Ref. [2].	22
3.2	2-probe geometry. Here $\mu_L > \mu_R$, and the circle in the conducting wire represents some static scatterer.	24
3.3	Incoming and outgoing states scattering off a generic potential. . .	29
3.4	Equivalent circuit model for trilayer calculation. The “resistors” represent the interfaces.	33
4.1	The Keldysh contour.	42
4.2	Physical interpretation of the retarded Green’s function with the leads represented by self energies. The factors of the second term correspond to hopping from i to j while making excursions into the left lead, shown by the arrows in the picture.	50
4.3	Contour integration for the Green’s function. In the complex plane, the integral is evaluated using Gaussian quadrature with 20-40 points, while the nonequilibrium portion is evaluated along the real axis. . .	52
4.4	Atomic positions at a Cr-Au interface. The grey and black circles represent Au and Cr atoms, respectively. The interface is assumed to be flat, and transverse periodic boundary conditions are used. . . .	53
4.5	Energy shifts of bulk leads and the ensuing charge transfer in 2-probe geometry, for a system of semi-infinite Cr adjacent to semi-infinite Au.	55
4.6	Charge density through a slice of real space for Cr-Au system. The black dotted lines indicate the system-lead boundaries, and indicate that the charge density is continuous at the boundary.	56

5.1	Steps in construction of the pseudopotential (shown for the $l = 0$ channel only). (1.) Find the $l = 0$ all electron (AE) orbital. (2.) Construct the pseudo-orbital according to procedure outlined in text. (3.) Find the resulting potential. (4.) Remove valence (and core) electron contributions from potential.	67
5.2	Schematic of the self-consistent cycle.	79
6.1	A typical trajectory of a monodomain switching event.	85
6.2	Cartoon of Néel Domain Wall.	86
6.3	Schematic for scattering problem of \hat{x} spinor incident on a ferromagnet with orientation in \hat{z} -direction.	89
6.4	Current carrying electron spin. On the left it precesses around the magnetization. The right figure shows the total spin after averaging over all current carrying states. In this case the transverse component decays to 0.	90
6.5	Cartoon showing spin transfer torque. The electron spin enters the free ferromagnet point up, and is rotated by the magnetization so that it leaves in a different direction. Spin transfer is the back-action torque on the magnetization by the electron spin.	91
6.6	Illustration of current induced magnetization switching. The orientation of the free (thinner) FM layer is opposed to the applied field because of spin transfer torque.	93
6.7	Tilting one atomic plane by θ of a uniform, infinite, bulk system. . .	96
6.8	Illustration of Eq. (6.39), relating spin current fluxes to local spin precession.	104
6.9	Spin current and spin fluxes in Co-Cu-Co-Cu system, with $\theta = 90^\circ$. .	106
7.1	Density of states for Co and Cu.	109

7.2	Transmission as a function of transverse wave vector. The majority channel shows almost uniform transmission, while the minority channel shows a complicated structure.	110
7.3	Coordinates used in trilayer (2-interface) calculation.	111
7.4	Conductance per area vs. relative layer orientation for the Co-Cu-Co trilayer. A magnetoresistance of 30% is obtained. The data labelled “from AP” represent configurations obtained by rotating away from the collinear anti-parallel ground state.	112
7.5	Polarization and direction of spin current versus relative layer orientation. The angle of the spin current in the spacer is $\theta/2$. $p(\pi) = 0$ as required by symmetry.	113
7.6	Geometric illustration of the spin current orientation in the spacer and relative layer orientation. If the polarization is assumed to be independent of θ , the increase of efficiency with θ follows simply from this geometrical consideration.	114
7.7	Spin transfer efficiency g for NEGF calculation, and Slonczewski and simple estimate formulas.	116
7.8	Equivalent circuit model for trilayer calculation. The “resistors” represent the interfaces.	117
7.9	Angular magnetoresistance for two models: NEGF (ballistic) and spin circuit theory (diffusive). The Schep magnetoresistance is larger due to its omission of contact resistance.	118
7.10	Polarization P and spin transfer g vs θ for diffusive and ballistic regimes. The initial decrease of p_{diff} causes g_{diff} to decrease monotonically.	120
7.11	Coordinates used in 3 interface calculation.	121

7.12	Conductance per area and polarization for 2-interface (trilayer) and 3-interface systems. As expected, the conductance is reduced and polarization increased for the 3-interface system. Also, the polarization does not decay to 0 for 3-interface AP configuration.	122
7.13	Transmission function for single interface vs. 2 interfaces. The 2 interface case is for parallel Co alignment.	123
7.14	2 vs 3 interface transmission along the k -space line $k_y = 0, k_x \in [0, \pi]$. The 3 interface case shows a structure related to resonant reflection.	124
7.15	Spin transfer per current versus angle, and spin transfer efficiency vs. angle for 2-3 interface systems. The spin torque is generally larger for the 3 interface case, because of the larger polarization.	125
7.16	Schematic showing the resonant behavior present in the majority channel in the AP configuration. This leads to a $T_{\downarrow} > T_{\uparrow}$ in the AP configuration.	125
7.17	Spin current angle in the spacer vs. relative orientation for 2 and 3-interfaces. The larger angle of the 3-interface system is a consequence of resonant reflection in the majority channel.	126
7.18	Coordinates of the DSF stack configuration.	126
7.19	Spin transfer torque and efficiency for 2,3 interface systems and DSF system. As expected, the DSF system shows considerable enhancement of STT efficiency.	127
7.20	Layer resolved spin torques for DSF stack. The spin torques are localized at both interfaces of the free layer, and act cooperatively to increase the spin transfer efficiency.	127
8.1	Cartoon of N-AFM-N-AFM-N antiferromagnetic spin valve. This configuration would be labelled “Parallel”, as described in the text.	133
8.2	AGMR vs. spacer length for a single band 2-d toy model.	134

8.3	For (a): spin densities for N-AFM-N-AFM-N structure. Here $E_f = 2 \cos(.1)$, $U/t = .1$, and only single-channel is calculated. For (b): Out-of-plane spin densities (spin transfer torques) present in a AFM-FM-N-FM structure, similar to that used for exchange bias. For the data shown $E_f = 2 \cos(.5)$, $U/t = .01$, and transverse channels included.	136
8.4	GMR as a function of spacer thickness. There is a sizable GMR for all spacer thicknesses. The inset shows the geometry for the four layer spacer configuration - up and down spins are colored red and blue (light and dark), respectively. The configuration above illustrates an anti-parallel configuration.	138
8.5	Layer and spin resolved density of states at the Fermi energy for Cr-Au single interface system. Layers 1-12 are Cr, and 13-24 are Au. The pronounced enhancement of the density-of-states in layer 12 reflects the interface resonance. The spin-polarization of the interface resonance is consistent with the fact that $T_{\downarrow} > T_{\uparrow}$ in the transport calculation.	140
8.6	Number of propagating states in the [001] direction at the Fermi energy for bulk antiferromagnetic Cr.	141
8.7	Number of propagating states in the [001] direction at the Fermi energy for bulk antiferromagnetic Cr.	143
8.8	Density of states at the fermi energy in the Brillouin zone for layers 10-14of the single interface Cr-Au system. The DOS relaxes to its bulk shape a couple of layers away from the interface.	144
8.9	Layer resolved current induced torque per current. The (X,Y,Z) directions in the legend refer to the directions of the induced torques. The solid arrows in the figure refer to the orientation of the Cr interface spin. The torque is localized in the first layer of the Cr.	147

9.1	Coordinates and spin structure for Co-NiMn interface.	149
9.2	Magnetic moment on each sublattice. Layer 12 is terminating Ni layer of NiMn. The vertical lines labelled “A, B, and C” represent choices of planes which subdivide the system, as explained in the text. . . .	150
9.3	Illustration of the need for torques to differ by sign on the A and B sublattices in order to rotate the AFM moment. The torques are shown with gray arrows. For current from FM to AFM, the torque pulls the AFM axis toward the FM, and the FM perpendicular to the AFM axis.	152
9.4	Spin torque per current on FM and AFM layers for compensated interface.	153
9.5	Cartoon showing the spin transfer torques present in a compensated AFM - FM interface. (a) The presence of the ferromagnet leads to spin-polarized current and STT for small θ . (b) At $\theta = 90^\circ$, the current’s spin polarization is due only to the FM, as seen from symmetry considerations, and there is no torque. (c) For $\theta > 90^\circ$, the sign of current polarization and spin transfer torque changes. . .	154
9.6	Torques on sublattices A and B vs. layer, for several different relative orientations.	155
9.7	Torques on the first two layers of Mn. On the first layer, the torques cooperate, while on the second layer, they cancel each other.	156
9.8	Torques vs. angle on FM and AFM layer for different choices of system cuts. An interface with compensated moment (cuts A and B) shows a $\sin 2\theta$ behavior, while an interface with uncompensated moment (cut C) shows a more $\sin \theta$ behavior.	157

9.9	System to consider the implications of $\sin 2\theta$ torque. The field and AFM axis point in the \hat{z} -direction, and the hard axis is in the \hat{x} -direction.	157
9.10	Coordinates used for magnetic orientation and torques.	159
9.11	Magnetic configuration (M_x, M_z) and peak of power spectrum P_z (arbitrary units) versus applied field and current. Also shown is stability boundaries found analytically (the labels $\pm x, \pm z$ refer also to solutions which point approximately in these directions). The stability boundary plot also shows the reduced out-of-plane solution space for negative to positive field sweep with a dashed line.	163
9.12	Saddle shape shows the out of plane torque vs β for small excursions from the $y - z$ plane. The torque is always positive.	164
9.13	For a uniform distribution of spin orientations spanning $\theta \in [-\beta, +\beta]$, the average \hat{z} -component is $(\sin \beta)/\beta$, plotted above.	168
9.14	Numerical check of the solution to LL+Slonczweski equation with tilted pinning field. The black squares indicate the stability boundary determined analytically.	169
9.15	(A) Set of switched moments are shown in darker gray for a given distribution and $B_{st} > 0$. (b) Dark gray shows set of switched moments for $B_{st} < 0$; here only moments sufficiently close to $\theta = \pi$ undergo switching.	170
9.16	(a) Ratio of $\langle M_z \rangle / \langle M_z^0 \rangle$ vs. B_{st}/B_{pin} for 3 moment distributions - a value of +1 signifies no change to exchange bias, and -1 signifies a reversed exchange bias orientation. (b) shows a contour plot of $\langle M_z \rangle / \langle M_z^0 \rangle$ vs B_{st}/B_{pin} and β	171
9.17	M_z vs applied field and current, for forward and backward field sweeps.	173

9.18	Illustration of the role of STT for field-induced magnetization switching of an easy plane FM: STT can assist the switching, reducing the switching field; however STT can not retard switching.	173
9.19	Hysteresis loops for several values of spin transfer torque. Only 1 branch is shifted by the spin transfer torque.	174
9.20	The lattice structure of the NiMn-Cu-NiMn system. There are 6 ML of Cu (atoms not shown explicitly), and the terminating Mn layers 2d lattices are offset in real space, as shown.	175
9.21	Conductance vs. relative orientation for two compensated antiferromagnets. The conductance is minimized (or resistance maximized) for $\theta = 0, 90, 180$. The difference in conductance is likely due to phase-coherent effects.	176
B.1	Spin-dependent noncollinear hopping between two sites i and $i + 1$. The spin is rotated by the “hopping” effective magnetic field (points into the page).	188
B.2	Spin-dependent noncollinear hopping between two sites i and $i + 1$. When you reverse the labels of “source” and “target”, the sign of the current changes, but in this case, the sense of rotation of the spin changes as well. This is the source of the violation of $I_L = -I_R$. The difference is usually very small.	188
C.1	Unit cell of antiferromagnet (shown for up spin, the down spin has opposite signs for U .)	191

Chapter 1

Introduction

The discovery of quantum mechanics in the early twentieth century revolutionized the way we think about matter at atomic length scales. Although motivated primarily by experiments in atomic physics, the quantum theory was soon applied to assemblies of many atoms in molecules and in crystals. The description of matter in the solid state follows in principle directly from the many-particle Schrödinger equation. When written down in the 1920's, the Schrödinger equation provided a theory of everything for condensed matter physics. From a strict reductionist point of view, the description of condensed matter physics is thus complete. This point of view is exemplified by Carl Anderson, who declared after the discovery of the positron that “the rest is chemistry!” Of course such characterizations are hardly serious, and the unreduced problem as it stands is so utterly intractable that, in the words of Walter Kohn, “its solution is not a legitimate scientific concept”¹. Dirac made the point with characteristic understatement: “the underlying physical laws for the mathematical theory of a large part of physics and the whole of chemistry are thus completely known, and the difficulty is only that the exact application of these laws leads to equations much too complicated to be soluble.”

¹Kohn characterizes a solution Ψ to be “legitimate” if it can be both calculated and recorded with sufficient accuracy - a criterion a many-body wave function for $N > 10^3$ does not meet.

Despite this difficulty, condensed matter theory has enjoyed much success in describing the properties of bulk materials, in both their mundane and exotic forms. The underlying reasons for its success despite the apparent complexity of the problem are explained in part from the concept of the quasiparticle and of the collective coordinate, described below.

The source of difficulty associated with the many-body Schrödinger equation is the electron-electron interaction. The easiest way to deal with this difficulty is to simply ignore it. True to their pragmatic spirit, this approach was adopted by physicists from the beginning for its simplicity and its apparent ability to provide a reasonable description of experimental properties. It was put on more solid theoretical ground with the formulation of by Landau's formulation of the Fermi liquid theory which bears his name. Although electron-electron interactions can be large in strength, they have little effect on excitations from the ground state for most systems due to phase space considerations [3]. They do however lead to a modification of the pure single-particle picture, which is manifested in a renormalized electron mass and finite lifetime. This modified state is referred to as a quasi-particle, which although strictly speaking is a many-body state, can be handled with the ease of a single particle state.

The other central concept used in descriptions of condensed matter systems is that of a collective coordinate, often called an order parameter. In this case a macroscopic number of constituent particles condense into some symmetry-broken collective state, which can be described by a collective variable referred to as an order parameter. Common examples include superconductivity and ferromagnetism. The behavior of the ordered state is not described by the microscopic interactions which govern the behavior of the constituent particles. This ordered state is therefore emblematic of the notion of *emergence*, an idea described in the classic paper of Phil Anderson appropriately entitled "More is Different" [4].

1.1 Spintronics

The main topic of this thesis is magnetic metal spintronics, which in an elemental sense can be considered the study of the interaction between nonequilibrium quasiparticles and the collective order parameter of a magnetic broken-symmetry states. There are several recent examples of phenomena related to quasiparticle-order parameter interactions. For example, quantum Hall bilayers which develop excitonic condensates [5] under certain conditions and exhibit anomalies related [6] to the influence of transport currents on interlayer phase coherence. The interplay between charge density waves and transport currents has also been shown to affect both the current-voltage characteristics and the properties of the charge density wave order [7].

The most-studied example is the interaction between nonequilibrium quasiparticles and the magnetization of a ferromagnet. For ferromagnets, this interaction leads to two well-known effects: giant magnetoresistance and spin transfer. Both effects occur in circuits which contain ferromagnetic elements (typically multilayers of nanoscale dimension containing ferromagnet layers separated by nonmagnetic layers). In giant magnetoresistance there is a change in the resistance when the magnetic configuration of the ferromagnet changes. In general the resistance is smaller when the magnetic orientation is uniform than when the magnetic orientation is spatially varying. As we will discuss further later, this effect provides the basis for reading magnetically stored information. Spin transfer may be understood as the converse effect to GMR. In this case, the presence of a sufficiently large current can change the magnetic configuration of a ferromagnet. There is hope that this effect can be used to create nonvolatile magnetic random access memory (MRAM) [8].

In this thesis, we study these effects from a more general point of view, and consider their manifestation in novel magnetic systems such as antiferromagnets. Our picture of spin transfer is described in Ref. [9], and is advantageous in that it

does not rely on conservation of spin angular momentum, and can be implemented within density functional theory, discussed in Ch. (5). In this way, our calculations include all of the electronic structure details of the materials involved. These realistic calculations are valuable in that they indicate of the strength of these effects in unexplored materials, providing some measure of experimental guidance.

1.2 Outline of thesis

Here we give a preview of the material contained in this work and its organization:

Ch. (2) describes the basic physics of spintronics in ferromagnets. This gives context to our results on ferromagnetic systems, and provides a backdrop against which to contrast the novel features of spintronics in antiferromagnets.

Next we describe the machinery needed to consider spintronics in systems in a realistic way. It turns out we need a lot of machinery, and it is described in Ch. 3-6. The breakdown is as follows:

Ch. (3) describes our implementation of density functional theory. It is a standard implementation, and follows in the spirit of Ref. [10], but we include some of the details here in the hopes that this document will be useful as a background reference for future researchers.

Ch. (4) describes the physical picture of transport in mesoscopic systems in the ballistic regime, which is furnished by the Landauer-Buttiker theory of transport. We also briefly review a formalism known as “spin circuit theory” for treating transport in noncollinear magnetic systems in the diffusive regime. The spin-circuit theory is not fully microscopic and is complementary to the approach used in this thesis research.

Ch. (5) reviews the technical formalism employed to calculate ballistic transport, known as nonequilibrium Green’s functions.

Ch. (6) describes the formal details of our calculation of spin dynamics, in-

cluding equilibrium exchange interactions and nonequilibrium spin transfer torques. We include the calculation of exchange interactions in equilibrium despite the fact that they play no further role in remaining work, only to highlight the relationship between their calculation and that of spin transfer torques.

With that we have in place the machinery necessary to calculate magnetoresistance and spin transfer torques for realistic systems. We consider three types of systems: purely ferromagnetic (FM), purely antiferromagnetic (AFM), and hybrid AFM-FM over the next three chapters. Specifically:

Ch. (7) covers the calculation of spin transfer torques in a typical FM spin valve, consisting of Co FM layers separated by Cu spacers. This calculation serves as a benchmark which allows us to examine in some detail properties of the calculation method itself. We also contrast our results for the ballistic case with those obtained in the diffusive limit with spin circuit theory.

Ch. (8) considers the spintronic effects present in antiferromagnetic systems. At first we discuss an AFM spin valve. We'll first speak generally of the unique features of spin torques in AFMs, how they are distinct from those in FM. Then we perform a realistic, first principles calculation using antiferromagnetic Cr and Au spacer.

Ch. (9) considers a system containing both FM and AFM elements. We again find features of spin transfer that are qualitatively different from those in conventional FM. This new form of spin torques leads to unusual magnetic configurations, which we predict should be observable experimentally.

Chapter 2

Spintronics

2.1 Introduction

Spintronics is a multi-disciplinary field that seeks to identify phenomena in which the spin degree of freedom plays a critical role, and to exploit spin-dependent effects for useful applications. It has drawn the interest of scientists who are interested in magnetism and related ordering phenomena from a fundamental science point of view, as well as the interest of scientists who are interested mainly in applications to information technology. The discovery of giant magnetoresistance effect by Albert Fert in 1988 is considered to be the birth of the field. Spintronics has already revolutionized hard-disk technology and there is hope that spintronic effects will continue to play a central role in the development of new information technology.

Information processing technology has been dominated by semiconductors for the past 50 years. The ability to fabricate semiconductors in a controlled fashion helped usher in the technology based society we live in today. Along the way, the importance and relevance of semiconductors spurred on new research, and helped the field of condensed matter physics grow enormously. In conventional electronics, control of circuit behavior is achieved by coupling to the charge of the electron, with

the application of bias potentials to circuits of ever increasing complexity. In this case, the spin of the electron is basically irrelevant, and is simply along for the ride. An essential motivation of spintronics is to find and/or design systems where the spin plays an active role in circuit behavior and design. This extra degree of freedom would presumably afford greater flexibility and capability to current technologies. There is, among optimists, the hope that spintronics can follow in the footsteps of semi-conductors in its scope, relevance, and scientific value [11].

One long-recognized phenomena that can be considered to be part of spintronics is anisotropic magnetoresistance; here the resistance of a ferromagnet is dependent on the relative orientation of the direction of current flow and magnetization [12]. Another active area is dilute magnetic semiconductors. The key challenge in this field is identifying the microscopic source of ferromagnetism in semiconductors doped with magnetic ions, and leveraging this understanding to design materials with transition temperatures sufficiently high for applications [13]. Other spintronic effects include the anomalous Hall effect, an effect whereby a ferromagnet develops an extra contribution to the Hall resistivity, due to spin-orbit coupling [14]. In this thesis, we focus on what are perhaps the largest subfields of spintronics: giant magnetoresistance (GMR) and spin transfer torques (STT). Both effects are observed in nanoscale systems, usually multilayers consisting of ferromagnetic and paramagnetic layers. The details of these two effects are described in the following sections.

A theme which runs through all of spintronics is the interplay between the magnetization and the nonequilibrium, current carrying quasiparticles. This may be considered a specific instance of the more general situation in which there is interaction between an order parameter and nonequilibrium quasiparticles. A familiar and simple example of this type of phenomena is a circuit in which current flows between normal (N) metal elements through a superconductor (S). Because of Andreev reflection of the quasiparticle current at the N/S boundary, the Cooper

pair amplitude in the superconductor is altered. In the presence of a normal metal transport current, the superconducting order parameter develops a spatial gradient in the steady state which allows the condensate to carry current through the superconducting element. A more recent example occurs in quantum Hall bilayers which develop excitonic condensates [5] under certain conditions and exhibit anomalies related [6] to the influence of transport currents on interlayer phase coherence.

The scientific approach to spintronics is emblematic of condensed matter physics as a whole: it employs a broad range of approaches from the abstract treatment of underlying principles using sophisticated theoretical techniques, to the very practical implementation of these effects in efforts more akin to device engineering. In this work, the approach we adopt may in some sense help to bridge the divide between these two distinct approaches. We seek to identify and generalize theoretically the phenomena associated with GMR and STT, and determine the extent to which such generalizations would be manifest in real materials.

In this chapter we review some of the basic properties of spintronics. In Sec. (2.2), we review the basic properties of ferromagnets relevant to spintronics effects. In Sec. (2.3), we discuss magnetoresistance, while in Sec. (2.4), we discuss spin transfer torques. In Sec. (2.5), we briefly review exchange bias, an effect we consider in more detail in Ch. (9).

2.2 Metallic magnetism

The first recorded observation of ferromagnetism comes from Greece in the 6th century BC [15]. Despite its long history, the physical origin of ferromagnetism was only understood in the past century, and the fundamental properties of ferromagnets remain a subject of theoretical and experimental research. Here we describe the basic properties of ferromagnets that will be important in describing spintronic phenomena.

In a ferromagnet, a macroscopic number of spins align and point in some preferred direction, forming a state with spontaneously broken symmetry. The existence of ferromagnetism in metals is the result of a subtle balance between quantum mechanical exchange energy and kinetic band energy. The exchange energy is a manifestation of Fermi statistics, which states that the total wave function must be anti-symmetric under interchange of particles. The physics behind the kinetic and exchange energy competition is most easily captured in a two-particle wave function. Due to the anti-symmetry requirement of the total wave function, a wave function with symmetric spin part (or spin-polarized state) must have an anti-symmetric real space part; since an anti-symmetric real space wave function reduces the Coulomb energy, this spin-polarized state is preferred. On the other hand, a symmetric real space wave function has a smaller kinetic energy than an anti-symmetric one, thereby favoring a spin-unpolarized state. Thus the spin polarization of the ground state depends on the balance between these two energies.

Nonclassical contributions to electron-electron interactions produce other contributions beyond exchange, referred to as the correlation energy. For spin polarized states, the exchange-correlation energy is spin-dependent, and acts as an effective magnetic field. The magnitude of the spin-dependent exchange-correlation energy in solids is described well by ab initio LSDA calculations, and for transition metals, can be characterized by an average value in the range of $0.7 - 1.0$ eV.

The competition between exchange/correlation and kinetic energies in solids is captured qualitatively by the Stoner model [16]. If the exchange/correlation energy is denoted by I , then ferromagnetism is stabilized for

$$D(E_f)I < 1 , \tag{2.1}$$

where $D(E_f)$ is the paramagnetic density of states at the Fermi energy. Eq. (2.1) is known as the Stoner criterion for ferromagnetism. Here a large density of states

at the Fermi level indicates that the kinetic band energy cost for forming a spin-polarized state is small, so that a spin-polarized state is energetically preferable. The materials which satisfy the Stoner criterion are Fe, Co, and Ni [16].

The exchange/correlation energy responsible for the ferromagnetic state (and correspondingly the magnitude of the magnetization) is large, and leads to magnetic transition temperatures of several hundred Kelvin. However, the dependence of energy on magnetization *direction* is determined from very small relativistic corrections to the energy. These include long range dipole-dipole interactions, and spin-orbit interactions which lead to magneto-crystalline anisotropy. Because of the relative smallness of these terms, the direction of the magnetization can be easily manipulated by external fields and currents. It is for this reason that magnetic materials are so amenable to applications.

As a matter of terminology, electrons whose spins belong to the larger spin population are referred to as “majority” electrons, while those with spin in the smaller spin population are “minority”. If we choose the axis of spin quantization such that the magnetization points in the $+z$ direction, then majority spins are labelled “up”, minority spins “down”. (Conversely, if the quantization axis chosen such that $+z$ points *opposite* to the magnetization, then majority are “down” and minority are “up”.)

2.3 Magnetoresistance

2.3.1 Giant magnetoresistance

In giant magnetoresistance (GMR), there is a (giant) change of resistance of the multilayer if the relative orientations of the magnetic layers changes. GMR is most easily understood in the configuration shown in Fig. (2.1) - here current flows

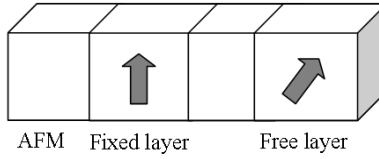


Figure 2.1: Schematic of a spin valve. The AFM layer pins the fixed layer’s orientation with the exchange bias effect.

perpendicular to the interface between layers ¹. In most experimental and applied systems, one of the layer’s magnetic orientation is fixed, while the other is free to rotate. (The fixed layer is pinned by an adjacent antiferromagnet through an effect known as exchange bias, or by having a different anisotropy.) Typically the free layer is bistable, and can point either parallel or anti-parallel to the fixed layer.

If the electron current enters from the left, then the fixed layer polarizes the current in the direction of its magnetization. Electrons with this polarity pass more easily through the free layer if its magnetization points in this same direction, so that a configuration with parallel fixed and free layers has a lower resistance than that with an anti-parallel configuration. The definition of magnetoresistance is:

$$\text{GMR} = \frac{G_P - G_{AP}}{G_{AP}} . \quad (2.2)$$

where $G_{P/AP}$ is the total conductance of the device in the parallel/anti-parallel configuration. (In the literature, GMR is sometimes defined as $(G_P - G_{AP})/G_P$. The difference between definitions is normally not significant.)

The promise of spintronics has already been fulfilled by GMR, since the effect forms the basis for current hard disc drive read-head technology. Because the magnetic layers are of nanoscale dimension, the orientation of the free layer,

¹There is a similar effect when current flows parallel to the layer interfaces (known as CIP GMR), but it is not as relevant in current research.

and therefore the resistance of the multilayer, is very sensitive to external fields. These multilayers may then be used as tiny magnetic field sensors, and in this role they have revolutionized the hard disk drive industry as the newest generation of read heads. Fig. (2.2) shows the explosion of the areal density of data storage that resulted from using magnetoresistance-based read heads.

Their effectiveness as sensors can be traced back to the separation of energy scales between the large spin-dependent exchange-correlation field, and the small anisotropy terms. A generic property of a “good” sensor is: small input \rightarrow large output. In this case, due to small anisotropy energy, a small magnetic field is sufficient to orient the magnetization, and because of the large exchange-correlation fields, this yields a large change in the transport conductance.

A simple quantitative account of GMR is provided by Valet-Fert theory [17]. In this model, the up and down spin channels carry current independently. The conductance G in a ferromagnet is different for majority and minority channel: $G_{\uparrow} \neq G_{\downarrow}$ (In spin valves, the resistance is often dominated by scattering at interfaces between materials. The conductance we consider here is therefore not the bulk material conductance, but the conductance associated with the interface.) The parallel and anti-parallel configurations of a spin valve are represented in Fig. (2.3). Applying Kirchoff’s laws for the current to the two different alignments immediately yields an expression for GMR in terms of the total conductance $G = G_{\uparrow} + G_{\downarrow}$ and the polarization $P = (G_{\uparrow} - G_{\downarrow})/G$:

$$G_P = \frac{G}{2} \tag{2.3}$$

$$G_{AP} = \frac{G(1 - P^2)}{2} \tag{2.4}$$

$$\text{GMR} = \frac{P^2}{1 - P^2} \tag{2.5}$$

It is clear from Eq. (2.5) that the GMR is maximized by maximizing P .

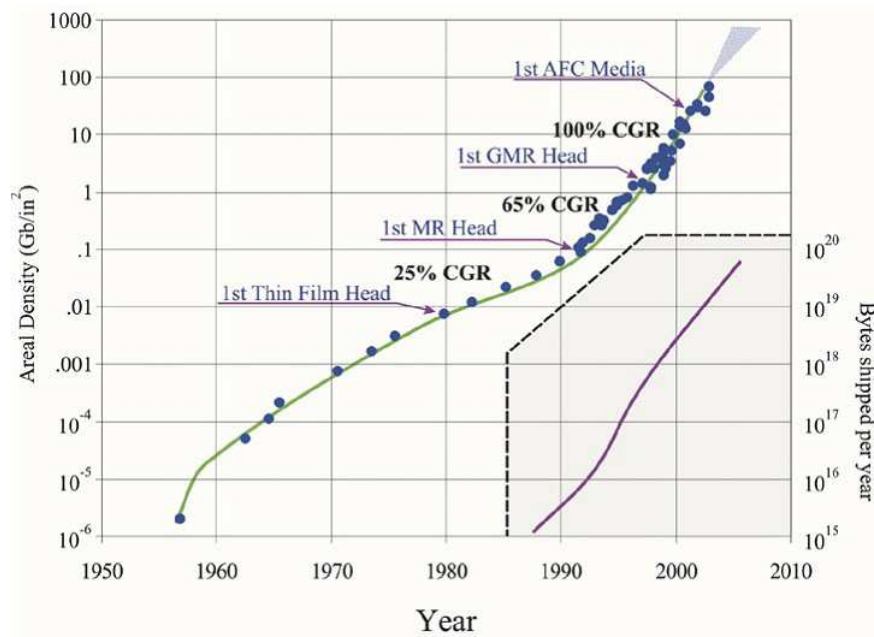


Figure 2.2: History of magnetic storage density with key innovations labelled. Inset shows total capacity of hard drives shipped per year. Fig. taken from Ref. [1], CGR stands for “compound growth rate”, AFC is “antiferromagnetically coupled media”, which represents an improvement in recording media design not of interest to us here.

In many systems, the difference between G_{\uparrow} and G_{\downarrow} can be understood in terms of electronic structure. As an example, we consider the materials of the classic experimental spin valve: Co magnetic layers separated by a Cu spacer (this setup is considered in detail in Ch. (7)). Fig. (2.4) shows the Fermi surface of these materials in the parallel and anti-parallel configurations. It is clear that the majority channel of Co has a Fermi surface that matches quite well with that of Cu, while the minority channel Co Fermi surface does not. Electrons undergo less momentum scattering when they make a transition between a bulk-like Co state to a bulk-like Cu state. Therefore, in the parallel alignment the conductance in the majority channel is much higher than that in the minority channel, so that $G_{\uparrow} > G_{\downarrow}$.

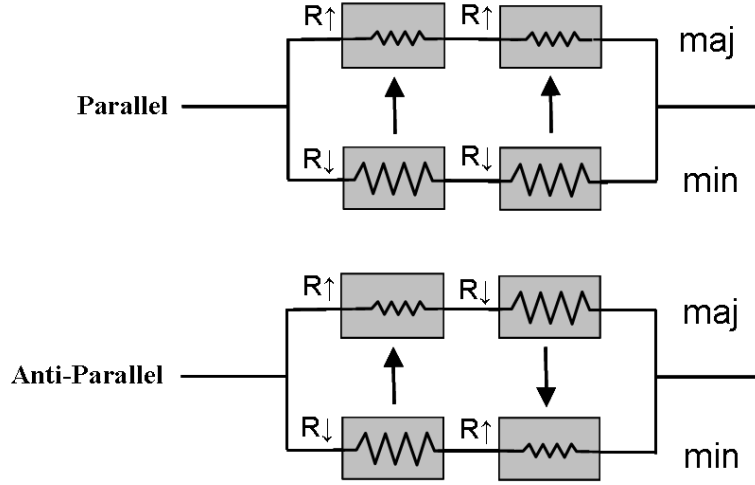


Figure 2.3: Schematic of the two channel model of GMR. The boxes labelling $R_{\uparrow/\downarrow}$ represent the spin-dependent resistance of a ferromagnet-normal metal interface.

2.3.2 Tunnelling magnetoresistance

Tunnelling Magnetoresistance (TMR) is distinguished from GMR by the presence of an insulating (rather than metallic) spacer layer. This changes the physical picture of the scattering. The Julliere model provides the simplest framework to understand this system. In this case the conductance is found from the Fermi Golden rule, and is proportional to the density of states at the Fermi energy of both magnetic layers: $G = 4\pi e^2 D_L(E_f) D_R(E_f) |T|^2$. An independent two-channel model for majority and minority spin is assumed, and the current in parallel and anti-parallel alignment is then given by:

$$\begin{aligned}
 I_P &\sim D_L^{\uparrow}(E_f) D_R^{\uparrow}(E_f) + D_L^{\downarrow}(E_f) D_R^{\downarrow}(E_f) \\
 I_{AP} &\sim D_L^{\uparrow}(E_f) D_R^{\downarrow}(E_f) + D_L^{\downarrow}(E_f) D_R^{\uparrow}(E_f)
 \end{aligned} \tag{2.6}$$

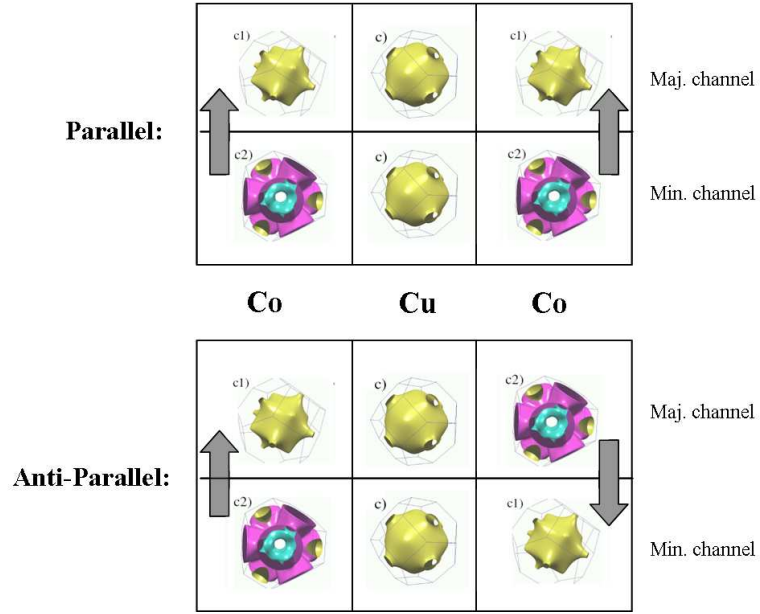


Figure 2.4: A schematic for the electronic structure of a Co-Cu spin valve .

These expressions lead to a magnetoresistance which is similar to the GMR expression, except with a different polarization factor $\bar{P} = (D^\uparrow(E_f) - D^\downarrow(E_f)) / (D^\uparrow(E_f) + D^\downarrow(E_f))$.

$$\text{TMR} = \frac{\bar{P}_L \bar{P}_R}{1 - \bar{P}_L \bar{P}_R} \quad (2.7)$$

Here the polarization factor is simply a bulk property of the material, and represents the fraction of spin-polarized electrons at the Fermi level. The TMR is maximized by maximizing \bar{P} , and the search for half-metals, or materials with $\bar{P} = 1$, is therefore a very active field in academia and industry.

In the Julliere model, the details of the tunnelling process are completely ignored (corresponding to neglecting the matrix elements $|T|^2$ in Fermi's golden rule). It was thought for a long time that these details are unimportant. However,

in a stunningly successful example of theoretical/computational materials design, Butler et al. [18] showed that the electronic structure of the ferromagnet-insulator combination can play a crucial role in maximizing TMR. They predicted that the combination of Fe and MgO would exhibit extremely large TMR ratios, which was subsequently verified experimentally. This tunnelling magnetoresistance (TMR) design is likely to be implemented in the next generation of read heads.

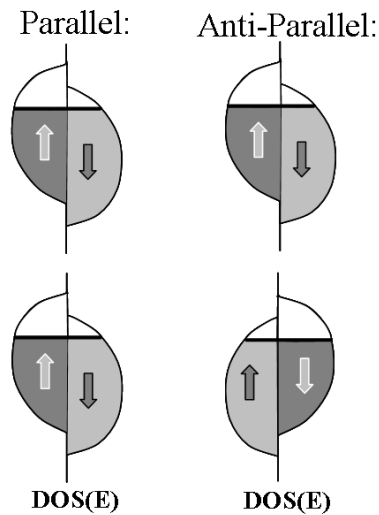


Figure 2.5: Julliere's model of TMR. In this model TMR is due to spin-dependent density of states the the Fermi level.

2.3.3 Molecular GMR

Recent efforts have shown that the spacer layer of a spin valve can consist only of a molecule, molecular monolayer, or carbon nanotube [19]. In one set of experiments, magnetoresistive effects were found in systems formed by sandwiching monolayer of octanethiole between Ni leads [20]. The finding is that the molecule is able to act as an effective spacer in a spin valve type structure, with GMR ratios on the order of

10%. With the machinery developed in this thesis, we have performed the first fully realistic calculation of GMR for a molecular system - a benzene di-thiol molecule sandwiched between Ni leads - and have found results consistent with experimental data [21]. (This work lies outside the main theme of this thesis and is therefore not addressed further.)

Other experiments examine magnetoresistance properties when the spacer consists of an organic semiconductor made from π -conjugated molecules [22, 23]. In this case, the transport behavior is non-Ohmic, and the conventional picture of GMR as described earlier must be modified. The machinery developed in this thesis is particularly well-suited for studying GMR in these novel systems.

2.4 Spin transfer

Spin transfer may be understood as the converse effect of GMR. In this case, the presence of a sufficiently large current density may change the relative orientation of the magnetic layers in a multilayer. This phenomenon is usually understood as a consequence of angular momentum conservation; if the electron current is incoming from the left, then it is initially polarized parallel to the fixed layer. In traversing the free layer, the current is then polarized in the direction of the free layer. The direction of the current polarization is therefore changed, or rotated, by the free layer - the free layer magnetization exerts a torque on the spin of the current. By conservation of angular momentum, the spin current must exert an equal and opposite torque on the free layer magnetization. This is indicated schematically in Fig. (2.6). In this way, spin angular momentum is transferred from one subsystem - the current carrying electrons - into another subsystem - the magnetization. For this reason the effect is known as spin transfer. If the torque exerted on the magnetization by the current is sufficiently large, the magnetization can undergo complete reversal and can be switched from parallel to anti-parallel (or the reverse). In addi-

tion, dynamical modes in which the free layer magnetization undergoes microwave precession can occur. This effect was predicted theoretically in 1996 by Slonczewski [24] and Berger [25], and subsequently observed experimentally [26, 27, 28, 29, 30], and is now the subject of extensive research.

One potential application of spin transfer is magnetic random access memory, or MRAM. In MRAM, the orientation of the free layer (parallel or anti-parallel to fixed layer) encodes binary data (“0” or “1”). A large current could change the orientation with spin transfer torque, or perform a write operation, while a lower current could sense the orientation via the GMR effect, or read the data. This method of data storage holds distinct advantages over conventional RAM - most notably it is non-volatile, so that information is retained even after power loss. Current MRAM technologies use current-induced magnetic fields for writing data, but such a mechanism poses problems for power consumption and scaling. These problems are resolved with the use of spin transfer as a writing mechanism [8]. Efforts to this end are currently underway in academic and industrial research.

2.5 Exchange bias

We mention here some details of a phenomena known as exchange bias. Exchange bias refers to the effect in which an anti-ferromagnet adjacent to a ferromagnet effectively pins the ferromagnet, so that the switching field of the ferromagnet is greatly increased. This is typically used in spin valves to ensure that the fixed layer remains fixed.

Exchange bias is an effect which currently probably resides in the category of magnetics proper, as opposed to spintronics (the distinction arising because spintronics involves nonequilibrium quasi-particles, a notion that is independent of the current understanding of exchange bias). We nevertheless mention some background of exchange bias here, as in a later chapter we consider the effect of spin transfer

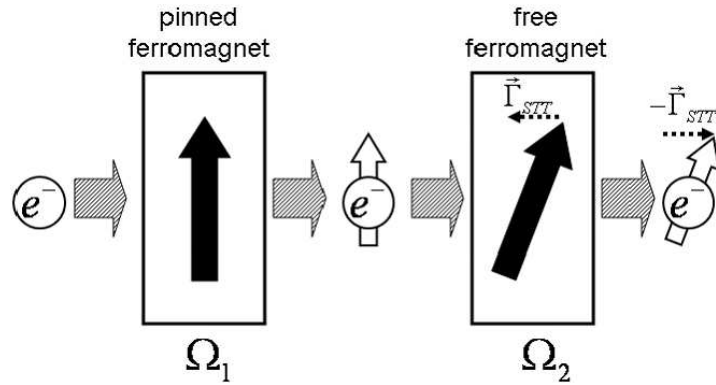


Figure 2.6: Cartoon showing spin transfer torque. The electron spin enters the free ferromagnet point up, and is rotated by the magnetization so that it leaves in a different direction. Spin transfer is the back-action torque on the magnetization by the electron spin.

torques on exchange bias.

2.5.1 Meiklejohn and Bean - direct exchange

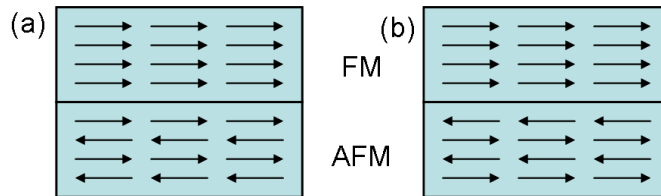


Figure 2.7: Geometry in direct exchange model: (a) is a low energy configuration, while (b) is a high energy configuration. The difference in energy leads to unidirectional anisotropy for the FM, or exchange bias.

This is the first and simplest model of exchange bias [31]. The antiferromagnet interface is uncompensated, with a net spin/area M_{AFM} , and a Heisenberg

coupling J_1 to the ferromagnetic spin M_F is assumed:

$$E_{direct} = J_1(\vec{M}_{AFM} \cdot \vec{M}_F) \quad (2.8)$$

If one assumes that the antiferromagnet does not undergo reversal with the ferromagnet, then there will be a unidirectional anisotropy and the shift in the hysteresis curve (or the bias field) is immediately seen to be :

$$H_E = \frac{\Delta E}{2M_F t_F} = J_1 \frac{1}{M_F t_F} \quad (2.9)$$

However this formula leads to bias fields that are orders of magnitude too large, motivating refinements of this simple picture.

An important recent experimental realization of Stohr et al. [32] makes this simple model more relevant than previously thought. It was found that there are in fact only a very small percentage (4%) of moments at the AFM interface which are pinned. The rest of the moments rotate rigidly with the ferromagnet. Only these pinned moments contribute to the expression above, so that the predicted bias fields are reduced by a factor of .04, which leads to realistic values for the exchange bias. However, the nature of the pinning (its origin and magnitude) is not known. We consider open questions relating spin transfer torques to exchange bias in the last chapter.

Chapter 3

Transport in Mesoscopic Systems

3.1 Introduction

In this chapter we review the physical picture of electron transport relevant to systems in the mesoscopic regime. In so doing, we hope to shed light on what is precisely meant by the term “mesoscopic”. This picture is provided by the Landauer theory of transport, which we use extensively throughout the thesis, and describe in Sec (3.2). We also review other formalisms used in this work to study transport, including scattering matrices in Sec. (3.4), and spin circuit theory, described in Sec. (3.5). First we review important length scales for the systems we have in mind:

1. Screening Length L_s : The screening length indicates the length scale over which a perturbation in the electronic charge density is screened by free charges. Within Thomas-Fermi theory of a free electron gas, $L_s = \left[\frac{e^2 D(E_f)}{\epsilon_0} \right]^{-1/2}$, where $D(E_f)$ is the density of states at the Fermi level. For metals, $D(E_f)$ is large and this length is of the order of $1 - 10\text{\AA}$.

2. Mean Free Path L_m : The mean free path is the distance an electron

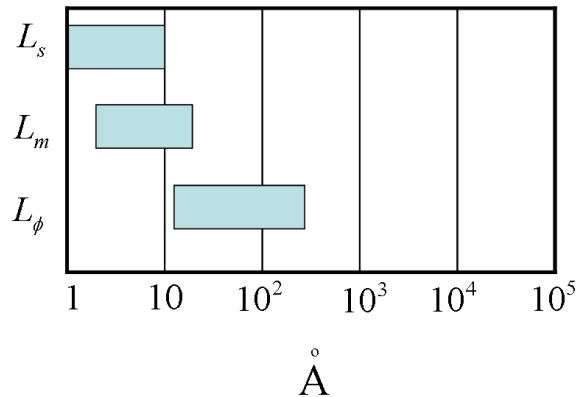


Figure 3.1: Length scales relevant for mesoscopic systems. Figure adapted from Ref. [2].

travels before undergoing momentum scattering. The change in momentum is due to scattering from impurities in the lattice, interfaces, or any other defect that does not exchange energy with the electron (static impurities). It is basically the length scale on which an electron notices that it is not in a perfect crystal, which has rather special properties because of Bloch's theorem [3]. The mean free path is related to the momentum relaxation time τ_m by $L_m = v_F \tau_m$. τ_m is often much longer than collision time τ_c , because most collisions are often ineffective at changing the momentum of the electron. This is usually parameterized by $\alpha \frac{1}{\tau_m} = \frac{1}{\tau_c}$, where α is between 0 and 1. Values of mean free paths depend of extrinsic factors such as sample purity and temperature, but a typical value for transition metals under experimental conditions is $10 \sim 20 \text{ \AA}$.

3. Phase coherence length L_ϕ : The phase coherence length is the distance an electron travels before it experiences an energy-changing scattering event (inelastic scattering). Equivalently, it is the distance travelled before quantum phase information of its state is lost. The entity from which the electron scatters must have an internal degree of freedom to exchange energy with the electron, and common ex-

amples are phonons, other electrons, and spin waves. As before, the rate of inelastic scattering is in general smaller than the rate of overall collisions, and we parameterize the relation as: $\frac{1}{\tau_\phi} = \alpha_\phi \frac{1}{\tau_c}$, with α_ϕ again between 0 and 1. L_ϕ is related to temperature (primarily via phonons) roughly as $L_\phi \sim T^{-p}$, where $p \sim 1 - 2$. Typical values for experimental system are $L_\phi \sim 100 - 200 \text{ \AA}$. In pure metals at room temperature and above, the situation in which most scattering is inelastic is common. In this case $L_\phi = L_m$.

3.2 Landauer

When electron transport takes place through a system with dimensions on the order of a mean free path, quantum mechanical effects become important, and the assumptions of semi-classical transport break down. (Semiclassical transport ideas can fail at low temperature when L_ϕ is very long because of localization physics.) This physics in this regime was initially studied by R. Landauer in the 1950's [33, 34], and extended M. Buttiker and others in the 1980's [35, 36]. In the experimental situation of interest, a scattering region is connected to two much larger particle reservoirs. When an external bias is applied, i.e. when the chemical potentials of the reservoirs are different, a steady state nonequilibrium current flows through the scattering region. If the chemical potential of the left reservoir is greater than that of the right, then the current is carried by an imbalance of right-goers emanating from the left reservoir into the unfilled states of the right reservoir. The schematic for the experimental setup is given in Fig. (3.2). A key assumption underlying the Landauer picture is that the contacts between the wire and the reservoirs are reflectionless: that is, that electrons are not reflected back into the wire as they leave it and enter the reservoirs. When the reservoirs are much wider than the wire (have many more transverse modes), it has been verified that this assumption is usually valid [37]. We can then be assured that rightmoving electrons to the left

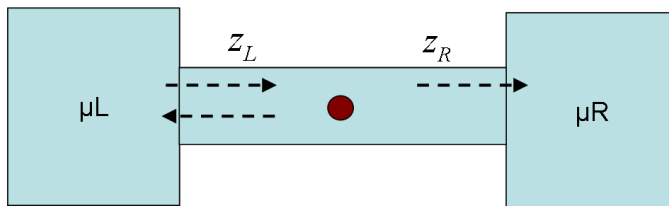


Figure 3.2: 2-probe geometry. Here $\mu_L > \mu_R$, and the circle in the conducting wire represents some static scatterer.

of the scatterer emanated from the left contact, and are in equilibrium with the left contact, with chemical potential μ_L . We emphasize that this formulation of transport assumes that L_ϕ is larger than the system size.

A key observation in the Landauer picture of transport is the simple relation between the current carried by states with energy E and their occupation number $f(E)$. To demonstrate this relation consider the current carried by states with momentum between k and $d + dk$:

$$I = \frac{e}{2\pi} v_k f(E_k) dk \quad (3.1)$$

$$I = \frac{e}{2\pi\hbar} \frac{\partial E}{\partial k} f(E_k) dk \quad (3.2)$$

$$I = \frac{e}{2\pi\hbar} \frac{\partial k}{\partial E} \frac{\partial E}{\partial k} f(E) dE \quad (3.3)$$

$$I = \frac{e}{h} f(E) dE \quad (3.4)$$

The current is simply proportional to the occupation $f(E)$. It may seem surprising that the factor of velocity drops out, but it is simply compensated by a factor of density of states: states with a smaller velocity have a larger density of states and vice versa.

We can then find the current for the 2-probe geometry of Fig. 3.2. We consider just a single channel wire, and take the probability of electron transmission

through the scatterer to be T (so that the probability of reflection is $1-T$). Consider the location $z = z_L$ along the wire. Using the assumption of reflectionless contacts, we know right-moving electrons emanated from the left reservoir, and are therefore described by an occupation $f_L(E)$:

$$I_{z=z_L}^{\text{Right}}(E) = \frac{e}{h} f_L(E) dE \quad (3.5)$$

Left-moving electrons at this point consist of states that emanate from the right reservoir and are transmitted through the scatterer, and states emanating from the left reservoir that are reflected from the scatterer:

$$I_{z=z_L}^{\text{Left}}(E) = \frac{e}{h} (f_L(E)(1-T) + f_R(E)T) dE \quad (3.6)$$

The net current is then:

$$I^{\text{tot}} = \frac{e}{h} T (f_L(E) - f_R(E)) dE \quad (3.7)$$

Integrating over all energies, we obtain the Landauer formula for the conductance G of a 1-dimensional system:

$$I = \frac{e}{h} T [\mu_L - \mu_R] \quad (3.8)$$

$$\Rightarrow G = \frac{e^2}{h} T \quad (3.9)$$

The constant e^2/h is known as the quantum unit of conductance, and its value is $3.87 \times 10^{-5} \Omega^{-1}$. The formula can be generalized to a system with N transverse channels:

$$G = \frac{e^2}{h} \sum_{i=1}^N T_i \quad (3.10)$$

The result is intuitively appealing: the conductance of a sample is very simply related to the probability that electrons can transmit through it.

Historically, Eq. (3.10) was a source of controversy, as many of the investigators at the time viewed the finite (rather than infinite) conductance of a perfect sample as a fatal flaw in the theory [38]. An alternative formula which did not “suffer” from this feature was

$$G = \frac{e^2}{h} \sum_{i=1}^N \frac{T_i}{1 - T_i}. \quad (3.11)$$

Nevertheless experiments confirmed the validity of Landauer’s formula in 1988 [39].

The apparent discrepancy between Eq. (3.10) and Eq. (3.11) may be reconciled by distinguishing between the scattering and contact contributions to the resistance [40]. Landauer’s formula can be re-written to clarify this distinction:

$$G_{\text{tot}}^{-1} = \frac{h}{e^2} \frac{1}{N} \left[\frac{1 - \bar{T}}{\bar{T}} + 1 \right] \quad (3.12)$$

where \bar{T} is the average conductance:

$$\bar{T} = \frac{1}{N} \sum_{i=1}^N T_i \quad (3.13)$$

The scattering resistance G_S^{-1} and contact resistance G_C^{-1} are identified as:

$$G_S^{-1} = \frac{h}{e^2} \frac{1}{N} \left(\frac{1 - \bar{T}}{\bar{T}} \right) \quad (3.14)$$

$$G_C^{-1} = \frac{h}{e^2} \frac{1}{N} \quad (3.15)$$

The origin of contact resistance is the redistribution of the current from the many transverse channels of the reservoir into the relatively smaller number of channels for a thin wire. Indeed, for the case where the conductor acquires many

transverse channels (or has a large cross sectional area), the contact resistance goes to 0. In the context of 3-dimensional multilayer geometries, the contact resistance is also known as the Sharvin resistance. The distinction between contact and scattering resistance is discussed further in Sec. (3.4.1).

3.3 From Landauer to Boltzmann.

To put the Landauer approach in context, we consider here the relation between the conductivity obtained with a Landauer approach and that obtained with a semi-classical approach. The conductivity of the Drude model (a fully classical model) is given by $\sigma = ne^2\tau/m$. In a semi-classical Boltzmann approach, the conductivity of a uniform bulk material within the relaxation time approximation is

$$\sigma_{\alpha\beta} = \tau \frac{e^2}{4\pi^3} \int d\mathbf{k} f_{\mathbf{k}} v_{\alpha} v_{\beta} \frac{\partial f}{\partial \mu} = ne^2\tau \mathbf{M}_{\alpha,\beta}^{-1} \quad (3.16)$$

$$\mathbf{M}_{\alpha,\beta}^{-1} = \frac{1}{\hbar^2} \frac{\partial^2 E_{\mathbf{k}}}{\partial k_{\alpha} \partial k_{\beta}} \quad (3.17)$$

This is identical to the Drude result with band structure effects included in the effective mass tensor. For metals, $\frac{\partial f}{\partial \mu} \approx \delta(\epsilon - \epsilon_F)$, and σ can be rewritten as an integral over the Fermi surface A_{FS} :

$$\sigma_{\alpha\beta} = \frac{e^2\tau}{4\pi^3\hbar} \int dA_{FS} \left(\frac{v_{\alpha}v_{\beta}}{v} \right) \quad (3.18)$$

$$\Rightarrow \sigma_{zz} = \frac{e^2\tau}{4\pi^3\hbar} \int dA_{FS}(v_z) \quad (3.19)$$

A similar result can be obtained in a Landauer approach under the following conditions: if λ is the mean free path, we assume the system length $L \gg \lambda$. We then coarse grain the system into M cells each of length l , where $l < \lambda$; in each cell we can apply the ballistic Landauer formalism. We suppose some transmission probability T through each cell, so that each cell has an associated scattering resistance of

$G^{-1} \sim (1 - T)/T$ (see Eq. (3.14)). The total resistance is then given by the series resistance:

$$G_{\text{tot}}^{-1} = \sum_{i=1}^M G_i^{-1} = M \frac{h}{e^2} \left(\frac{1 - T}{T} \right) = \frac{L}{\lambda} \frac{h}{e^2} \left(\frac{1 - T}{T} \right) \quad (3.20)$$

The mean free path λ can be traded for a relaxation time τ via the relation $l = v_f \tau$. Then

$$\frac{G_{\text{tot}}^{-1}}{L} = \frac{1}{v_F \tau} \frac{h}{e^2} \left(\frac{1 - T}{T} \right) \quad (3.21)$$

By summing over transverse channels (or integrating over the Fermi surface), we find

$$\frac{G_{\text{tot}} L}{A} \equiv \sigma = \frac{e^2 \tau}{2\pi^2 h} \int dA_{FS} v_z \left(\frac{T}{1 - T} \right) \quad (3.22)$$

Comparing to Eq. (3.19), the result reproduces the Boltzmann approach result (with extra factors of T). The exact values of T would depend on the choice of l (and τ). The key point in this development is that the sample must be sufficiently large so that a choice of l is possible such that the transmission T any portion of the sample with this length is essentially uniform. In this sense, the scattering throughout the sample is self-averaging: the details of particular scattering events are washed out. To the extent that a sample is mesoscopic, such a choice of l is not possible, and the specific details of the scattering throughout each section of the sample are experimentally relevant.

3.4 The scattering matrix

So far we have considered Landauer's formula, which relates the conductance of a system connected to two reservoirs to the scattering state transmission probability.

In this work we are also interested in multilayer systems, in which there are several interfaces between different materials, each of which acts as a scattering potential. A scattering matrix formalism is useful for studying such systems.

The scattering matrix expresses the out-going amplitudes in terms of incoming amplitudes:

$$|\phi_{\text{out}}\rangle = \mathcal{S} |\phi_{\text{in}}\rangle \quad (3.23)$$

In the geometries considered here, the asymptotic wave functions are Bloch states. As a matter of notation, we write $\phi_{L/R}(+\infty)$ for left/right moving states at $z = +\infty$, and $\phi_{L/R}(-\infty)$ for left/right moving states at $z = -\infty$. This is represented schematically below:

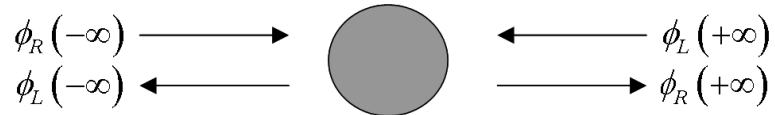


Figure 3.3: Incoming and outgoing states scattering off a generic potential.

With this notation, Eq. (3.23) becomes:

$$\begin{pmatrix} \phi_L(-\infty) \\ \phi_R(+\infty) \end{pmatrix} = \mathcal{S} \begin{pmatrix} \phi_R(-\infty) \\ \phi_L(+\infty) \end{pmatrix} \quad (3.24)$$

Where the scattering matrix has the form:

$$\mathcal{S} = \begin{pmatrix} r & t' \\ t & r' \end{pmatrix} \quad (3.25)$$

The utility of the scattering matrix approach is that the effect of multiple scattering potentials can be found simply by composing the individual scattering matrices for

each potential. For example, given two scattering matrices $\mathcal{S}_1, \mathcal{S}_2$, and supposing that scatterer 1 is to the left of scatterer 2, we can compose them to find their combined effect:

$$\mathcal{S}_{12} = \begin{pmatrix} r_1 + t'_1 r_2 (1 - r'_1 r_2)^{-1} t_1 & t'_1 (1 - r_2 r'_1)^{-1} t'_2 \\ t_2 (1 - r'_1 r_2)^{-1} t_1 & r'_2 + t_2 (1 - r_2 r'_1)^{-1} r'_1 t'_2 \end{pmatrix} \quad (3.26)$$

The total transmission amplitude through the two scatterers is therefore $t_{12} = t_1 (1 - r_1 r_2)^{-1} t_2$. We can include phase coherent effects by including the phase shifts associated with $t_{1,2}$

$$T_{12}^{\text{coherent}} = \frac{T_1 T_2}{1 + R_1 R_2 - 2\sqrt{R_1 R_2} \cos(\theta)} \quad (3.27)$$

where θ is the phase shift acquired by the state in one round-trip between the scatterers. We can also remove phase coherent effects by composing transmission/reflection probabilities instead of amplitudes. In this case the total transmission is:

$$T_{12}^{\text{incoherent}} = \frac{T_1 T_2}{1 - R_1 R_2} \quad (3.28)$$

In later chapters we utilize both equations to highlight the differences between treating the transport between successive interfaces coherently and incoherently.

3.4.1 Scattering matrices and interface resistance

When concatenating scattering matrices or transmission amplitudes obtained from the Landauer formula, it is important to include only the scattering contribution to the resistance (and to discard the contact or Sharvin resistance); the distinction between these contributions is described in Sec. (3.2). In Ref. [41], Schep et al.

derive the proper interface resistance between two materials A and B .

$$R_{AB} = \frac{h}{e^2} \left(\frac{1}{\sum_m |T_m|^2} - \frac{1}{2} \left(\frac{1}{N_A} + \frac{1}{N_B} \right) \right) \quad (3.29)$$

Where $N_{A/B}$ is the number of states at the Fermi level of material A, B . This expression is a generalization of the scattering resistance given by Eq. (3.14). When this formula is used, first principles calculations for interface resistance agree with experimental results [42].

The contributions to experimentally observed resistance depend on the experimental geometry. For a 2-probe experiment, in which the same leads through which current flows also detect the potential difference, the contact resistance is measured along with the scattering resistance. If a 4-probe measurement is performed, then the voltage probe no longer detects the contact resistance contribution to the overall resistivity.

3.5 Conductance of materials in the diffusive regime

In this section we describe the formalism recently developed to calculate transport properties of noncollinear magnetic systems within the diffusive regime [43, 42]. This topic is somewhat ancillary to the main thrust of this thesis. We include the details of this formulation however because in Sec (7.4), we will contrast the transport properties obtained from a Landauer approach with the properties obtained from this approach. The aim of that exercise is to highlight the role of the ballistic assumption of our calculation.

As discussed in Sec. (3.1), the size of nanoscale or mesoscopic systems is usually on the order of the mean free path or phase coherence length. In ballistic theories of transport, such as the Landauer approach, phase coherent quantum interference effects are fully included. In our calculation (and most others to date as

well), interface scattering is taken to be specular, so that k_{\parallel} is conserved. In the diffusive limit, both phase coherent and specular scattering effects are completely removed. It is useful to study both regimes because real systems are probably not entirely ballistic or diffusive, but possess properties of both.

The theory for spin-dependent diffusive transport in multilayer geometries that we consider in this work is known as “spin-circuit theory” (SCT), or magneto-electronics. It was introduced by A. Brataas, G. Bauer, and Y. Nazarov in 2000 [43]. Here we give an indication of the physics that is involved in its formulation. SCT can be thought of essentially as Ohm’s and Kirchoff’s Laws generalized to noncollinear spin space. Because of the vector nature of spin, all quantities which are scalars (c_o) in conventional circuit theory become 4-vectors (c_o, c_x, c_y, c_z) in SCT . As in conventional circuit theory, the input parameters include the resistors (their topology and values) and the applied voltages, while the outputs are the spin-dependent current and voltages throughout the system. The first step in applying the theory is to map a multilayer geometry into an equivalent configuration of resistors. The orientations of the magnetic layers are the final input parameters for a calculation. The resistivity of a multilayer has contributions from the bulk resistivity of the materials involved, and also the resistivity from the sharp interface between two different materials. In this work we will only consider the resistance contribution from the interfaces, which should be larger for system with thin layers.

A trilayer spin-valve type structure can be mapped into a simple Kirchoff-like circuit shown in Fig. (3.4). The interface resistance can be obtained from first principles methods, and is characterized by 4 numbers: $G_{\uparrow}, G_{\downarrow}$, and $G_{\uparrow\downarrow}$. G_{σ} is the standard spin-dependent conductances found with Landauer’s formula. $G_{\uparrow\downarrow}$ is a complex number related to the noncollinear nature of the conductance, and is given

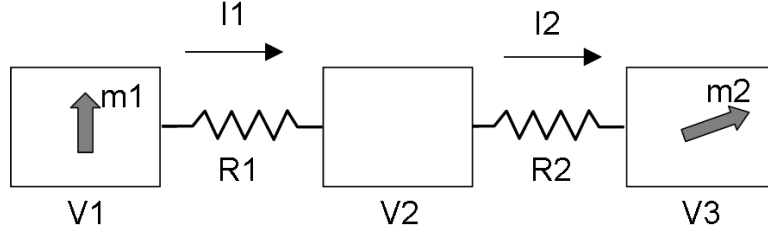


Figure 3.4: Equivalent circuit model for trilayer calculation. The “resistors” represent the interfaces.

by:

$$G_{\uparrow\downarrow} = \sum_{mn} (T_{mn}^{\uparrow})^* T_{mn}^{\downarrow} \quad (3.30)$$

The currents and potentials are defined in noncollinear spin space:

$$I = \begin{pmatrix} I_{\uparrow\uparrow} & I_{\uparrow\downarrow} \\ I_{\downarrow\uparrow} & I_{\downarrow\downarrow} \end{pmatrix} = \frac{1}{2} (I_c + \mathbf{I}_s \cdot \sigma) \quad (3.31)$$

$$f = \begin{pmatrix} f_{\uparrow\uparrow} & f_{\uparrow\downarrow} \\ f_{\downarrow\uparrow} & f_{\downarrow\downarrow} \end{pmatrix} = f^N + \mathbf{s} \cdot \sigma \quad (3.32)$$

The spin-dependent potential on a normal metal node (denoted by a superscript N) can point in any direction, but the potential on a ferromagnetic node (superscript F) is assumed to point in the direction of the magnetization \mathbf{m} :

$$f^N = f_c^N + f_s^N \mathbf{s} \cdot \sigma \quad (3.33)$$

$$f^F = f_c^F + f_s^F \mathbf{m} \cdot \sigma \quad (3.34)$$

The fact that the spin-dependent potential is aligned with the magnetization assumes that the spin current flux transverse to the magnetization is absorbed by the

magnetization. This is satisfied for layers thicker than about 3 nm [44] (see Sec. (6.3)).

It is convenient to rewrite the conductance parameters as $G = G^\uparrow + G^\downarrow$, $p = (G^\uparrow - G^\downarrow)/G$, $\eta_R = 2\text{Re } G^{\uparrow\downarrow}/G$, $\eta_I = 2\text{Im } G^{\uparrow\downarrow}/G$. The extension of Ohm's Law ($I = GV$) for charge and spin current flowing between a $F|N$ interface is then:

$$I_c = G (f_c^F - f_c^N) - p G (f_s^N \mathbf{m} \cdot \mathbf{s} - f_s^F) \quad (3.35)$$

$$\begin{aligned} \mathbf{I}_s = G [& (p (f_c^F - f_c^N) - f_s^F + (1 - \eta_R) \mathbf{s} \cdot \mathbf{m}) \mathbf{m} \\ & + \eta_R \mathbf{s} + \eta_I (\mathbf{s} \times \mathbf{m})] \end{aligned} \quad (3.36)$$

Kirchoff's Laws extended to noncollinear spin space take the form:

$$\sum_{\alpha} I_{\alpha} = 0 \quad (\text{for N and F nodes}) \quad (3.37)$$

$$\sum_{\alpha} \mathbf{I}_{s\alpha} = 0 \quad (\text{for N nodes}) \quad (3.38)$$

$$\sum_{\alpha} \mathbf{I}_{s\alpha} \cdot \mathbf{m} = 0 \quad (\text{for F nodes}) \quad (3.39)$$

Eqs. (3.37) and (3.38) state that the net charge and spin current flux into a normal metal is 0. This represents conservation of charge and spin. Eq. (3.39) states that the net flux of the spin current parallel to the magnetization is 0.

To give a feel for of a calculation based on these equations, we consider a simple example to illustrate how the above may be applied in the most simple-minded way. For the trilayer system represented in Fig. (7.8), the ‘‘input’’ variables are applied voltage $\mathbf{V}_1, \mathbf{V}_3$, (the orientations of the two ferromagnets are also inputs, and are implicit in $\mathbf{V}_1, \mathbf{V}_3$) and the resistors values G_1, G_2 , while the ‘‘unknown’’ variables are $\mathbf{I}_1, \mathbf{I}_2, \mathbf{V}_2$ (12 unknowns). Eqs. (3.35) and (3.36) for \mathbf{I}_1 and \mathbf{I}_2 give 8 equations, while Eqs. (3.37-3.38) give 4 more equations (note Eq. (3.39) is not needed since the only unknowns are in a normal metal node) . Thus we have 12

unknowns, and 12 linear equations, which can be easily solved (on a computer).
(This particular calculation can be simplified much more, but that need not concern us here.)

Chapter 4

Keldysh

In this chapter we consider a convenient formalism to apply the Landauer transport picture. In Sec. (4.1) and (4.2), we give an account of equilibrium and nonequilibrium Green's functions, with the aim of elucidating the key differences between the two. In Sec. (4.3), we apply the nonequilibrium Green's function formalism to the two-probe transport measurement geometry to derive expressions for the density matrix. Finally, in Sec. (4.4), we explain the technical details of implementing this formalism within DFT. The approach adopted here is somewhat pedagogical, and there are many more heuristic or intuitive explanations of this formalism in the literature [40]. We do not go into great detail as to the nuts and bolts implementation of this formalism, as the main thrust of the thesis is to build upon this formalism in calculating spin transfer torques. With these caveats, we proceed.

4.1 Green's functions in equilibrium systems

To describe an interaction or perturbation, we break up the Hamiltonian as follows:

$$H = H_0 + H_1 , \tag{4.1}$$

where H_1 is the perturbing term. A standard method of handling the perturbation term is with a Green's function method. We are interested in situations in which the perturbation introduces irreversible processes. In this case, the traditional Green's function method is modified, leading to the so-called nonequilibrium Green's function formalism. This was initially developed by Schwinger [45], Keldysh [46], and Kadanoff and Baym [47]. The approach described here is that of Keldysh. To illustrate the key ingredients of this formulation, we briefly review the formulation of the traditional Green's function expansions, and then specify how this expansion changes in the presence of irreversible transitions.

The derivation of the expression of the Green's function expansion is formal, so it is useful for orientation to sketch a preview of the steps involved: first we define an operator S which propagates states ψ according to H_1 . S is then written as a power series expansion in H_1 . With this approximate expression for S , we can determine the expectation value of any operator \hat{O} (in particular the Green's function operator \hat{G}) for the system described by the full Hamiltonian.

Interaction picture

In order to formulate a perturbation expansion for S in powers of H_1 , it is necessary to use the interaction picture for time evolution. Time evolution is often described by the Schrödinger or Heisenberg picture: In the Schrödinger picture, the dynamics is ascribed to the wave function $\psi(t)$, while in the Heisenberg picture the dynamics is ascribed to operators $\hat{O}(t)$. In the case where the Hamiltonian is time-independent, these two pictures' time dependence can be written as:

$$\psi_S(t) = e^{i\hbar H t} \psi_S(0) \quad \text{Schrödinger} \quad (4.2)$$

$$\hat{O}_H(t) = e^{-i\hbar H t} \hat{O}_H(0) e^{i\hbar H t} \quad \text{Heisenberg} . \quad (4.3)$$

(The subscripts S and H indicate Schrödinger and Heisenberg, respectively). In the interaction picture, the states ψ evolve in time according to H_1 , while the operators evolve according to H_0 . This is accomplished by defining $\psi_I(t) = e^{iH_0t}\psi_S(t)$ (subscript I is for interaction picture). This definition can be understood intuitively: $\psi_S(t)$ evolves with the full Hamiltonian, while e^{iH_0t} undoes the contribution of H_0 , leaving the contribution of H_1 . The equations of motion for a state and an operator are in the interaction picture are then:

$$i\hbar \frac{\partial \psi_I}{\partial t} = \hat{H}_I \psi_I \quad (4.4)$$

$$\frac{\partial \hat{O}_I}{\partial t} = i\hbar [\hat{O}_I, \hat{H}_0] . \quad (4.5)$$

Time evolution operator S

Now we define the propagator $S(t, t')$ as:

$$\psi_I(t) = \hat{S}(t, t') \psi_I(t') . \quad (4.6)$$

S propagates a state forward in time under the action of the perturbing Hamiltonian H_1 . The formal expression for S is given as:

$$S(t, t') = \sum_{n=0}^{\infty} \frac{1}{n!} \int_t^{t'} dt_1 \cdots \int_t^{t'} dt_n T[\hat{H}_1(t_1) \cdots \hat{H}_1(t_n)] . \quad (4.7)$$

The symbol T orders the operators so that the operators at earlier times are to the right of operators at later times. If ψ_0 is the ground state wave function of H_0 , then S has the following important property:

$$\psi_I(t) = S(t, -\infty) \psi_0 . \quad (4.8)$$

In Eq. (4.8), it is assumed that the perturbation is adiabatically turned on, starting from a system with no perturbation present at $t = -\infty$ (the adiabatic assumption ensures that the system remains in its ground state as the perturbation is turned on).

The expectation value of an operator in the Heisenberg picture is related to the expectation value in the interaction picture as follows:

$$\begin{aligned}\langle \hat{O}_H(t) \rangle &= \frac{\langle \psi_0 | \hat{O}_H(t) | \psi_0 \rangle}{\langle \psi_0 | \psi_0 \rangle} = \frac{\langle \psi_I(t) | \hat{O}_I(t) | \psi_I(t) \rangle}{\langle \psi_0 | \psi_0 \rangle} \\ &= \frac{\langle \psi_0 | S(+\infty, t) \hat{O}_I(t) S(t, -\infty) | \psi_0 \rangle}{\langle \psi_0 | S(+\infty, t) S(t, -\infty) | \psi_0 \rangle}.\end{aligned}\quad (4.9)$$

Eq. (4.9) can be understood intuitively: the operator O_I contains the contribution to the time evolution from H_0 , while S contains the contribution from H_1 ; their combination given in Eq. (4.9) gives the combined effect for the total evolution, allowing for the evaluation of \hat{O}_H .

The adiabatic assumption is made in Eq. (4.9) when we write $\langle \psi_I(t) | = \langle \psi_0 | S(+\infty, t)$. Here we assume that the perturbation is turned off at $t = \infty$, and that upon turning off the perturbation, *the state returns to its known ground state*. That is, we assume reversibility. This is the key assumption that is lifted in the nonequilibrium Green's function formalism.

Plugging the formal expression for S into Eq. (4.9) leads to the result:

$$\begin{aligned}\langle \hat{O}_H(t) \rangle &= \frac{1}{\langle \psi_0 | S | \psi_0 \rangle} \langle \psi_0 | \sum_{j=0}^{\infty} \left(\frac{-i}{\hbar} \right)^j \frac{1}{j!} \int_{-\infty}^{\infty} dt_1 \cdots \\ &\quad \cdots \int_{-\infty}^{\infty} dt_j T[\hat{H}_1(t_1) \cdots \hat{H}_1(t_j) \hat{O}_I(t)] | \psi_0 \rangle.\end{aligned}\quad (4.10)$$

The right hand side of Eq. (4.10) is expressed as a perturbation series in H_1 , which can be truncated to determine the expectation value approximately. Wick's theorem describes the way in which re-ordering the time ordered operators into normal

ordered operators (which vanish) generates residual contraction terms (due to the non-commutativity of fermionic operators). The expansion is then entirely composed of these contracted terms [48, 49, 50].

The Green's Function

So far, the operator \hat{O} has been unspecified. We now introduce the Green's function G . G is an important operator because other observables can be obtained from it. The Green's function is defined as:

$$G_{i,j}(t, t') = \frac{-i\langle\psi_0|T[\hat{c}_i(t)\hat{c}_j^\dagger(t')]| \psi_0\rangle}{\langle\psi_0|\psi_0\rangle}, \quad (4.11)$$

where $\hat{c}_i, \hat{c}_i^\dagger$ are the annihilation and creation operators for an electron in state i . $\hat{c}_i(t)$ is defined in the Heisenberg picture:

$$\hat{c}_i(t) = e^{iHt}\hat{c}_i e^{-iHt}. \quad (4.12)$$

The expectation of an operator \hat{O} can be found with the knowledge of G :

$$\langle\hat{O}\rangle = i \lim_{t' \rightarrow t} \text{Tr}[\hat{O}\hat{G}(t, t')]. \quad (4.13)$$

When the Green's function is inserted into the expansion of Eq. (4.10), it is possible to associate each one of the contracted terms with a Feynman diagram. These diagrams can be constructed on physical grounds, and so in principle one can carry out the series expansion by writing down all of the appropriate diagrams.

The $j = 0$ term in the expansion 4.10 corresponds to the unperturbed Green's function G_0 , which is known. Each subsequent term in the expansion corresponds to a particular physical process involving the perturbation H_1 . A single instance of

this physical process can be denoted by Σ (an example of such a process could be scattering off a impurity). The Green's function obtained from including a single such process is:

$$G = G_0 + G_0 \Sigma G_0 . \quad (4.14)$$

The effect of iterating this process over and over is captured by the Dyson equation:

$$G = G_0 + G_0 \Sigma G_0 + G_0 \Sigma G_0 \Sigma G_0 + \dots = G_0 + G_0 \Sigma G \quad (4.15)$$

$$\Rightarrow G = \frac{G_0}{1 - \Sigma} = \frac{1}{E - H_0 - \Sigma} . \quad (4.16)$$

In general to describe a perturbation H_1 , it is necessary to calculate Σ in some approximation, and apply the Dyson equation. More details and examples of the application of this formalism can be found in standard textbooks [48, 49, 50].

4.2 Nonequilibrium Green's function

Formally, Eq. (4.10) describes a situation in which the perturbation is turned off at $t = -\infty$ and the ground state is $|\psi_0\rangle$; the perturbation is adiabatically turned on, and the operator expectation value is evaluated at some finite time, and then the perturbation is adiabatically turned off. The time contour of the propagator is simply begins at $t = -\infty$ and ends at $t = \infty$. Properties are calculated at intermediate times for which interactions play a role. As mentioned previously, implicit in this formalism is the assumption that when the perturbation is turned off, the state returns to its original ground state (within a phase factor). However, for certain types of perturbations, this assumption may not be satisfied, and it is necessary to reformulate the perturbation scheme. The essential idea is to adiabatically turn on the perturbation, evaluate quantities of interest, and then reverse the time contour

back to $t = -\infty$. By doing this we are assured that the system returns to its ground state at the end of the propagator's time contour. The contour of the propagator S then has the following form shown in Fig. (4.1), and is referred to as the Keldysh contour.

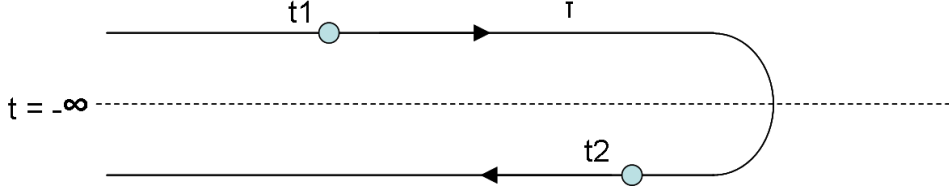


Figure 4.1: The Keldysh contour.

The development of the theory of nonequilibrium Green's functions is formally identical with the equilibrium case, with the exception that the time contour is now along the Keldysh contour. In particular, the propagator S is defined as before, but now on the Keldysh contour:

$$S(\tau, \tau') = \sum_{n=0}^{\infty} \frac{1}{n!} \int_{\tau}^{\tau'} d\tau_1 \cdots \int_{\tau}^{\tau'} dt_n T_C[\hat{H}_1(\tau_1) \cdots \hat{H}_1(\tau_n)] . \quad (4.17)$$

The time label τ is reserved for points along the contour. The time ordering operator T_C orders operators such that operators further along the contour are to the left of those earlier along the contour. The relation between Heisenberg and interaction picture operators is identical to the earlier version, now evaluated on the contour (compare Eq. (4.9)):

$$\begin{aligned} \langle \hat{O}_H(\tau) \rangle &= \frac{1}{\langle \psi_0 | S | \psi_0 \rangle} \langle \psi_0 | \sum_{j=0}^{\infty} \left(\frac{-i}{\hbar} \right)^j \frac{1}{j!} \int_C d\tau_1 \cdots \\ &\quad \cdots \int_C d\tau_j T_C[\hat{H}_1(\tau_1) \cdots \hat{H}_1(\tau_j) \hat{O}_I(\tau)] | \psi_0 \rangle . \end{aligned} \quad (4.18)$$

As before, we are interested in the Green's function, now with time arguments defined on the contour:

$$G_{i,j}(\tau, \tau') = \frac{-i\langle\psi_0|T_C[\hat{c}_i(\tau), \hat{c}_j^\dagger(\tau')]| \psi_0\rangle}{\langle\psi_0|\psi_0\rangle} . \quad (4.19)$$

The Green's function possesses a perturbation expansion based on a Wicks theorem, as in the equilibrium case. Since the contour consists of a forward and a backward branch, it is necessary to introduce different Green's functions to distinguish between the possible cases of the 2 time arguments (this is the major source of complication for the nonequilibrium case):

$$G(\tau, \tau') = \begin{cases} G^<(\tau, \tau') & \text{if } \tau \text{ on upper contour, } \tau' \text{ on lower ;} \\ G^>(\tau, \tau') & \text{if } \tau \text{ on lower contour, } \tau' \text{ on upper ;} \\ G^T(\tau, \tau') & \text{if } \tau, \tau' \text{ both on upper contour ;} \\ G^{\bar{T}}(\tau, \tau') & \text{if } \tau, \tau' \text{ both on lower contour .} \end{cases} \quad (4.20)$$

Where we have introduced the lesser Green's function:

$$G^<(t, t') = i\langle\hat{c}^\dagger(t')\hat{c}(t)\rangle , \quad (4.21)$$

the greater Green's function:

$$G^>(t, t') = -i\langle\hat{c}(t)\hat{c}^\dagger(t')\rangle , \quad (4.22)$$

the time ordered Green's function:

$$G^T(t, t') = -i\langle T[\hat{c}(t)\hat{c}^\dagger(t')]\rangle , \quad (4.23)$$

and the anti-time ordered Green's function:

$$G^T(t, t') = -i\langle T[\hat{c}(t)\hat{c}^\dagger(t')] \rangle . \quad (4.24)$$

This overall Green's function, with its 4 components, is referred to as the Keldysh Green's function. It is also convenient to define the advanced and retarded Green's functions

$$G^a(t, t') = -i\theta(t - t')\langle \{\hat{c}(t), \hat{c}^\dagger(t')\} \rangle = \theta(t' - t)[G^<(t, t') - G^>(t, t')] ; \quad (4.25)$$

$$G^r(t, t') = i\theta(-t + t')\langle \{\hat{c}(t), \hat{c}^\dagger(t')\} \rangle = \theta(t - t') [G^>(t, t') - G^<(t, t')] . \quad (4.26)$$

Of particular importance is $G^<$. This component of the Keldysh Green's function yields information about observables:

$$\langle \hat{O} \rangle = -i \lim_{t \rightarrow t'} \text{Tr}[G^<(t, t')\hat{O}] . \quad (4.27)$$

The machinery described in this thesis essentially describes the calculation of $G^<$ for various systems under equilibrium and nonequilibrium situations.

Matrix multiplication on the Keldysh contour can be broken up into its analytic pieces, according to Langreth's rules [51]. For example, the matrix multiplication on the contour given by:

$$A(\tau, \tau') = \int_C d\tau'' B(\tau, \tau'')C(\tau'', \tau') \quad (4.28)$$

Can be expressed in terms of Keldysh components as:

$$A^{\geq}(t, t') = \int_{-\infty}^{\infty} dt'' B^r(t, t'')C^{\leq}(t'', t') + \int_{-\infty}^{\infty} dt'' B^{\geq}(t, t'')C^a(t'', t') \quad (4.29)$$

$$A^{R/A}(t, t') = \int_{-\infty}^{\infty} dt'' B^{R/A}(t, t'')C^{R/A}(t'', t'). \quad (4.30)$$

Omitting the integration signs, the above may be written more succinctly as $A^{\gtrless} = B^r C^{\lessgtr} + B^{\gtrless} C^a$. For a triple product of the form $D = ABC$ on the contour, iterating Langreth's rules leads to the useful result:

$$D^< = A^r B^r C^< + A^r B^< C^a + A^< B^a C^a . \quad (4.31)$$

As before, the Green's function satisfies a Dyson equation on the contour :

$$G = G_0 + G_0 \Sigma G . \quad (4.32)$$

Using Eq. (4.31), the lesser component is given by:

$$G^< = G_0^r \Sigma^r G^< + G_0^a \Sigma^< G^r + G_0^< \Sigma^a G^a . \quad (4.33)$$

Iterating this equation for $G^<$ once yields:

$$G^< = (1 + G_0^r \Sigma^r) G_0^< (1 + \Sigma^a G^a) + (G_0^r + G_0^r \Sigma^r G_0^r) \Sigma^< G^a + G_0^r \Sigma^r G_0^r \Sigma^r G^< . \quad (4.34)$$

The above can be iterated infinitely and written in closed form:

$$G^< = (1 + G^r \Sigma^r) G_0^< (1 + G^a \Sigma^a) + G^r \Sigma^< G^a . \quad (4.35)$$

The first term of Eq. (4.35) is a boundary condition term and is not relevant for the steady state solution [51, 52]. Omitting it leads to the final result:

$$G^< = G^r \Sigma^< G^a . \quad (4.36)$$

This is known as the Keldysh equation, and is the central result of this formal development.

4.3 Application to the 2-probe geometry

To give an example of this formalism which is especially useful to the main body of the thesis, we consider a finite system which is connected to two semi-infinite leads. This calculation was done initially by C. Caroli et al. in Ref. [53]. The Hamiltonian describing this system is taken to be a simple single particle 1-d tight binding model for simplicity. Generalizations to multi-band and/or multidimensional systems are, in principle, straightforward.

$$H_C = \sum_{\langle i,j \rangle} t_{(i,j)} c_i^\dagger c_j ; \quad (4.37)$$

$$H_L = \sum_{\langle \alpha,\beta \rangle \in L} t_{(\alpha,\beta)} d_\alpha^\dagger d_\beta + \sum_{\langle \alpha,\beta \rangle \in R} t_{(\alpha,\beta)} d_\alpha^\dagger d_\beta ; \quad (4.38)$$

$$H_I = \sum_{\langle i,\alpha \in L \rangle} t_{(i,\alpha)} c_i^\dagger d_\alpha + \sum_{\langle i,\alpha \in R \rangle} t_{(i,\alpha)} c_i^\dagger d_\alpha . \quad (4.39)$$

Here the c operators are defined for center region, and the d operators for the leads. i, j, α, β are arbitrary labels, but we eventually take them to be site labels. H_C is the Hamiltonian for the central region or system (which is finite), H_L is the Hamiltonian for the left and right leads, and H_I describes the coupling between system and leads. The total Hamiltonian is $H = H_C + H_L + H_I$.

The task is to calculate the Green's functions $G^<$ and G^r of the center region. This can be accomplished by the equation of motion method. It is useful to first record a number of commutators that will be used in the derivation (For simplicity we only consider coupling to the R lead.):

$$[c_n, H] = \sum_j c_n (t_{j,n} + t_{n,j}) + \sum_\alpha d_\alpha t_{n,\alpha} ; \quad (4.40)$$

$$[d_\gamma, H] = \sum_\alpha d_\gamma (t_{\alpha,\gamma} + t_{\gamma,\alpha}) + \sum_i t_{\gamma,i} c_i . \quad (4.41)$$

In the equation of motion method, expressions for G^r and $G^<$ are found from evaluating the time derivative of G_r :

$$G_{n,m}^r(t, t') = -i\theta(t - t')\langle\{c_n(t), c_m^\dagger(t')\}\rangle \quad (4.42)$$

$$\Rightarrow i\frac{\partial G_{n,m}^r(t, 0)}{\partial t} = \delta(t)\langle\{c_n(t), c_m^\dagger(t')\}\rangle + \theta(t - t')\langle\{[c_n(t), H], c_m^\dagger(0)\}\rangle \quad (4.43)$$

Using the commutators of Eq. (4.40), the 2nd term of Eq. (4.43) becomes:

$$\begin{aligned} \theta(t)\langle\{[c_n(t), H], c_m^\dagger(0)\}\rangle &= \theta(t)\sum_j(t_{n,j} + t_{j,n})\langle\{c_j, c_m^\dagger\}\rangle + \theta(t)\sum_\alpha t_{n,\alpha}\langle\{d_\alpha, c_m^\dagger\}\rangle \\ &= (H_C G^r)_{n,m} + (H_I \Gamma)_{n,m} . \end{aligned} \quad (4.44)$$

Where we have defined

$$\Gamma_{\gamma,m}(t, t') = -i\theta(t - t')\langle\{d_\gamma(t), c_m^\dagger(t')\}\rangle . \quad (4.45)$$

Combining Eq. (4.43-4.45) leads to an expression for $\partial_t G^r$:

$$[(i\partial_t - H_C)G^r(t)]_{n,m} = \delta(t)\delta_{n,m} + (H_I \Gamma(t))_{n,m} . \quad (4.46)$$

We now proceed to differentiate Γ with respect to time:

$$\frac{\partial \Gamma}{\partial t} = \delta(t)\langle\{d_\gamma(t), c_m^\dagger(t')\}\rangle + \theta(t)\langle\{[d_\gamma(t), H], c_m^\dagger(0)\}\rangle . \quad (4.47)$$

Using Eq. (4.41), the 2nd term of Eq. (4.47) is written

$$\langle\{[d_\gamma(t), H], c_m^\dagger(0)\}\rangle = \sum_\alpha (t_{\alpha,\gamma} + t_{\gamma,\alpha})\langle\{d_\gamma, c_m^\dagger\}\rangle + \sum_i t_{\alpha,i}\langle\{c_i, c_m^\dagger\}\rangle . \quad (4.48)$$

Plugging this into Eq. (4.47), we obtain an expression for $\partial_t \Gamma$:

$$\begin{aligned} \frac{\partial \Gamma_{\gamma,m}}{\partial t} &= \delta(t) \langle \{d_\gamma, c_m^\dagger\} \rangle + \theta(t) \sum_\alpha (t_{\alpha,\gamma} + t_{\gamma,\alpha}) \langle \{d_\gamma, c_m^\dagger\} \rangle \\ &\quad + \theta(t) \sum_i t_{\alpha,i} \langle \{c_i, c_m^\dagger\} \rangle \end{aligned} \quad (4.49)$$

$$= (H_R \Gamma)_{\gamma,m} + (H_I^\dagger G^r)_{\gamma,m} . \quad (4.50)$$

Collecting terms, we obtain:

$$[(i\partial_t - H_R)\Gamma]_{\gamma,m} = (H_I^\dagger G^r)_{n,m} . \quad (4.51)$$

This inhomogeneous partial differential equation for Γ can be solved with the aid of the Green's function for the differential operator $(i\partial_t - H_R)$, denoted by G_R^r :

$$[(i\partial_t - H_R)G_R^r(t)]_{nm} = \delta(t)\delta_{n,m} . \quad (4.52)$$

Notice the G_R^r is nothing but the retarded Green's function for the isolated right lead. Γ is then given by:

$$\Gamma = \int dt_1 G_R^r(t - t_1) H_I^\dagger G^r(t_1) . \quad (4.53)$$

Recognizing this as a convolution, we can write Γ in the energy domain as

$$\Gamma(E) = G_R^r(E) H_I^\dagger G^r(E) . \quad (4.54)$$

The previous expression for G^r (Eq. (4.46)) may also be written in energy space as:

$$[(E - H_C)G^r(E)]_{n,m} = \delta_{n,m} + (H_I \Gamma(E))_{n,m} . \quad (4.55)$$

Combining this with the previous expression for G^r , we obtain:

$$[(E - H_C)G^r(E)]_{n,m} = \delta_{n,m} + H_I G^r(E) H_I^\dagger G^r(E) . \quad (4.56)$$

This can be identified with the equation

$$G^r = G_0^r + G_0^r \Sigma^r G^r , \quad (4.57)$$

with the identification

$$\Sigma^r = H_I G_R^r(E) H_I^\dagger . \quad (4.58)$$

At this point we specify the nature of the H_I central system-lead coupling. We assume that only the edge of system couples to the edge of the lead. If we take $H_{I(0,1)} = T$, then the self energy can be written:

$$\Sigma_{11}^r = T G_R^r(E)_{(0,0)} T^\dagger . \quad (4.59)$$

This key simplification is made possible by using a real space basis.

Using this form for the self-energy, the total Green's function is then given by:

$$G^r(E) = G_0^r(E) + G_0^r(E) \Sigma^r G^r(E) \quad (4.60)$$

$$\Rightarrow G^r(E) = G_0^r(E) + G_0^r(E) (T G_R^r(E) T^\dagger + T' G_L^r(E) T'^\dagger) G^r(E) . \quad (4.61)$$

Fig. (4.2) indicates how this equation may be understood intuitively. Recall that the retarded Green's function G_{ij} may be interpreted as the amplitude for hopping to site j starting from site i . Again the geometry of the overall system is that of a finite central region connected to two semi-infinite leads. The total

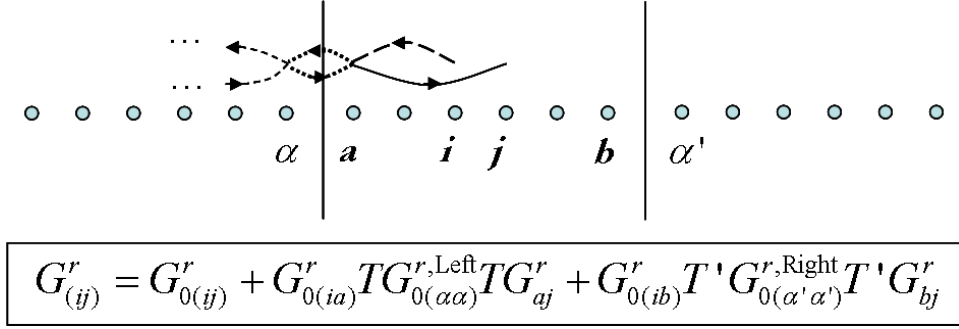


Figure 4.2: Physical interpretation of the retarded Green's function with the leads represented by self energies. The factors of the second term correspond to hopping from i to j while making excursions into the left lead, shown by the arrows in the picture.

amplitude to hop from site i to site j in the central region includes the amplitude to make that transition by hopping merely within the central region - given by G_0 - plus the amplitude for i to j transitions that are interrupted by excursions to the leads. This is represented by the 2nd term shown in Fig. (4.2). The factors in this term represent physically hopping to the edge of the central region ($G_{0(i,a)}^r$), hopping into the edge of the lead (T), hopping about the lead and back to the edge of the lead ($G_{R(\alpha,\alpha)}^r$), hopping back into the edge of the system (T^\dagger), and finally hopping to site j of the system ($G_{0(a,j)}^r$). Notice that the last Green's function is the total Green's function, so that the equation is written in Dyson-esque form.

Once Σ^r is known, we find $\Sigma^<(E)$ from the relation [40]:

$$\Sigma^<(E) = -i(\Sigma^r - \Sigma^a)f(E) \equiv \Gamma(E)f(E) . \quad (4.62)$$

Where f is again the fermi distribution function, and we have defined $\Gamma \equiv -i(\Sigma^r - \Sigma^a)$. As described earlier (see Eq. (4.27)), the density matrix is determined from

$G^<$:

$$\rho = \frac{1}{\pi} \int G^<(E) dE = \frac{1}{\pi} \int G^r(E) [\Gamma_L(E) f_L(E) + \Gamma_R(E) f_R(E)] G^a(E) dE . \quad (4.63)$$

From the above, the bias across the junction enters the formalism in the different occupation functions of the left and right leads. For energies where $f_L(E) = f_R(E)$ (both leads are occupied), the following relation holds:

$$G^r(E) [\Gamma_L(E) f_L(E) + \Gamma_R(E) f_R(E)] G^a(E) = 2\text{Im} [G^r(E)] . \quad (4.64)$$

Using this relation, we rewrite the integral of Eq. (4.63) into two parts:

$$\rho = \frac{2}{\pi} \int_{-\infty}^{E_f} \text{Im}[G^r(E)] dE + \frac{1}{\pi} \int_{E_f}^{E_f+eV} G^r(E) \Sigma^<(E) G^a(E) dE . \quad (4.65)$$

The equilibrium contribution to the density matrix ρ comes from the first term, while the nonequilibrium, or current-carrying portion comes from the 2nd term.

The integral over energy is vastly simplified by exploiting the analytic properties of $G^r(E)$. Since the poles of this function are in the lower half of the complex plane, the integral can be performed over a semi-circle in the upper half complex plane. The integrand is a smooth function in this energy region [54], so that it can be evaluated accurately with less sampling than would be required to do the integral along the real axis. The nonequilibrium portion of the integral for ρ is not analytic, and so must be performed directly along the real axis.

Once ρ is determined, all other observables \hat{O} can be found, as explained in Sec. (4.2).

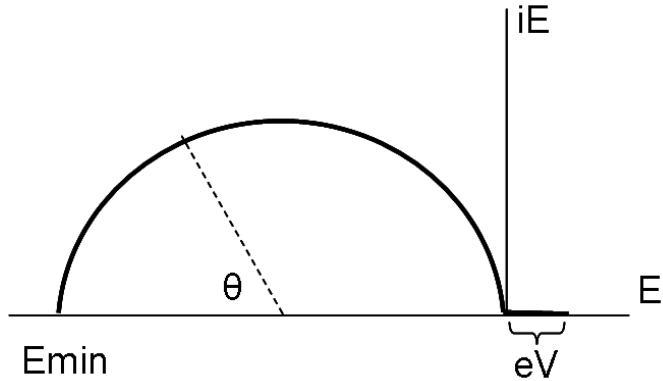


Figure 4.3: Contour integration for the Green’s function. In the complex plane, the integral is evaluated using Gaussian quadrature with 20-40 points, while the nonequilibrium portion is evaluated along the real axis.

4.4 Implementation

The description of the calculation of the density matrix in nonequilibrium systems has so far been fairly general. We now specify its application for a mean-field, self-consistent Hamiltonian described within an LCAO basis. All of the expressions in the previous section are applicable for a multi-orbital basis set. The aspects of the calculation that require further examination are the boundary conditions of the self-consistent potential, and the calculation of self-energies. These details are explained in the following sections.

4.4.1 Boundary conditions

A key ingredient in our calculation is the treatment of boundary conditions at the system-lead interface. We make the ansatz that the charge density at the edge of the system has relaxed to its bulk value. (We refer to this ansatz as the “bulk-relaxation approximation”). The screening length of metals is on the order of 0.1 –

1.0 nm (see Table (3.1)), so this approximation is well-founded in metals. To impose this condition, we solve the Hartree equation for the center region with boundary conditions:

$$V_H^{\text{system}}|_{z=0} = V_H^{\text{Left bulk}} \quad (4.66)$$

$$V_H^{\text{system}}|_{z=L} = V_H^{\text{Right bulk}} . \quad (4.67)$$

We have found that imposing this condition on the Hartree potential ensures that the charge densities, and therefore the total effective potential, matches smoothly across the boundary [54]. It is necessary to include several buffer layers of the lead material in the center region in order to guarantee the validity of the bulk-relaxation approximation. Convergence with respect to the number of buffer layers can be tested by increasing the number of buffer layers and making sure that the results do not change.

In equilibrium, the self-consistent potential ensures that there is a common Fermi level throughout the system. In our equilibrium calculations, we shift the energies of the 2 leads to a common Fermi energy, and let the charge in the system relax to self-consistency.

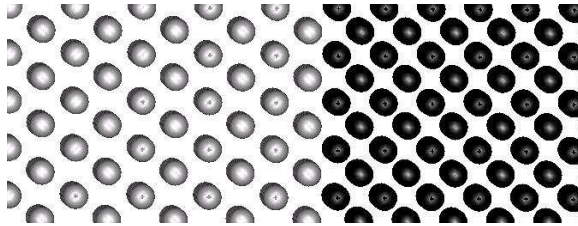


Figure 4.4: Atomic positions at a Cr-Au interface. The grey and black circles represent Au and Cr atoms, respectively. The interface is assumed to be flat, and transverse periodic boundary conditions are used.

Here we consider a single bulk Chromium - bulk Gold interface as an exam-

ple which demonstrates the validity of the bulk relaxation approximation, and the physics of the self-consistent potential. Fig. (4.4) shows the atomic coordinates at the interface. Here we consider a perfectly flat interface along the [001] crystal direction. Fig. (4.5) shows the density of states of the Cr and Au bulk leads. Here both Fermi level of both materials is set to 0. The density of charge in Au is larger than that of Cr, which is manifested by a larger total number of states below the Fermi level for Au. This mismatch in density causes a re-arrangement in the electronic distribution at the interface. This is shown in Fig. (4.5) - here charge accumulates on the first Cr layer, and is depleted from the first Au layer. The net potential drop across the interface can be estimated from the charge transfer:

$$eV = \rho d = \left(\frac{0.3C}{A} \right) 3.29 \text{ a.u.} = .902 \text{ eV} \quad (4.68)$$

This can be compared to the difference in work functions between the two materials: $\phi_{\text{Cr}} - \phi_{\text{Au}} = 5.28 - 4.44 = .84 \text{ eV}$.

Fig. (4.6) illustrates the matching of the charge density at the edge of the sample and the bulk lead for the same calculation. It is clear that the bulk-relaxation approximation holds very well for this system.

4.4.2 Self-energy calculation

Another component of our method involves the calculation of self-energy terms, which represent the coupling of the central system to the leads. This self-energy is given by the expression

$$\Sigma_{nm}^r(E) = H_{I(n,\gamma)} G_R^r(E)_{(\gamma,\beta)} H_{I(\beta,m)} \cdot \quad (4.69)$$

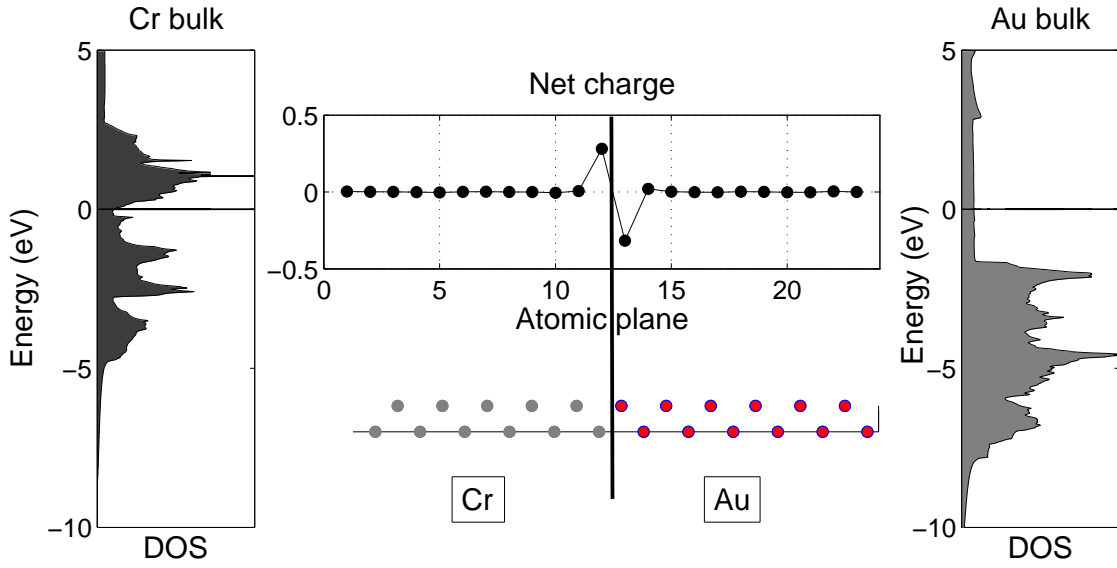


Figure 4.5: Energy shifts of bulk leads and the ensuing charge transfer in 2-probe geometry, for a system of semi-infinite Cr adjacent to semi-infinite Au.

Here Greek indices γ, β refer to sites in the lead, while indices n, m refer to sites in the central system. $G_R^r(E)$ is the Green's function of the semi-infinite lead:

$$(E - H_R)G_R^r(E) = 1 . \quad (4.70)$$

The lead-system coupling H_I connects only sites at the edge of the system and at the edge of the lead. For this reason, it is necessary only to calculate the components of G_R^r at the edge. To determine these edge components (or the “surface” Green's function), we first write the periodic Hamiltonian for the semi-infinite left lead in

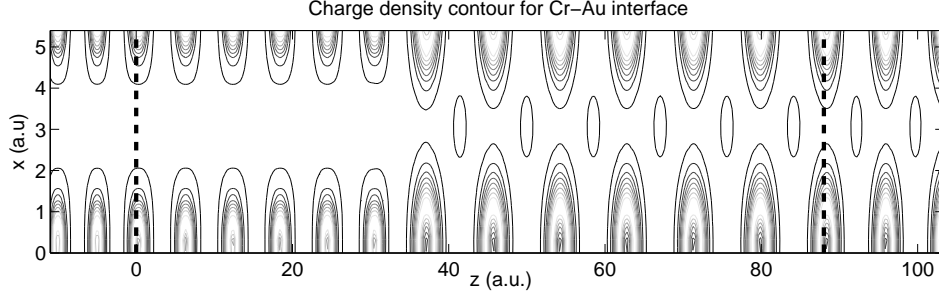


Figure 4.6: Charge density through a slice of real space for Cr-Au system. The black dotted lines indicate the system-lead boundaries, and indicate that the charge density is continuous at the boundary.

the form:

$$H_L = \begin{pmatrix} \ddots & \ddots & \ddots & 0 \\ & H_{l+1,l} & H_{l,l} & H_{l,l+1} \\ & 0 & H_{l,l-1} & H_{l,l} \end{pmatrix}. \quad (4.71)$$

The size of the periodic $H_{l,l}$ block is taken to be large enough so that blocks only interact with nearest neighbors. (So that $H_{l,l+2} = 0$, for example).

The total equation for the lead Green's function is given as:

$$\begin{pmatrix} \ddots & \ddots & 0 \\ H_{l+1,l} & E - H_{l,l} & H_{l,l+1} \\ 0 & H_{l,l-1} & E - H_{l,l} \end{pmatrix} \begin{pmatrix} \ddots & \ddots & G_{-2,0} \\ G_{-1,-2} & G_{-1,-1} & G_{-1,0} \\ G_{0,-2} & G_{0,-1} & G_{0,0} \end{pmatrix} = I. \quad (4.72)$$

Because we have taken $H_{l,l}$ to be large enough, we only need to find the $G_{0,0}$ element of G . To do so, we use the method described in Ref. [55]. The basic idea is to multiply the two matrices in Eq. (4.72) together and determine a recurrence relation for $G_{0,0}$. This recurrence is infinite, but can be truncated at some level to

obtain an arbitrarily accurate value of $G_{0,0}$.

Once $\Sigma_{L/R}$ is determined for the left/right leads, the Green's function is obtained by direct matrix inversion:

$$G^R(E) = (E + i\eta - H_C - \Sigma_L - \Sigma_R)^{-1}. \quad (4.73)$$

4.4.3 Calculating the transmission

Once G is determined, the transmission probability T is found from the Fisher-Lee relation. Here we quote the result, from Ref. [56]:

$$T = \text{Tr} [\Gamma_L G^R \Gamma_R G^A], \quad (4.74)$$

where $\Gamma_{L/R} = i(\Sigma^R - \Sigma^A)_{L/R}$. In systems with transverse periodicity in the x, y directions, all of the quantities above have a k_x, k_y dependence, and all quantities must be integrated over k_x and k_y . (Typically this requires a very fine integration mesh, with at least $N_{k_x} N_{k_y} > 10^4$ for transverse Brouillon zone areas of $(\pi/3\text{\AA})^2$.) The main computational bottleneck is evaluating Eqs. (4.73) and (4.74) for a sufficient number of energies and k_{\parallel} .

Chapter 5

Density Functional Theory

5.1 Introduction

Electronic degrees of freedom in a solid are described by the many body non-relativistic Schrödinger equation $H\Psi = i\partial_t\Psi$ with the Hamiltonian:

$$H = -\frac{\hbar^2}{2m}\nabla^2 - \sum_{i,K} \frac{Z_K e^2}{|\mathbf{r}_i - \mathbf{R}_K|} + \frac{1}{2} \sum_{i \neq j} \frac{e^2}{|\mathbf{r}_i - \mathbf{r}_j|} \quad (5.1)$$

The Hamiltonian 5.1 contains terms describing the kinetic energy, the potential of the lattice, and the electron-electron interaction energy, which we denote by \hat{T} , \hat{V} , and \hat{U} , respectively. The wave function $\Psi(\mathbf{r}_1, \dots, \mathbf{r}_N)$ must be anti-symmetric according to Fermi statistics:

$$\hat{P}[\Psi(\mathbf{r}_1, \dots, \mathbf{r}_N)] = (-1)^R \Psi(\mathbf{r}_1, \dots, \mathbf{r}_N) \quad (5.2)$$

Where \hat{P} is a permutation operator of rank R . Eq. (5.1) represents the “theory of everything” for electrons in molecular and solid-state systems. However the many-body nature of the system generally makes the exact problem intractable. In his Nobel prize speech, Walter Kohn speaks of the “exponential wall” that is encoun-

tered in approaching the problem directly: if the number of electrons is N , and each electron is described by M parameters (for example $M = 2$ for spin) the Hilbert space of the fully interacting system is M^N . Today's most powerful computers can handle up to $N = 10$ (for $M = 3$), and so for solid state systems a direct approach is obviously not feasible. The source of the difficulty is the many-body nature of the system, or the electron-electron interaction. Approximations usually treat the interaction term in a mean-field fashion, such as in Hartree-Fock theory. This chapter describes an approach known as density functional theory (DFT). While implementations of DFT often have the structure of a mean field theory, its formal justification is different.

This chapter is organized as follows: In Sec. (5.2) we state and prove the Hohenberg-Kohn theorem, which is central to DFT. We then describe the Kohn-Sham scheme and local density approximation. In Sec. (5.3), we describe the pseudopotential approximation employed in this work, while in Sec. (5.4), we describe the atomic orbital basis set used. In Sec. (5.5), we describe the solution procedure for finding self-consistent ground states of the Kohn-Sham equations. Finally, in Sec. (5.6), we describe the exchange-correlation functionals used in this work, which include noncollinear spin dependence. We omit details regarding the evaluation of matrix elements with our basis set. We employ the same methods as described in detail in Ref. [10].

5.2 General formulation - Hohenberg Kohn theorem

The Hohenberg-Kohn (H-K) theorem [57] is the central theoretical underpinning for density functional theory. The theorem states that the electronic charge density of a system's ground state $\rho(\mathbf{r})$ uniquely determines the external potential and electron number - implicitly determining all observable properties of the system. Clearly the external potential and electron number determine the ground state density from Eq.

(5.1), but the HK theorem states that this mapping is one-to-one and invertible:

$$\{V_{ext}(\mathbf{r}), N\} \leftrightarrow \rho(\mathbf{r}) . \quad (5.3)$$

The proof is simple (we will consider a nondegenerate ground state here, although the theorem holds for degenerate ground states as well [58]): suppose a system of N electrons with potential $V_1(\mathbf{r})$ and Hamiltonian \hat{H}_1 has a ground state wave function Ψ_1 with energy E_1 and density $\rho(\mathbf{r})$. Then E_1 is given by:

$$E_1 = \langle \Psi_1 | \hat{H}_1 | \Psi_1 \rangle = \langle \Psi_1 | \hat{T} + \hat{U} | \Psi_1 \rangle + \int d\mathbf{r} V_1(\mathbf{r}) \rho(\mathbf{r}) . \quad (5.4)$$

Now suppose there is a second potential $V_2(\mathbf{r})$ which differs from V_1 by more than an additive constant, with a ground state wave function Ψ_2 , energy E_2 , and the *same* density $\rho(\mathbf{r})$. Again we have:

$$E_2 = \langle \Psi_2 | \hat{T} + \hat{U} | \Psi_2 \rangle + \int d\mathbf{r} V_2(\mathbf{r}) \rho(\mathbf{r}) . \quad (5.5)$$

Since Ψ_1 is the ground state for H_1 , we have the inequality

$$\begin{aligned} E_1 < \langle \Psi_2 | \hat{H}_1 | \Psi_2 \rangle &= \langle \Psi_2 | \hat{T} + \hat{U} | \Psi_2 \rangle + \int d\mathbf{r} V_1(\mathbf{r}) \rho(\mathbf{r}) \\ &= E_2 + \int d\mathbf{r} (V_1(\mathbf{r}) - V_2(\mathbf{r})) \rho(\mathbf{r}) . \end{aligned} \quad (5.6)$$

By the same token:

$$\begin{aligned} E_2 < \langle \Psi_1 | \hat{H}_2 | \Psi_1 \rangle &= \langle \Psi_1 | \hat{T} + \hat{U} | \Psi_1 \rangle + \int d\mathbf{r} V_2(\mathbf{r}) \rho(\mathbf{r}) \\ &= E_1 + \int d\mathbf{r} (V_2(\mathbf{r}) - V_1(\mathbf{r})) \rho(\mathbf{r}) . \end{aligned} \quad (5.7)$$

Adding Eq. (6.1) and (5.8) results in a contradiction:

$$E_1 + E_2 < E_1 + E_2 . \quad (5.8)$$

Therefore the assumption that two different external potentials V_1 and V_2 can yield the same ground state density $\rho(\mathbf{r})$ is false. $\rho(\mathbf{r})$ therefore uniquely determines the potential V - or the potential is unique functional of the ground state density. This proves that the potential and particle number are a one-to-one, invertible function of the ground state density, proving the theorem. (Again this proof is valid provided that the ground state of the system in question is not degenerate.)

Since the ground state energy is a functional of the density (denoted by $E[\rho(\mathbf{r})]$), both ρ and E can be determined with a variational approach.

$$E = \min_{\rho(\mathbf{r})} E[\rho(\mathbf{r})] , \quad (5.9)$$

where

$$E[\rho(\mathbf{r})] = \int d\mathbf{r} V(\mathbf{r})\rho(\mathbf{r}) + F[\rho(\mathbf{r})] , \quad (5.10)$$

and $F[\rho]$ is given by

$$F[\rho] = \min_{\alpha} [\langle \Psi_{\rho}^{\alpha} | \hat{T} + \hat{U} | \Psi_{\rho}^{\alpha} \rangle] . \quad (5.11)$$

The minimization in Eq. (5.11) is over all many-body wave functions Ψ_{ρ}^{α} which yield the ground state density ρ . F is a universal function of ρ which is independent of the particular potential V of the system. The exact determination of F is equally intractable as the diagonalization of the original many-body Hamiltonian. However, approximations are more easily accessible since it is a functional of only a 3-dimensional real function.

The simplest functional for F is provided by Thomas-Fermi theory [58] (which was developed before the H-K theorem). In this case, the kinetic and electrostatic energies are derived from a free electron gas, with the result

$$E_{TF}[\rho] = \frac{3(3\pi^2)^{2/3}}{10} \int d\mathbf{r} \rho^{5/3}(\mathbf{r}) + \frac{1}{2} \int d\mathbf{r} d\mathbf{r}' \frac{\rho(\mathbf{r})\rho(\mathbf{r}')}{|\mathbf{r} - \mathbf{r}'|} . \quad (5.12)$$

Thomas-Fermi theory provides an illustrative example of potential difficulties in formulating an accurate density functional theory. It is well known that Thomas-Fermi theory suffers from serious deficiencies, in particular it predicts that atoms never bond into molecules [58]. The central defect is the treatment of the kinetic energy. Recent work has gone into finding more accurate forms for the kinetic energy functional, but usually the problem is circumvented by using Kohn-Sham equations.

5.2.1 Kohn-Sham equations

In the Kohn-Sham formulation of density functional theory [59], the functional F is given as:

$$F[\rho(r)] \equiv T_s[\rho(r)] + \frac{1}{2} \int \frac{\rho(r)\rho(r')}{|r - r'|} dr dr' + E_{xc}[\rho(r)] , \quad (5.13)$$

where $T_s[\rho(r)]$ is the kinetic energy of *non-interacting* electrons with a total density ρ . The motivation for this definition is that it gives a much better approximation to the kinetic energy, which typically comprises a large part of the total energy [60]. The above form of F serves as a *definition* of E_{xc} . E_{xc} contains all of the non-classical contributions to the energy. The total energy is then given by:

$$E = \int dr V(r)\rho(r) + T_s[\rho(r)] + \frac{1}{2} \int \frac{\rho(r)\rho(r')}{|r - r'|} dr dr' + E_{xc}[\rho(r)] . \quad (5.14)$$

In the Kohn-Sham scheme, $\rho(\mathbf{r})$ is represented with basis functions $\{\phi_i(\mathbf{r})\}$, which are usually taken to be orthogonal:

$$\rho(\mathbf{r}) = \sum_{i=1}^N |\phi_i(\mathbf{r})|^2 \quad (5.15)$$

$$\langle \phi_i^*(\mathbf{r}) | \phi_j(\mathbf{r}) \rangle = \delta_{ij} . \quad (5.16)$$

The total energy 5.14 is minimized by the ground state. In terms of $\{\phi_i\}$, this minimization condition is

$$\frac{\delta E[\rho]}{\delta \phi_i(\mathbf{r})} = 0 . \quad (5.17)$$

The orthogonality condition is imposed by introducing Lagrange multipliers E^i :

$$\frac{\delta E[\rho]}{\delta \phi_i(\mathbf{r})} - E^i \phi_i(\mathbf{r}) = 0 . \quad (5.18)$$

The functional 5.14 is then extremized with respect to $\phi_i(\mathbf{r})$, $\delta E/\delta \phi_i(\mathbf{r})$, yielding the Kohn-Sham equations:

$$\left(-\frac{1}{2} \nabla^2 + v_{\text{eff}}(\mathbf{r}) - \epsilon_i \right) \phi_i(\mathbf{r}) = 0 ; \quad (5.19)$$

$$v_{\text{eff}}(\mathbf{r}) = V(\mathbf{r}) + \int \frac{\rho(\mathbf{r}')}{|\mathbf{r} - \mathbf{r}'|} d\mathbf{r}' + v_{xc}(\mathbf{r}) . \quad (5.20)$$

Where the exchange correlation energy is given by

$$v_{xc}(\mathbf{r}) = \frac{\delta}{\delta \rho(\mathbf{r})} E_{xc}[\rho(\mathbf{r})] . \quad (5.21)$$

The interacting problem is now simplified into a set of non-interacting Schrödinger equations with an effective potential which has to be determined self-consistently. These equations have much the same structure as the Hartree-Fock equations, except

that the Hartree-Fock exchange potential is non-local in space. The formulation for the ground state is still in principle exact. As discussed in the next section, approximations of E_{xc} are needed for practical implementation of the K-S equations. The effective Hamiltonian depends on the solutions $\{\phi_i\}$ through $\rho(\mathbf{r})$, so the structure of these equations is that of a self-consistent mean field theory. The solution of these equations is a difficult task, and we discuss their solution in the remainder of this chapter.

5.2.2 Total energy

The expression Eq. (5.14) for the total energy can be re-written as

$$E_{\text{tot}} = E_{\text{BS}} + \delta E_H + \delta E_{xc} + E_{\text{ion-ion}} . \quad (5.22)$$

Where E_{BS} represents the single particle contribution to the energy:

$$E_{\text{BS}} = \sum_i^N E_i , \quad (5.23)$$

and the Kohn-Sham eigenvalues E_i are:

$$E_i = \int d\mathbf{r} (\phi_i(\mathbf{r}))^* \left\{ \frac{-\nabla^2}{2} + \int d\mathbf{r}' \frac{\rho(\mathbf{r}')}{|\mathbf{r} - \mathbf{r}'|} + V_{xc}(\rho(\mathbf{r})) + V_{\text{ion-el}} \right\} \phi_i(\mathbf{r}) . \quad (5.24)$$

The remaining terms represent double counting corrections to the single particle energy (δE_H) and the exchange correlation energy (δE_{xc})

$$\delta E_H = -\frac{1}{2} \int d\mathbf{r} \frac{\rho(\mathbf{r})\rho(\mathbf{r}')}{|\mathbf{r} - \mathbf{r}'|} , \quad (5.25)$$

$$\delta E_{xc} = \int d\mathbf{r} \left(\frac{E_{xc}(\mathbf{r})}{\rho(\mathbf{r})} - V_{xc}(\mathbf{r}) \right) , \quad (5.26)$$

and the last term $E_{\text{ion-ion}}$ is the electrostatic energy of the ions:

$$E_{\text{ion-ion}} = \sum_{I \neq J} \frac{Z_I Z_J}{|\mathbf{R}_I - \mathbf{R}_J|}. \quad (5.27)$$

In this work we adopt the Born-Oppenheimer approximation and assume that the ionic positions are frozen. The validity of this approximation follows from the fact that $m_{\text{ion}} \gg m_{\text{electron}}$. The proper ionic positions are obtained by minimizing the total energy. In this work we have simply taken experimental values for lattice constants and not performed this minimization (or ionic relaxation) explicitly.

5.2.3 Local density approximation

The Kohn-Sham formulation of density functional theory is, to this point, still exact. All of the complications arising from the many-body nature of the problem are contained in $E_{xc}[\rho(\mathbf{r})]$. The power of density functional theory is that approximate forms for E_{xc} are possible to construct which lead to an accurate description of real systems. The most common approximation is the local density approximation (LDA). In this approach, E_{xc} is evaluated for an electron gas with uniform density ρ , denoted by $E_{xc}^0[\rho]$. The exchange-correlation energy at each point in the real system is then taken to be $E_{xc}^0[\rho(\mathbf{r})]$. The exchange-correlation potential is then local in the sense that it depends only on the local charge density. The quality of a particular parameterization of E_{xc}^0 is determined from a practical perspective - if it leads to density functional calculations that describe a variety of experimental observations well, it is considered a good approximation. Approximation methods are also aided by certain constraints, or sum rules, that the exchange-correlation energy functional should satisfy.

There are other, more sophisticated approximations beyond LDA. By including the spin degree of freedom, a spin-dependent exchange-correlation functional is obtained - known as the local spin density approximation (LSDA). In addition, non-

local effects may be included by considering functionals that depend on the local gradient of the density in the exchange-correlation energy. This leads to a class of functionals known as “generalized gradient approximations” (GGA). The specific parameterizations of functionals are used in this work are given in Sec. (5.6) and Appendix A.

5.3 Pseudopotential approximation

As discussed in Sec. 5.2.1 The Kohn-Sham Hamiltonian is composed of the terms:

$$\hat{H}^{KS} = \hat{T} + \hat{V}^{\text{ion}} + \hat{V}^H + \hat{V}^{xc} , \quad (5.28)$$

where \hat{T} represents the single-particle kinetic energy, \hat{V}^{ion} the electrostatic interaction with the ionic lattice of the crystal. \hat{V}^H describes the electrostatic electron-electron interaction, while \hat{V}^{xc} includes the non-classical many body effects of electron-electron interactions, which as described in Sec. 5.2.3 are treated in some approximate fashion.

The pseudopotential approximation represents a significant simplification of the problem. The physical motivation for it is that the core electrons are largely inert: they do not participate in bonding and essentially only serve to screen the potential of the bare nucleus seen by the valence electrons. In the pseudopotential approximation we replace of the bare nuclear potential with a core-electron screened potential, and the remove the core electron degrees of freedom from the problem [61].

Here we describe in detail the process of constructing the pseudopotential. The pseudopotential of an atom is not unique - indeed some are better than others. The quality of a pseudopotential is determined by its transferability - that is, its ability to recreate all electron properties in a variety of chemical environments.

There are several recipes for constructing the pseudopotential; the one used in this work is that of Trouiller and Martin [62]. The procedure can be broken into 4 steps. Fig. (5.1) shows a schematic of the procedure, and each step is described below:

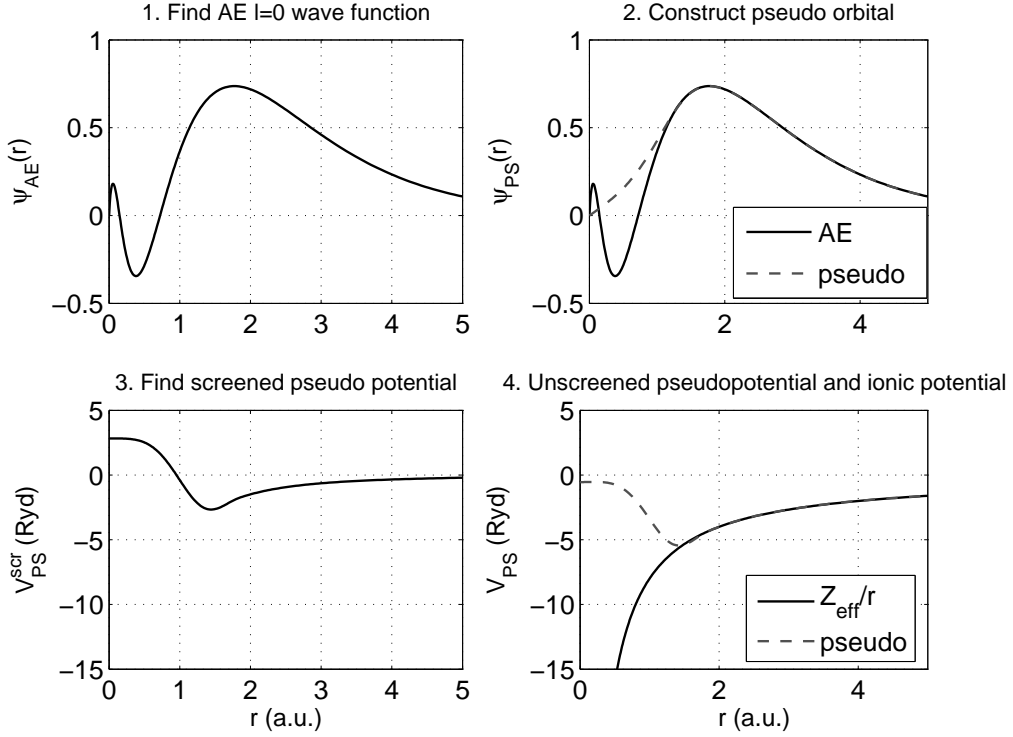


Figure 5.1: Steps in construction of the pseudopotential (shown for the $l = 0$ channel only). (1.) Find the $l = 0$ all electron (AE) orbital. (2.) Construct the pseudo-orbital according to procedure outlined in text. (3.) Find the resulting potential. (4.) Remove valence (and core) electron contributions from potential.

Step 1: We begin with the Kohn-Sham equations for a single atom, (within LDA), and consider the wave function Ψ of the form $\psi_l(r)Y_l^m(\theta, \phi)$ (the wave function has the additional constraint that it must produce a spherically symmetric

$\rho(\mathbf{r})$):

$$H_l^{\text{atom}}\psi_l = E_l\psi_l ; \quad (5.29)$$

$$H_l^{\text{atom}} = \hat{T}_l + V_{\text{bare}}^{\text{ion}}(r) + V_H[\rho(r)] + V_{xc}[\rho(r)] ; \quad (5.30)$$

$$\hat{T}_l = - \left(\frac{1}{r} \frac{\partial^2}{\partial r^2} - \frac{l(l+1)}{r^2} \right) . \quad (5.31)$$

The potential energy terms can be combined into a single term, denoted by V^{scr} (or V 'screened'):

$$V_{\text{AE}}^{\text{scr}}(r) = V_{\text{bare}}^{\text{ion}}(r) + V_H[\rho(r)] + V_{xc}[\rho(r)] ; \quad (5.32)$$

$$\Rightarrow H^{\text{atom}} = \hat{T}_l + V_{\text{AE}}^{\text{scr}}(r) ; \quad (5.33)$$

the subscript 'AE' ('all-electron') refers to quantities calculated from the full solution of the above atomic Kohn-Sham equations.

Step 2: Next the pseudo valence orbitals are constructed from the all-electron valence orbitals. The pseudo orbitals are constructed to have the following properties:

1. The pseudo orbital radial function contains no nodes. This is desirable because we would like to have smooth, easily representable wave functions.
2. The pseudo orbital radial wave function should match the all-electron wave function beyond a certain cutoff radius r_c .
3. The charge enclosed within the cutoff radius r_c should be the same for pseudo and all-electron wave function.
4. The valence all-electron and pseudopotential eigenvalues should be equal.

Constraints 3 and 4 ensure that the logarithmic derivative of the all-electron and pseudo wave function agree for $r > r_c$ [61]. The logarithmic deriva-

tive is related to the phase shift associated with scattering off of a radial potential. Having the same logarithmic derivative then ensures that the scattering properties of the pseudo and all electron wave functions will be similar. In general, reducing the value of r_c will make a pseudopotential more transferable (better), at the cost of making the potential “harder”, or more difficult to represent accurately on a real space grid. Pseudopotentials that satisfy the above 4 conditions are referred to as “norm-conserving” pseudopotentials [61].

These conditions specify the generic procedure:

$$\{\psi_l\}_{\text{AE}}^{\text{val}} \rightarrow \{\psi_l\}_{\text{PS}}^{\text{val}} . \quad (5.34)$$

Here the subscript ‘PS’ signifies “pseudopotential”, the superscript “val” specifies valence orbital.

Step 3: Given $\{\psi_l\}_{\text{PS}}^{\text{val}}$, the set of new potentials $V_{l,\text{PS}}^{\text{scr}}$ is found:

$$(\hat{T}_l + V_l^{\text{PS,scr}})\psi_l^{\text{PS}} = E_l\psi_l^{\text{PS}} ; \quad (5.35)$$

$$\Rightarrow V_l^{\text{PS,scr}} = E_l - \frac{\hat{T}_l\psi_l^{\text{PS}}}{\psi_l^{\text{PS}}} . \quad (5.36)$$

Step 4: The final pseudopotential is obtained by subtracting off the contribution from the hartree and exchange terms from the pseudo orbital valence charge:

$$V_l^{\text{PS}} = V_l^{\text{PS,scr}} - V_H[\rho_{\text{PS}}^v] - V_{xc}[\rho_{\text{PS}}^v] . \quad (5.37)$$

In the case of transition metals, the valence d -electrons are localized near the atomic nucleus, so that there is significant overlap between the valence and core electron charge density. Due to the nonlinearity of the exchange/correlation potential, it is necessary to evaluate the potential using the total charge density $\rho^{\text{val}} + \rho^{\text{core}}$. In this case the the contribution to the exchange-correlation potential

from the core density is also subtracted from the screened pseudopotential (compare Eq. (5.37):

$$V_l^{\text{PS}} = V_l^{\text{PS,scr}} - V_H[\rho_{\text{PS}}^v] - V_{xc}[\rho_0^c + \rho_{\text{PS}}^v] . \quad (5.38)$$

The core density may oscillate rapidly near the atomic nucleus, making it difficult to represent on a real space grid. However, since the only relevant portion of the core charge is that which overlaps with the valence charge, the inner core electron density is replaced by a smooth function:

$$\rho_c(r) = \begin{cases} Ar^l e^{-\alpha r} & \text{if } r < r_c \\ \rho_{\text{core}}(r) & \text{if } r > r_c . \end{cases} \quad (5.39)$$

Values of r_c are between .7 and .9 a.u.

The pseudopotentials are now determined. As constructed, they are however long-range: for $r > r_c$, the pseudopotential behaves as Z_{eff}/r . To remove this long-range form from the pseudopotential, a new potential V_L is added and subtracted for each angular momentum channel l :

$$V^{PS} = V_L + \sum_{l=1}^{l_{\text{max}}} \sum_{m=-l}^{m=l} |Y_{l,m}\rangle \delta V_l^{PS} \langle Y_{l,m}| , \quad (5.40)$$

where

$$\delta V_l^{PS} = V_l^{PS} - V_L . \quad (5.41)$$

The exact form of V_L is in principle arbitrary. Following Ref. [10], the form we use for V_L is given by the potential generated by a positive charge distribution of the

form:

$$\rho^{local}(r) \propto \exp[-(\sinh(abr)/\sinh(b))^2] , \quad (5.42)$$

where the total charge of ρ^{local} is equal to the valence of the atom. The procedure outlined above is performed with a software package “ATOM” [63].

5.3.1 Seperable pseudopotentials

In the context of plane wave calculations, the semi-local form of the pseudopotential (nonlocal in angular momentum, local in space) is problematic. If there are m k -points and n basis functions, evaluation of the psuedopotential requires mn^2 integrals. Kleinman and Bylander bypassed this difficulty by constructing a pseudopotential that is fully nonlocal [64].

$$\hat{V}^{KB} = \hat{V}_L + \sum_{lm} \frac{|\delta V_l^{PS} \phi_{lm}\rangle \langle \delta V_l^{PS} \phi_{lm}|}{\langle \phi_{lm} | \delta V_l^{PS} | \phi_{lm} \rangle} \quad (5.43)$$

The resulting evaluation requires only mn integrals. We use this fully nonlocal form of the pseudopotential in this work primarily as a matter of convention, as the computational savings of this fully nonlocal form are not relevant for DFT with a LCAO basis. The Kleinman-Bylander construction can lead to unphysical ghost states in which the lowest p state is lower than the lowest s state [65].

5.3.2 Addition of screening potentials

In the previous section, we described the construction of pseudopotentials, which drastically reduce the dimensionality of the Hilbert space by sweeping the largely inert core electrons under the rug. After the use of pseudopotentials, the Hamiltonian

takes the form:

$$\hat{H} = \hat{T} + \sum_I V_L(\mathbf{r} - \mathbf{R}_I) + \sum_{I,l} V_l^{KB}(\mathbf{r} - \mathbf{R}_I) + \hat{V}_H + \hat{V}_{xc} . \quad (5.44)$$

The long range nature of V_L may be eliminated by adding and subtracting the potential V_{atom} due to the charge constructed by populating the atoms with their reference charge configuration ρ_{atom} . The resulting screened neutral atom potential $V_{NA} \equiv V_L + V_{atom}$ is short ranged (vanishes beyond the maximum orbital cutoff radius). The addition of this screening charge density ρ_{atom} modifies V_H : the net source charge is now $\rho(\mathbf{r}) - \rho_{atom}(\mathbf{r})$. The potential produced by this charge is denoted by δV_H . The final Hamiltonian then takes the form:

$$H = \hat{T} + \sum_I V_{NA}(\mathbf{r} - \mathbf{R}_I) + \sum_{I,l} V_{I,l}^{KB}(\mathbf{r} - \mathbf{R}_I) + \delta V_H(\mathbf{r}) + \hat{V}_{xc}(\mathbf{r}) , \quad (5.45)$$

where

$$\delta V_H(\mathbf{r}) = \int d\mathbf{r}' \frac{\rho(\mathbf{r}') - \rho_{atom}(\mathbf{r}')}{|\mathbf{r} - \mathbf{r}'|} , \quad (5.46)$$

$$V_{NA} = V_L + V_{atom} . \quad (5.47)$$

5.4 Basis set: Linear Combination of Atomic Orbitals

With the Kohn-Sham Hamiltonian defined, we must now specify a basis set. The basis set used in this work consists of a linear combination of atomic orbitals (LCAO). The atomic orbitals are precisely those that are constructed in forming the pseudopotential (see Eq. (5.34)). The minimal basis set for each atom in the system is

then:

$$\phi_{i,l,M}(\mathbf{r}) = R_l(|\mathbf{r} - \mathbf{R}_i|)Y_M^l(\theta, \phi) , \quad (5.48)$$

here i is the label for atom, and l is the angular momentum label ($l = 0, 1, 2, \dots$ or $l = s, p, d, \dots$). We use real spherical harmonics $|L, M\rangle$, which are related to the conventional harmonics $Y_m^l \equiv |l, m\rangle$ by

$$|l, M\rangle = \frac{1}{\sqrt{2}}(|l, m\rangle + (-1)^M |l, -m\rangle) ; \quad (5.49)$$

$$|l, \bar{M}\rangle = \frac{1}{\sqrt{2i}}(|l, m\rangle - (-1)^M |l, -m\rangle) , \quad (5.50)$$

where $M = |m|$. The basis orbitals are purely real in this representation.

To ensure the sparseness of the Hamiltonian, the orbital's radial function is taken to have a finite cutoff. There are several techniques for cutting off pseudo-orbital radial functions. The methods we use are those found in the software package Siesta [10]. In one case, a confining potential is added to the atomic Hamiltonian which is used to generate the basis orbitals. It is parameterized in the form:

$$V(r) = V_o \frac{e^{-\left(\frac{r_c - r_i}{r - r_i}\right)}}{r_c - r} \quad (5.51)$$

Where r_i and V_o are free parameters (strictly speaking defined variationally). Here r_c specifies the cutoff, r_i determines the onset of the confining potential, and V_0 its strength. The above potential diverges at $r = r_c$, ensuring the orbital is confined with r_c .

In some of the studies, we have found that the choice of basis set orbital parameters is very important. For such systems, we use a downhill simplex optimization routine to minimize the enthalpy ($E + PV$) of the system with respect to the basis set parameters described above [66].

So far we have constructed a single radial pseudo orbital for each angular momentum channel. The resulting basis set is referred to as a single- ζ basis set. The addition of more orbital basis functions generally results in more accurate calculations. One way to do this is to use more than one radial function for each angular momentum. The procedure for generating multiple- ζ basis sets is described in Ref. [67], and consists of the following steps:

1. Given an orbital wave function ϕ_0 , construct a new wave function ϕ_1 , which is identical to ϕ_0 outside some radius R_{DZ} .
2. The wave function ϕ_1 is taken to be of the form $r^l(a - br^2)$ inside R_{DZ} , with a and b ensuring continuity and differentiability at $r = R_{DZ}$. The difference between the original wave function ϕ_0 and ϕ_1 is the new atomic orbital basis function. This wave function is localized with R_{DZ} . The value of R_{DZ} is typically chosen so that a certain fraction of the charge is contained outside of R_{DZ} , typically 15%.

Usually polarization orbitals are included as well in order to increase the flexibility of the basis set. This is often taken from an angular momentum channel $l_{max} + 1$, where l_{max} is the maximum angular momentum occupied by the atomic configuration. Other examples of polarization orbitals include the atomically unoccupied $3p$ orbital of transition metal elements.

An important aspect of the basis set used here is that it is non-orthogonal:

$$S_{ij} = \int d\mathbf{r} \phi_i(|\mathbf{r} - \mathbf{R}_I|) \phi_j(|\mathbf{r} - \mathbf{R}_J|) \neq \delta_{ij}. \quad (5.52)$$

S is referred to as the overlap matrix. The non-orthogonality is generally accounted for with the replacement $E \rightarrow ES$. For example, the Schrödinger equation becomes: $H\psi = ES\psi$, the Green's function becomes: $G = (ES - H)^{-1}$, and so on.

5.5 Solution of Kohn-Sham Equations

5.5.1 The density matrix

The Kohn-Sham Hamiltonian depends on its solutions $\{\phi_i(\mathbf{r})\}$ through $\rho(\mathbf{r})$. For a system with N electrons, the charge density is obtained by filling up the lowest eigenstates of the self-consistent K-S Hamiltonian. The expectation of an operator O is then given as

$$\langle O \rangle = \sum_{i=1}^N \langle \phi_i | \hat{O} | \phi_i \rangle . \quad (5.53)$$

An alternative description of the ground state occupation of orbitals is given by the density matrix. This is defined as:

$$\hat{\rho} = \sum_i |\phi_i\rangle f(\beta(E_i - \mu)) \langle \phi_i| , \quad (5.54)$$

where μ is the chemical potential, β is inverse temperature, and $f(x)$ is the Fermi distribution function: $f(x) = (1 + e^{-x})^{-1}$. Physical observables are now obtained by tracing over the density matrix:

$$\langle O \rangle = \text{Tr} [\hat{\rho} \hat{O}] . \quad (5.55)$$

In particular, once the density matrix is calculated, the real space charge density is then given by $\rho(\mathbf{r}) = \sum_{ij} \hat{\rho}_{(ij)} \phi_i^*(\mathbf{r}) \phi_j(\mathbf{r})$.

Given the charge density, the Hartree potential is calculated by:

$$\nabla_H^2(\mathbf{r}) = \rho(\mathbf{r}) \quad (5.56)$$

$$\Rightarrow V_H(\mathbf{k}) = \rho(\mathbf{k})/\mathbf{k}^2 . \quad (5.57)$$

The contribution to the exchange-correlation potential is found by evaluating $v_{xc}[\rho(\mathbf{r})]$ for the local density. The specific form of v_{xc} we use is described in Sec. (5.6). These density-dependent potentials create a new Hamiltonian, which must again be diagonalized to find a new charge density. The process is iterated until the input and output density matrix are equal within some specified tolerance.

5.5.2 Periodic systems

In this section we discuss the treatment of infinite, periodic systems. In such a system a basic unit cell is repeated infinitely in 1 or more dimensions, so that the potential, charge density, and other physical properties are also simply repeated infinitely.

For m orbitals in the unit cell, the Hamiltonian describing the matrix elements between pairs of orbitals in the unit cell is of dimension $m \times m$ - we denote it by $H_{(0,0)}$. Orbitals in the unit cell also interact with those from neighboring cells. We denote the Hamiltonian describing the unit cell's interactions with its $+z$ neighbor is $H_{(0,1)}$; in general $H_{(0,\delta)}$ describes the interaction of the unit cell atoms with those of a neighboring cell with displacement δ .

Bloch's theorem allows for the transformation of the original infinite, periodic system into a finite one with the addition of the crystal momentum label \mathbf{k} . To describe the entire system, a sufficiently large sampling of \mathbf{k} -vectors from the Brouillon zone is required. For a given \mathbf{k} , we construct the \mathbf{k} -dependent Hamiltonian as:

$$H_{\mathbf{k}} = \sum_{\delta} H_{(0,\delta)} e^{i\mathbf{k}\cdot\delta} . \quad (5.58)$$

For each \mathbf{k} , $H_{\mathbf{k}}$ is diagonalized and the eigenvalues $\epsilon_{\mathbf{k}}$ and eigenvectors $|\psi_{\mathbf{k}}\rangle$ are found and stored. The Fermi level ϵ_F is determined by the charge density of the

system:

$$N = \frac{V}{(2\pi)^3} \int d\mathbf{k} f(\beta(\epsilon_{\mathbf{k}} - \epsilon_F)) , \quad (5.59)$$

where $f(x)$ is the fermi-dirac distribution function $(e^x + 1)^{-1}$. For each \mathbf{k} , the eigenvectors form an complete basis, and in this basis the density matrix operator $\hat{\rho}$ is diagonal. It is given by:

$$\hat{\rho}_{\mathbf{k}}^{\text{diag}} = \sum_i |\psi_{\mathbf{k},i}\rangle f(\epsilon_{\mathbf{k},i} - \epsilon_F) \langle \psi_{\mathbf{k},i}| . \quad (5.60)$$

The sum i is over eigenvectors of $H_{\mathbf{k}}$. This density matrix is transformed into the LCAO basis by a the transformation:

$$\hat{\rho}_{\mathbf{k}} = V_{\mathbf{k}} \hat{\rho}_{\mathbf{k}}^{\text{diag}} (S_{\mathbf{k}} V_{\mathbf{k}})^{-1} , \quad (5.61)$$

where $V_{\mathbf{k}}$ is a matrix of the eigenvectors of $H_{\mathbf{k}}$, and $S_{\mathbf{k}}$ is the \mathbf{k} -dependent overlap matrix. The total density matrix is given by:

$$\hat{\rho}_{\text{tot}} = \frac{1}{(2\pi)^3} \int d\mathbf{k} \hat{\rho}_{\mathbf{k}} . \quad (5.62)$$

The density matrix includes contributions from pairs of orbitals in different unit cells:

$$\hat{\rho}_{0,\delta} = \frac{1}{(2\pi)^3} \int d\mathbf{k} \hat{\rho}_{\mathbf{k}} e^{i\mathbf{k}\cdot\delta} , \quad (5.63)$$

where the factor of $e^{i\mathbf{k}\cdot\delta}$ comes from the Bloch factor of the wave function in the neighboring unit cell.

5.5.3 Self-consistent procedure

Finding the self-consistent solution to the Kohn-Sham equation is a challenging numerical task. The Hamiltonian is a highly nonlinear function of ρ : $H = A[\rho]$, while the density matrix is a function of H : $\rho = B[H]$. A self consistent $[H, \rho]$ pair satisfies:

$$\begin{aligned}\rho^* &= B[A[\rho^*]] \\ H^* &= A[B[H^*]]\end{aligned}\tag{5.64}$$

The outline of the procedure is shown in Fig. (5.2). The procedure consists first of an initial guess at the density matrix ρ_0 . This determines the initial charge density $\rho(\mathbf{r})$ and Hamiltonian. This Hamiltonian yields a new density matrix ρ_1 . Generally $\rho_0 \neq \rho_1$, and so a new trial density matrix is constructed, which is generally some combination of input and output density matrices. The simplest example is linear mixing:

$$\rho^{\text{new}} = \alpha\rho_0 + (1 - \alpha)\rho_1\tag{5.65}$$

For the systems considered in this work, simple linear mixing is usually not sufficient to obtain the self-consistent solution. We use a combination of Broyden's [68] and Pulay's [69] methods to solve Eq. (5.64).

5.6 Exchange-correlation functionals

5.6.1 LSDA

For the spin-dependent exchange-correlation functional, we use the local spin density approximation as parameterized by Perdew and Zunger in Ref. [70]. The particulars of this parameterization are given in Appendix A. The aspect of the exchange-

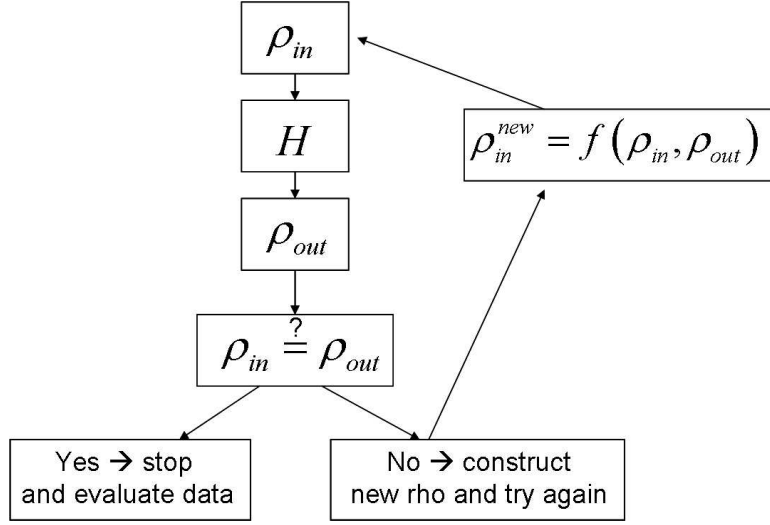


Figure 5.2: Schematic of the self-consistent cycle.

correlation potential for spin-dependent systems that we emphasize here is that the potential is also spin-dependent. In this sense it acts as an effective magnetic field.

5.6.2 Non-collinear spin

Here we consider the extension of the collinear spin-dependent exchange-correlation potential to noncollinear cases. In the most general case, a spin-dependent Hamiltonian is written as:

$$H\Psi = \begin{pmatrix} H_{\uparrow\uparrow} & H_{\uparrow\downarrow} \\ H_{\downarrow\uparrow} & H_{\downarrow\downarrow} \end{pmatrix} \Psi = E\Psi \quad (5.66)$$

Once the above is solved for the eigenfunctions, the spin dependent density matrix is determined as described earlier:

$$\rho = \begin{pmatrix} \rho_{\uparrow\uparrow} & \rho_{\uparrow\downarrow} \\ \rho_{\downarrow\uparrow} & \rho_{\downarrow\downarrow} \end{pmatrix} \quad (5.67)$$

From this the charge and spin density is determined, with the result:

$$n_{tot}(\mathbf{r}) = \text{Tr}[S\rho] \quad (5.68)$$

$$n_z(\mathbf{r}) = \text{Tr}[S(\rho_{\uparrow\uparrow} - \rho_{\downarrow\downarrow})] \quad (5.69)$$

$$n_x(\mathbf{r}) = 2\text{Re}\{\text{Tr}[S\rho_{\uparrow\downarrow}]\} \quad (5.70)$$

$$n_y(\mathbf{r}) = -2\text{Im}\{\text{Tr}[S\rho_{\uparrow\downarrow}]\} \quad (5.71)$$

The orientation of the spin is determined by $\mathbf{n} = (n_x\hat{x} + n_y\hat{y} + n_z\hat{z})/(n_x^2 + n_y^2 + n_z^2)^{1/2}$. $\mathbf{n}(\mathbf{r})$ determines $\theta(\mathbf{r}), \phi(\mathbf{r})$, which is the direction of the quantization axis for the local spin density. The magnitude of the polarization (or of the “up” component in the locally diagonal frame) is $(n_x^2 + n_y^2 + n_z^2)^{1/2} \equiv n_{\text{local}}^\uparrow$, while $n_{\text{local}}^\downarrow = n_{\text{tot}} - n_{\text{local}}^\uparrow$. The exchange-correlation potential is evaluated in the locally diagonal frame with $(n_{\text{local}}^\uparrow, n_{\text{local}}^\downarrow)$, determining $(V_{xc\uparrow}^{local}, V_{xc\downarrow}^{local})$. A rotation operator is applied to express this spin dependent potential in the global frame:

$$V_{xc}^{global} = U^\dagger V_{xc}^{local} U \quad (5.72)$$

where

$$U = \begin{pmatrix} \cos(\theta/2)e^{i\phi/2} & \sin(\theta/2)e^{-i\phi/2} \\ -\sin(\theta/2)e^{i\phi/2} & \cos(\theta/2)e^{-i\phi/2} \end{pmatrix} \quad (5.73)$$

The operator U rotates a spinor pointing in the (θ, ϕ) direction into the z direction. All angles are \mathbf{r} dependent. Eq. (5.72) can be written as

$$V_{xc}^{global} = \frac{1}{2}(V_{xc}^\uparrow + V_{xc}^\downarrow)\mathbf{1} + \frac{1}{2}(V_{xc}^\uparrow - V_{xc}^\downarrow) \begin{pmatrix} \cos(\theta) & \sin(\theta)e^{-i\phi} \\ \sin(\theta)e^{i\phi} & -\cos(\theta) \end{pmatrix} \quad (5.74)$$

In the above expression all of the V_{xc} are the values of V_{xc} in the locally diagonal frame. The above expression for V_{xc}^{global} makes the Hamiltonian dependent on all spin indices $(\uparrow, \uparrow), (\uparrow, \downarrow), (\downarrow, \uparrow), (\downarrow, \downarrow)$. Thus Eq. (5.74) defines a new Eq. (5.66), and the self-consistent cycle proceeds. The operations of finding the values of V_{xc}^{local} and rotating this to the global frame are performed at each point in real space.

Chapter 6

Spin Transfer

6.1 Introduction

In this chapter, we consider the dynamics of the magnetization of materials. We are ultimately interested in finding the instantaneous torques that are responsible for changing the magnetization configuration. These torques arise from many sources, and we shall consider how they can be calculated for realistic systems. We present a general approach which is valid for systems in equilibrium and for systems with an external applied voltage. Our approach utilizes NEGF+DFT, so that it captures the full electronic structure details of the materials involved.

In Sec. (6.2), we review the phenomenological description of magnetization dynamics for equilibrium systems (the Landau-Lifshitz equations). This serves as a general background and context for more in-depth considerations of the how magnetization dynamics are determined. In Sec. (6.3), we discuss the conventional picture of spin transfer. This is done with the idea of highlighting distinctions between this view and our own.

In Sec. (6.4), we discuss the derivation of magnetization dynamics from microscopics. From this well known procedure, we describe in Sec. (6.5) how param-

ters of a dynamical theory such as magnetic stiffness are usually calculated. Here we present our own general method for finding the magnetic stiffness parameters, which involves calculating the instantaneous torques present on the magnetization. The key feature of this method is that it may be applied to systems out of equilibrium. In Sec. (6.6), we discuss how the torques calculated for systems out of equilibrium (i.e spin transfer torques) relate to the conventional picture of spin transfer torques. Finally, we discuss in Sec. (6.7) the implementation of the calculation within our NEGF framework.

6.2 Spin dynamics: The Landau-Lifshitz equation.

The dynamics of magnetization are usually described in a phenomenological way with the Landau-Lifshitz equations. These describe the low-energy, long wavelength excitations of a ferromagnet from its ground state. The dynamics depend on the energy of a magnetic configuration $\mathbf{M}(\mathbf{r})$ is, which is often well described by:

$$E = E_{\text{exchange}} + E_{\text{anisotropy}} + E_{\text{demag}} + E_{\text{Zeeman}} ; \quad (6.1)$$

$$E_{\text{exchange}} = \frac{A}{M_s^2} \int d\mathbf{r} |\nabla \mathbf{M}|^2 ; \quad (6.2)$$

$$E_{\text{anisotropy}} = \frac{K}{M_s^2} \int d\mathbf{r} (\mathbf{M} \cdot \mathbf{c})^2 ; \quad (6.3)$$

$$E_{\text{demag}} = -\frac{1}{2} \int \mathbf{M} \cdot \mathbf{H} ; \quad (6.4)$$

$$E_{\text{Zeeman}} = -\mathbf{M} \cdot \mathbf{B}_{\text{app}} . \quad (6.5)$$

E_{exchange} is the energy cost associated with nonuniform magnetization configurations. It arises from interatomic exchange interactions, and is considered more fully later in this chapter. $E_{\text{anisotropy}}$ describes the energy associated with pointing in a certain direction in space. It comes fundamentally from spin-orbit interactions,

and is therefore much smaller than exchange energies in transition metals. E_{demag} is the magnetic dipole-dipole interaction energy, where \mathbf{H} is determined from the Maxwell's equation $\nabla \times \mathbf{H} = 0$. It is long range, and favors non-uniform magnetic configurations (it is the source of domain wall formation). Finally E_{Zeeman} is the Zeeman energy from an applied magnetic field. As a convention, \mathbf{M} is the magnetization per volume, so Eq. (6.1) represents an energy density, and $\mathbf{M} = M_s \boldsymbol{\Omega}$, where $\boldsymbol{\Omega}$ is the orientation of the magnetization.

If we define an effective field $\mathbf{B}_{\text{eff}} = -\delta E / \delta \mathbf{M}$, then the energy functional can be re-written

$$E = -\mathbf{M} \cdot \mathbf{B}_{\text{eff}}[\mathbf{M}] . \quad (6.6)$$

The magnetization \mathbf{M} is related to the angular momentum \mathbf{L} via the gyromagnetic ratio: $\mathbf{M} = \gamma \mathbf{L}$, The classical dynamics for \mathbf{M} (or \mathbf{L}) given an energy of the form Eq. (6.6) are [71]:

$$\frac{d\mathbf{M}}{dt} = \gamma \mathbf{M} \times \mathbf{B}_{\text{eff}} = \boldsymbol{\Gamma} , \quad (6.7)$$

where we denote the torque by $\boldsymbol{\Gamma}$.

In real systems, the magnetization is coupled to environmental degrees of freedom such as particle-hole excitations of the Fermi sea, phonons and nuclear spins (through spin-orbit and other interactions). Energy is dissipated from the magnetic system through these channels, and this is captured phenomenologically by the addition of a damping parameter α . The form of the damping often used is $(\alpha \boldsymbol{\Omega} \times \dot{\mathbf{M}})$, which ensures that $dE/dt \leq 0$. Inserting this by hand into the equation of motion yields the Landau-Lifshitz equations:

$$\frac{d\mathbf{M}}{dt} = \gamma \mathbf{M} \times \mathbf{B}_{\text{eff}} + \alpha \boldsymbol{\Omega} \times \frac{d\mathbf{M}}{dt} . \quad (6.8)$$

Fig. (6.1) indicates the trajectory for a uniform magnetization $\mathbf{\Omega}(t)$. (The case of spatially uniform magnetization is referred to in the magnetism literature as the “monodomain” case.) In this case, the applied field is in the $-\mathbf{z}$ direction, and the magnetization precesses around the applied field and eventually aligns with the applied field.

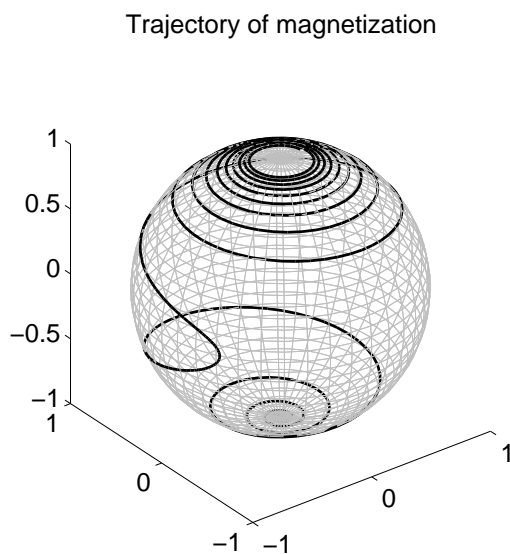


Figure 6.1: A typical trajectory of a monodomain switching event.

An important example of a metastable non-uniform magnetization configuration is a domain wall (DW). The magnetization profile of a particular simple model domain wall (a “Néel wall”) is described by the position-dependent orientation $(\theta(z), \phi(z))$:

$$\theta(z) = \pm \cos^{-1} \left(\tanh \left(\frac{z - z_0}{\lambda} \right) \right) ; \quad (6.9)$$

$$\phi(z) = 0 . \quad (6.10)$$

where the length scale is given by $\lambda = \sqrt{\frac{A}{K}}$, and the DW has an energy $\sqrt{4AK}$. Fig. (6.2) shows a schematic for a domain wall. We shall not discuss domain walls further in this work, but note here that the effect of spin transfer on domain wall dynamics is an important area of current research [72, 73, 74].

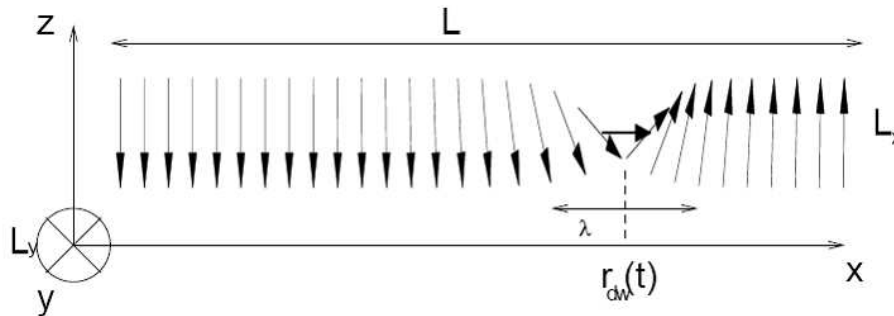


Figure 6.2: Cartoon of Néel Domain Wall.

6.3 Phenomenology of spin dynamics in the presence of current

We now consider the effect of spin currents on magnetization dynamics. In systems with noncollinear magnetic configurations, charge currents induce spin currents which exert a torque on the magnetization, referred to as the spin transfer torque (STT). These torques have been the subject of extensive theoretical work [24, 25, 75, 76, 9]. In this section we describe the physical picture and essential properties of the conventional picture of STT. Our purpose in describing the conventional picture of STT is that we want to ultimately highlight the differences between it and our picture of STT, and to show how the basic properties of STT change in antiferromagnetic (AFM) systems.

We disregard for the moment anisotropy and damping, and assume no external fields. The system is then rotationally invariant, and each component of the total spin angular momentum is conserved ($d\mathbf{M}_{\text{tot}}/dt = 0$). We then define a spin current \mathbf{Q} as the tensor product of Fermi sea drift velocity and spin: $\mathbf{Q} = \mathbf{v} \otimes \mathbf{M}$. The 2 indices (i, j) of Q_{ij} specify the direction of the current in real space and the direction of its spin polarization in spin space, respectively. Because spin angular momentum is conserved, we can write down an equation of continuity for \mathbf{M} :

$$\int dV \left[\frac{\partial \mathbf{M}}{\partial t} + \nabla \cdot \mathbf{Q} \right] = 0 . \quad (6.11)$$

If we denote \mathbf{M}_V as the magnetization inside a volume dV , the divergence theorem yields:

$$\frac{\partial \mathbf{M}_V}{\partial t} = - \int \mathbf{Q} \cdot d\mathbf{A} . \quad (6.12)$$

Physically, this represents conservation of \mathbf{M} : the magnetization can change only if magnetization leaves or enters the volume - it can not just appear or disappear out of nowhere.

This physics is completely analogous to the more familiar particle continuity equation. In terms of particle number n , and particle current $\mathbf{j} = \mathbf{v}n$:

$$\frac{\partial \rho}{\partial t} + \nabla \cdot \mathbf{j} = 0 . \quad (6.13)$$

This is also a reflection of a conservation law (conservation of particle number) which is derived from $U(1)$ symmetry.

When there is anisotropy or an applied field, rotational symmetry is broken resulting in non-conservation of \mathbf{M}_{tot} . In this case \mathbf{M} changes in time according to the Landau Lifshitz equation (Eq. (6.7)). However we still retain the contribution

to $d\mathbf{M}_V/dt$ from the divergence of the spin current:

$$\frac{\partial \mathbf{M}_V}{\partial t} = \mathbf{\Gamma} - \int \mathbf{Q} \cdot d\mathbf{A} \quad (6.14)$$

$$\Rightarrow \frac{\partial \mathbf{M}_V}{\partial t} = -\gamma \mathbf{M}_V \times \frac{\partial E}{\partial \mathbf{M}} + \alpha \mathbf{\Omega} \times \frac{\partial \mathbf{M}_V}{\partial t} + (\mathbf{Q}_{in} - \mathbf{Q}_{out}) . \quad (6.15)$$

The evaluation of the spin transfer torque (the last term of Eq. (6.15)) therefore boils down to evaluating spin current fluxes. If we write the spin current density as pJ , where J is the charge current density, and p is the polarization, and divide both sides of Eq. (6.15) by $\mathbf{M}_V = M_s dV$, we obtain:

$$\Rightarrow \frac{\partial \mathbf{\Omega}}{\partial t} = -\gamma \mathbf{\Omega} \times \frac{\partial E}{\partial \mathbf{M}} + \alpha \mathbf{\Omega} \times \frac{\partial \mathbf{\Omega}}{\partial t} + \frac{pJ}{M_s \ell} (\hat{\mathbf{Q}}_{in} - \hat{\mathbf{Q}}_{out}) . \quad (6.16)$$

This form of the equation for $d\mathbf{\Omega}/dt$ demonstrates a number of important general properties about the STT term applied to a ferromagnetic nanoparticle : its magnitude is proportional to the current density, and inversely proportional to the length (along the charge current direction). Hence the is maximized for thin FM layers.

6.3.1 Spin torques and spin fluxes in FM

To get an idea for the basic properties of STT in FM, it suffices to consider a toy model of spin-dependent transport. We suppose an electron with spin in the \hat{x} direction is incident upon a ferromagnet with magnetization in the \hat{z} direction (see Fig. (6.3)).

The incoming spinor $|\hat{x}\rangle$ can be written $(|\uparrow\rangle + |\downarrow\rangle)/\sqrt{2}$. As discussed in Sec. (5.6), the exchange-correlation potential differs for up and down spins in a ferromagnet. The wave function therefore has the following form:

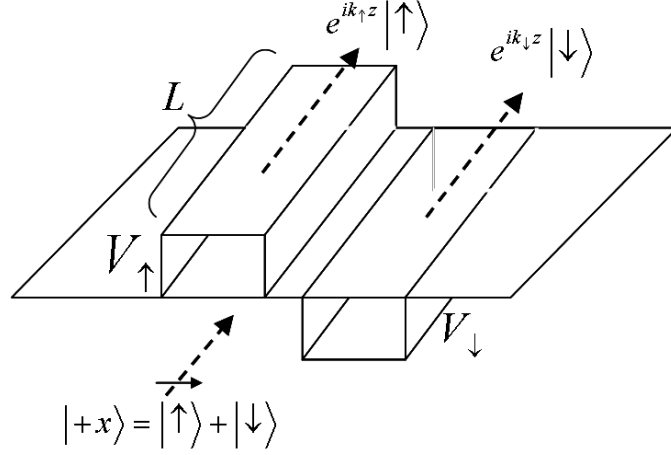


Figure 6.3: Schematic for scattering problem of \hat{x} spinor incident on a ferromagnet with orientation in \hat{z} -direction.

$$\psi(z) = \begin{cases} T_{\uparrow} e^{ik_{\uparrow}z} |\uparrow\rangle + T_{\downarrow} e^{ik_{\downarrow}z} |\downarrow\rangle & \text{for } z > 0 \\ (e^{ikz} + R_{\uparrow} e^{-ikz}) |\uparrow\rangle + (e^{ikz} + R_{\downarrow} e^{-ikz}) |\downarrow\rangle & \text{for } z < 0 \end{cases} \quad (6.17)$$

Where $E = k_{\uparrow,\downarrow}^2 \pm \Delta/2 = k^2$. To find the STT, we evaluate the spin current fluxes of this scattering state into and out of the FM. Fig. (6.4) shows the spin density of a single scattering state: the spin transverse to \hat{z} simply precesses around the magnetization, (with precession period $= (k_{\uparrow} - k_{\downarrow})^{-1}$). The precession period will vary for different scattering states at the Fermi energy (because different states will have different values of $(k_{F\uparrow} - k_{F\downarrow})^{-1}$). When the spin is averaged over all states at the Fermi energy, these oscillating spin densities destructively interfere, and the component of the spin perpendicular to the magnetization decays, as shown in Fig. (6.4). More explicitly, if the angle between incoming spin current and magnetization

is θ , the fluxes are:

$$\mathbf{Q}_{\text{in}} = gI (\sin(\theta)\hat{x} + \cos(\theta)\hat{z}) \quad (6.18)$$

$$\mathbf{Q}_{\text{out}} = gI \cos(\theta)\hat{z} \quad (6.19)$$

$$\Rightarrow \mathbf{Q}_{\text{out}} - \mathbf{Q}_{\text{in}} = gI \sin(\theta)\hat{x} \quad (6.20)$$

The net spin current flux (or STT) is then given by the component of the incoming spin current that is perpendicular to the magnetization. This brief analysis we have summarized neglects some details such as the spin direction of the reflected part of the wave function. It does however provide a qualitatively correct view of the conventional picture of STT.

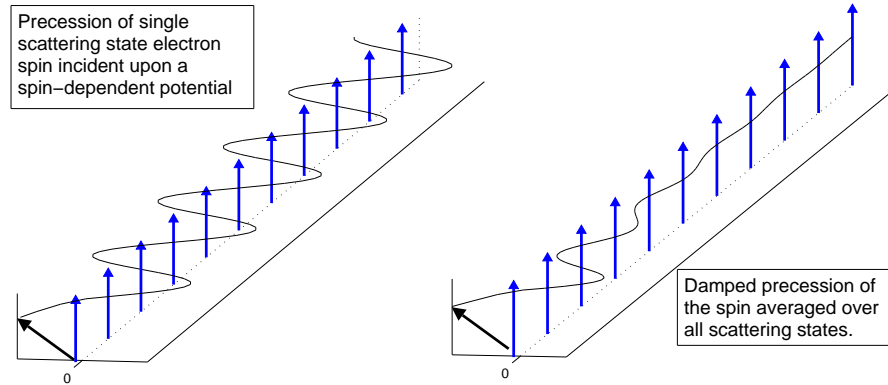


Figure 6.4: Current carrying electron spin. On the left it precesses around the magnetization. The right figure shows the total spin after averaging over all current carrying states. In this case the transverse component decays to 0.

Given this outline of the physics behind the STT, we copy the cartoon of STT given in Ch. 1 to consider once again:

The preceding analysis explains how the interference over transverse chan-

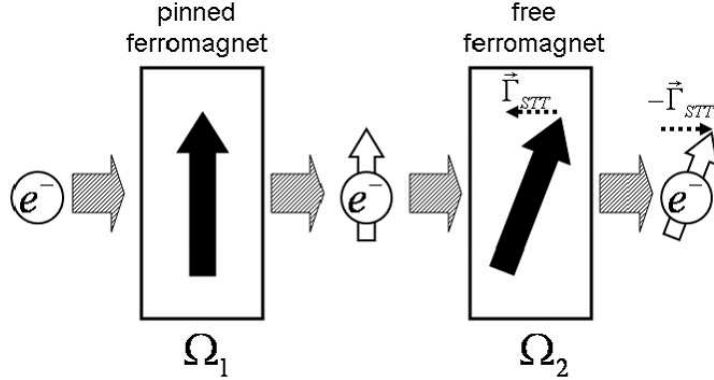


Figure 6.5: Cartoon showing spin transfer torque. The electron spin enters the free ferromagnet point up, and is rotated by the magnetization so that it leaves in a different direction. Spin transfer is the back-action torque on the magnetization by the electron spin.

neels' spin densities results in a spin current that is always aligned with local magnetization. By virtue of conservation of spin angular momentum, the resulting net spin current flux necessarily causes the magnetization to change in time. These general arguments lead to a spin transfer torque of the form:

$$\Gamma_{\text{STT}} = \frac{g(\theta)}{M_s \ell} J \sin(\theta) . \quad (6.21)$$

where the factor of $\sin(\theta)$ picks out the transverse portion of the incoming spin density, g represents the amount of spin torque delivered per transmitted electron, and ℓ is the length of the ferromagnet along the current direction.

The efficiency g is a very important parameter for potential applications of STT (as described in Sec. (7.3)). For MRAM applications, one would like to maximize g in order to flip the magnetization (or perform a write operation) with a small applied current, while for CPP read heads, it is desirable to minimize g so

that the magnetic orientation is a sensor of magnetic bits only, and not subject to noise from STT.

We highlight these well known features of spin transfer physics because they are qualitatively different in the context of anti-ferromagnets, as we shall see in later chapters. We also note that the analysis given here does not identify the microscopic interaction that is responsible spin transfer torque - it merely infers its existence by invoking a conservation law.

6.3.2 Current induced magnetization switching

A major experimental implication for spin transfer torque is current induced magnetization switching (CIMS). The standard spin valve experimental geometry is shown in Fig. (6.6). Normally a sufficiently large magnetic field ensure that both free and fixed magnetic layers are aligned with it. Any deviation from alignment, from thermal fluctuations for example, is quickly extinguished because of the damping, as described in Sec. (6.2). However in the system shown below, the spin transfer torque Γ_{STT} opposes the damping. If the current density is sufficiently large, the magnetization of the free layer switches to be anti-aligned with the field. The criterion for the switching in this simple case is:

$$\Gamma_{\text{STT}} > \alpha B_{\text{app}} . \tag{6.22}$$

The properties of spin transfer torques are generally studied by measuring switching current versus applied field.

6.4 Microscopic theory of spin dynamics

In the previous section, the dynamics of magnetization was derived in a phenomenological fashion, using a Landau energy functional and classical equations of motion.

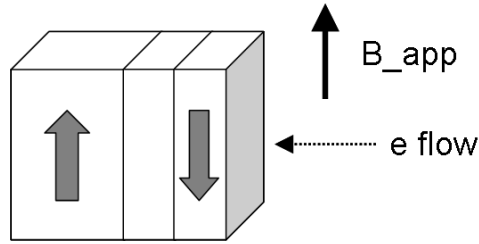


Figure 6.6: Illustration of current induced magnetization switching. The orientation of the free (thinner) FM layer is opposed to the applied field because of spin transfer torque.

We now consider how the magnetization dynamics can be described starting from a microscopic Hamiltonian. We are especially interested in the magnetization dynamics when there is a current in the system. As a matter of terminology, we refer to a system under a finite external bias as “nonequilibrium”. We consider also the dynamics of systems with no external bias - these systems will be referred to as “equilibrium”. Both “equilibrium” and “nonequilibrium” systems we consider are “non-stationary” - that is, they are time-dependent. We will not explicitly integrate the dynamics in time, instead we will be content with finding the instantaneous value of $d\mathbf{m}(t)/dt$, from which the dynamics can be easily obtained. As a matter of language, the phrase “determining dynamics” is used interchangeably with “determining $d\mathbf{m}(t)/dt$ ”.

In this section, we first give an indication of how a Landau-Lifshitz type equation can be obtained microscopically. We use the resulting expressions to find equilibrium dynamics - specifically the magnetic stiffness parameters of ferromagnetic materials (the parameter A of Eq. (6.2)). We cover these topics briefly, as they have been studied in detail previously. We then show how dynamics can also be obtained from the instantaneous torques present in non self-consistent systems. We calculate these torques to again find stiffness parameters for equilibrium systems,

verifying the consistency between the two approaches. We also calculate the torques in nonequilibrium systems (the spin transfer torques), and indicate the relation of this method to the standard picture of spin torques described in Sec. (6.3).

6.4.1 Adiabatic approximation

The starting point for all treatments of spin dynamics in solids is the separation of time scales for (fast) scalar electron fields and (slow) collective magnetic excitations. This separation of time scales follows from the separation of energy between the interatomic exchange energy (< 100 meV), which determines spin wave dispersions, and characteristic electronic energies such as bandwidth and intraatomic exchange [77], which are typically much larger.

Because of relatively slow magnetic dynamics, the electrons respond “instantly” to the instantaneous magnetic configuration - from the electrons’ perspective, the spin configuration is essentially static (note it is the *direction* which changes slowly, the *magnitude* of the magnetization changes on electronic time scales). The situation is analogous to the separation of time scales between the motion of ions in the lattice and the electronic degrees of freedom. (In this case, the adiabatic approximation is referred to as the Born-Oppenheimer (B-O) approximation.) The B-O approximation results in an equation of motion (EOM) for the ions. Our interest is in how the adiabatic approximation leads to an equation of motion for the magnetization.

There are a number of routes to deriving spin dynamics from an adiabatic approximation [78, 79, 77]. Here we briefly describe the general course taken by Niu and Kleinman [80, 81]. In their treatment, space is partitioned into cells of volume V_i , and \mathbf{m}_i is the spin inside the i^{th} volume. The key point in their derivation is the fact that the electronic wave function remains in the instantaneous ground state as the spin configuration evolves. (This fact is simply a statement of the adiabatic

theorem.) This constraint leads to the equation of motion for the spin variable \mathbf{m}_i :

$$-\sum_{j,\beta} \Omega_{ij}^{\alpha\beta} \dot{m}_j^\beta + \frac{\partial E}{\partial m_i^\alpha} = 0 , \quad (6.23)$$

where $E = \langle \psi | H | \psi \rangle$, and Ω is the Berry curvature, given as:

$$\Omega_{ij}^{\alpha\beta} = \frac{\partial}{\partial m_i^\alpha} \langle \psi | \frac{i\partial}{\partial m_j^\beta} | \psi \rangle - \frac{\partial}{\partial m_j^\beta} \langle \psi | \frac{i\partial}{\partial m_i^\alpha} | \psi \rangle . \quad (6.24)$$

In this work we make the simplifying assumption that the spin on a given atomic site is uniform in direction, or rigid (referred to in other work as the “rigid spin approximation” or RSA [77]). This approximation is valid under the condition that it is possible to identify well-defined regions of space in which the spin density is approximately constant. This condition is satisfied for strong ferromagnets such as Fe, however is not as well satisfied for weaker itinerant ferromagnets. Within this approximation, the Berry curvature is simply given as

$$\Omega_{ij}^{\alpha\beta} = \delta_{ij} \epsilon^{\alpha\beta\gamma} m_i^\gamma / (m_i)^2 . \quad (6.25)$$

This expression for the Berry curvature leads to a Landau-Lifshitz type equation for the spin \mathbf{m}_i :

$$\dot{\mathbf{m}}_i = -\mathbf{m}_i \times \frac{\partial E}{\partial \mathbf{m}_i} . \quad (6.26)$$

Thus reproducing Eq. (6.7). Eq. (6.26) describes only the dynamics of the *direction* of the magnetization - as described earlier, the magnitude of the magnetization is not an adiabatic variable. This EOM for spin is similar in format to the Born-Oppenheimer approximation for ionic dynamics: the spin dynamics depend on the variation of electronic energy with spin variable (whereas in the Born-Oppenheimer approximation, the ionic motion $\dot{\mathbf{R}}$ depends on $E[\mathbf{R}]$). Therefore the task for cal-

culating spin dynamics simply boils down to computing $E[\mathbf{m}]$. In the next section we describe how this is accomplished.

6.5 Equilibrium dynamics - stiffness calculation

We first consider an equilibrium, non-stationary magnetic system. The calculation of how the energy depends on \mathbf{m} is simplified by the magnetic force theorem. Normally in DFT, the energy is given by Eq (5.22), which includes both self-consistent single particle energies and double counting corrections terms. The magnetic force theorem says that to find the energy difference between the ground state and a slightly perturbed state, we only need to find the non-self-consistent change in single particle energies. (The proof can be found in Ref. [82]; the idea is that induced changes in the self-consistent part of the potential are approximately cancelled by changes in the double counting energy terms.)

As an example, we consider a uniform bulk magnetization. We would like to find the energy cost associated with rotating a single layer's orientation Ω_0 by an angle θ ; that is, we would like to calculate $E[\theta]$.

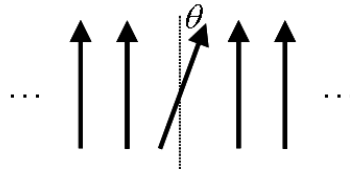


Figure 6.7: Tilting one atomic plane by θ of a uniform, infinite, bulk system.

Since the uniform magnetic state represents an energy extremum, we can parameterize the energy of small rotations away from the collinear ground state

generally as:

$$E[\mathbf{\Omega}_0] = J\mathbf{\Omega}_0 \cdot \mathbf{z} = J \cos \theta \quad (6.27)$$

In writing the energy in this fashion, we describe an itinerant magnetic system in a Heisenberg form. We can extract an effective Heisenberg coupling constant between the rotated plane and the rest of the system by finding:

$$J = \frac{E_{sp}[\theta_1] - E_{sp}[0]}{\cos(\theta_1) - 1} \quad (6.28)$$

Here E_{sp} refers to the non self-consistent single particle energy, which is all that we need to consider by virtue of the magnetic force theorem.

Lichtenstein et al. [83] derive an expression for J by expanding $E_{sp}[\theta]$ to second order in θ . (They consider the coupling between a single atom (labelled “0”) and the rest of the lattice, as opposed to a plane and the rest of the lattice.) The result is:

$$J = -\frac{1}{4\pi} \int^{E_f} \text{ImTr} [\Delta_0 (G_{\downarrow}^{00} - G_{\uparrow}^{00}) + \Delta_0 G_{\uparrow}^{00} \Delta_0 G_{\downarrow}^{00}] dE \quad (6.29)$$

The trace in the above is over orbitals of the atom, G_{σ}^{00} is the Green’s function of atom 0 for the original collinear ground state, and Δ_0 is the spin splitting Hamiltonian on atom 0. Similarly, the pairwise interaction between atoms i and j is given as

$$J_{ij} = -\frac{1}{4\pi} \int^{E_f} \text{ImTr} [\Delta_i G_{\uparrow}^{ij} \Delta_j G_{\downarrow}^{ji}] dE \quad (6.30)$$

Here G_{σ}^{ij} is the Green’s function coupling atom i to j (off-diagonal in atom index) for the original collinear ground state. Pajda et. al [84] determined the pairwise Heisenberg parameters for bulk Fe, Co, and Ni out to the 10th nearest neighbor.

From their data we are able to determine the Heisenberg coupling between a single atomic plane and the rest of the lattice. We use Eq. (6.29) to calculate the stiffness parameters, and our results are shown in comparison to Pajda et. al in the table 6.5.1.

6.5.1 Torque method for stiffness

We next consider an alternative expression for the stiffness. Our interest is to find an expression which does not rely on $E[\mathbf{m}]$, a quantity which may not yield torques in nonequilibrium systems (this point is discussed more below).

To derive expressions for magnetization dynamics, we separate both the single-particle Hamiltonian and the density matrix into spin-dependent and spin-independent contributions:

$$\mathbf{H}_{ij} = \mathbf{H}_{ij}^0 - \frac{1}{2} \mathbf{\Delta}_{ij} \cdot \boldsymbol{\tau} . \quad (6.31)$$

$$\rho_{ij} = \frac{1}{2} [\rho_{ij}^0 + \mathbf{m}_{ij} \cdot \boldsymbol{\tau}] . \quad (6.32)$$

where $\boldsymbol{\tau}$ is the vector of Pauli spin matrices and i, j are orbital indices. The notation for the spin-dependent part of the Hamiltonian is chosen to emphasize that it produces a spin-splitting Δ when it is orbital independent, as often assumed in simple toy models of a ferromagnetic metal (note that \mathbf{m} and $\mathbf{\Delta}$ are in general complex for orbital off-diagonal elements $i \neq j$). In mean field approximations, the interaction contribution to $\mathbf{\Delta}$ and \mathbf{m} are related locally in real space according to

$$\mathbf{\Delta}(\mathbf{r}) = \Delta_0(n(\mathbf{r}), m(\mathbf{r})) \hat{\mathbf{m}}(\mathbf{r}) . \quad (6.33)$$

where n and m are the local charge and spin densities, respectively, $\hat{\mathbf{m}} = \mathbf{m}/m$ is the space-dependent orientation of the magnetization, and Δ_0 is some parameterization of the exchange-correlation potential (given in detail in Appendix A). (Note in

Eq. (6.33), $\mathbf{\Delta}(\mathbf{r})$ and $\mathbf{m}(\mathbf{r})$ are functions in real space, while in Eq. (B.12), $\mathbf{\Delta}_{i,i'}$ represents the i, i' matrix element of the realspace potential $\mathbf{\Delta}(\tilde{\mathbf{r}})$, and $\mathbf{m}_{i,i'}$ the density matrix in orbital space).

To consider non-stationary states, we explicitly decouple the mean-field spin-dependent potential from the spin-dependent density matrix. That is, we allow for non-self-consistent $[H, \rho]$ pairs. In this case, we let $\mathbf{\Delta} = \Delta_0(n, m)\hat{\mathbf{m}}$, and $\rho = \frac{1}{2}[\rho^0 + \mathbf{s} \cdot \boldsymbol{\tau}]$, where $\hat{\mathbf{s}}$ is no longer in general parallel to $\hat{\mathbf{m}}$. A non-self-consistent $[H, \rho]$ pair attains its meaning via the magnetic force theorem (where non-self-consistent single particle energies are approximately equal to self-consistent total energies under small perturbations). The single particle energy of such a pair is then:

$$E_{\text{sp}} = \frac{1}{2} \text{Tr} \left[H_0 \rho_0 - \frac{1}{2} \Delta_0 \hat{\mathbf{m}} \cdot \hat{\mathbf{s}} \right]. \quad (6.34)$$

The dynamics associated with this $[H, \rho]$ pair is given generally by Eq. (6.26) ($= \mathbf{m} \times \partial E / \partial \mathbf{m}$). With the explicit form of the energy given here, we find that $d\mathbf{m}/dt$ is given by $\Delta_0(\hat{\mathbf{m}} \times \hat{\mathbf{s}})$. Physically, this quantity represents the torque on \mathbf{m} by the instantaneous spin density \mathbf{s} . The preceding analysis is not rigorous, but merely shown for the purposes of demonstrating the general relationship between changes in energy and $(\mathbf{m} \times \mathbf{s})$ - what we call “instantaneous torques”. A rigorous demonstration of the equivalence of the two approaches is given in Appendix B.

The scheme to calculate stiffness parameters from torques is therefore as follows: we take a self-consistent, collinear magnetic configuration and distort it in some way - as before we rotate the spin orientation of 1 atomic layer. This results in a new Hamiltonian with a modified spin dependent $\mathbf{\Delta}'$. We solve for the resulting non self-consistent spin density \mathbf{s} . The torque is given by (including the k index

from transverse periodicity):

$$\mathbf{\Gamma} = \frac{1}{2} \int dk \text{Tr}[\mathbf{\Delta}'_k \times \mathbf{s}_k] . \quad (6.35)$$

If we assume the energy is of simple Heisenberg form (Eq. (6.27)), then the torque is related to the magnetic stiffness via

$$\mathbf{\Gamma} = J \sin(\theta) . \quad (6.36)$$

For equilibrium systems, the torque is purely out of plane (\hat{y} -direction), so we can extract the stiffness:

$$J = \frac{\Gamma_y(\theta)}{\sin(\theta)} . \quad (6.37)$$

Table (6.5.1) shows the results from our calculation compared to previously published results. The agreement is good, with the exception that our result for Ni is too high. These stiffness parameters relate to measurable quantities, namely the spin wave dispersion for long wavelength spin waves, and the critical temperature. Table (6.5.1) gives the relation between previously published works and these parameters. Again the agreement is fairly good, with the exception of Ni. Ni may be less accurately calculated because it is a weak ferromagnet, and the conditions of RSA may be less well satisfied. It should be noted that calculated stiffness parameters are heavily dependent on basis set properties. Here we use a double- ζ with polarization basis set, and have optimized the basis set parameters with respect to ground state energy using a simplex minimization routine [66] (see Sec. (5.4) for a description basis orbital parameters).

Metal	J from Pajda [84] (mRyd)	our calculated $\partial E/\partial \Omega$ ($\mathbf{m} \times \mathbf{s}$)	T_c (Pajda)	T_c (expt)
Co	10.948	11.822 (11.753)	1645	1388-1398
Fe	9.882	9.562 (9.362)	1414	1044-1045
Ni	2.530	3.954 (4.041)	397	624-631

Table 6.1: Stiffness parameters for Co, Fe, and Ni - as calculated by Pajda et al. [84], and our calculations using their method, and the torque method. Also shown is the calculated and experimental T_c from the data of Pajda et al.

6.6 Nonequilibrium dynamics - STT calculation

From an operational point of view, the distinction between torque and energy methods for calculating equilibrium stiffness parameters is not significant. However the notion of torques arising from instantaneous spin densities has definite physical significance, and is central to finding the torques that exist in systems under bias. We discuss this important point more below.

The torque method of calculating stiffness offers insight into the physical mechanism that drives magnetization dynamics. Specifically, in a non-stationary state, there is a mis-alignment between the (slow) magnetization and the (fast) electron spins. The electron spins therefore make a contribution to the exchange-correlation effective magnetic field that is misaligned with the magnetization. The magnetization dynamics is then due to the precession of the magnetization around this misaligned exchange field. This mechanism behind magnetization dynamics is general, and we posit that it holds in nonequilibrium situations as well. We do not have a rigorous proof of this claim, however in the next section it is placed on firm ground for ferromagnets, or in general for any system in which spin conserved. In systems with strong spin-orbit coupling, the validity of this picture is not as clear,

although it has been employed by several researchers [85] in the context of spin torques in magnetic semiconductors. We return to this point in the last chapter.

An additional, and perhaps more practical motivation for describing dynamics in terms of torques rather than energies is that in nonequilibrium systems, energy may no longer determine system dynamics. To rephrase the point, it is not clear whether or not current induced torques (or forces) are conservative - that is, whether these torques (forces) can be written as the variation of an energy functional [86, 87]. This is a controversial issue, and as yet unresolved. So far most work has addressed forces on ionic degrees of freedom in nonequilibrium systems. Even in these systems the question is still open. For magnetic systems, energy functionals that yield the proper torques for nonequilibrium states involve vector potentials of magnetic monopoles [75], so it seems unlikely that the simple $K - S$ band energy is able to yield a nonequilibrium torque. We will defer further discussion of this important point to the last chapter.

6.6.1 Nonequilibrium torques and spin current fluxes

The picture of spin transfer torques as arising from the interaction between the magnetization and the misaligned exchange field of the quasiparticles is consistent with the conventional view of spin transfer as described in Sec. (6.3). Recall that in the conventional picture, spin torques are a necessity for satisfying conservation of total spin angular momentum. The spin transfer torques are then expressed in terms of the net spin current flux into/out of a volume.

The relation between spin flux and local torques can be found by considering the time-dependence of the the α -th component of the spin-density \mathbf{S} of a chosen

subsystem (SS) (see Appendix B for a derivation):

$$\begin{aligned} \dot{S}^\alpha = \sum_{i \in SS} \sigma_i^\alpha (\partial_t \rho) &= \sum_{\substack{i \in SS \\ j \notin SS}} \left[\frac{i}{2i\hbar} [\mathbf{H}_{ij}^{(0)} s_{ji}^\alpha - s_{ij}^\alpha \mathbf{H}_{ji}^{(0)} + \Delta_{ij}^\alpha \rho_{ji}^{(0)} - \rho_{ij}^{(0)} \Delta_{ji}^\alpha] \right. \\ &\quad \left. + \sum_{i,j \in SS} \frac{1}{4} \epsilon_{\alpha,\beta,\gamma} [\Delta_{ij}^\beta s_{ji}^\gamma + s_{ij}^\gamma \Delta_{ji}^\beta] \right]. \end{aligned} \quad (6.38)$$

The first four terms on the right hand side of Eq. (6.38) represent the net spin-current into the subsystem which has contributions from both the spin-polarization of inter-orbital coherence \mathbf{m} and from the spin-dependence of the inter-orbital matrix elements $\mathbf{\Delta}$ in the Hamiltonian. The final term describes the precessional time-evolution of spins in the subsystem under the influence of effective magnetic fields implied by the spin-dependent terms in the Hamiltonian. Eq. (6.38) can be written in a more suggestive form which is relevant for the multilayer geometries considered in this work.

$$\dot{\mathbf{M}} = (\mathbf{Q}_{(i_L-1, i_L)} - \mathbf{Q}_{(i_R, i_R+1)}) + \text{Tr}_{SS}[\mathbf{s} \times \mathbf{\Delta}] \quad (6.39)$$

Where the trace in the second term is over orbitals in the subsystem. The spin-current operator $\mathbf{Q}_{i,i+1}$ is defined as the spin current that flows between sites i and $i+1$. It is given by

$$\mathbf{Q}_{i,i+1} = \sigma \sum_{\substack{k \leq i \\ j > i}} \text{Im}[H_{kj} \rho_{jk}] \approx \frac{1}{2} \sum_{\substack{k \leq i \\ j > i}} \text{Im}[H_{kj}^{(0)} \mathbf{s}_{jk}] \quad (6.40)$$

In the second part of Eq. (6.40), we make the simplifying assumption that the ‘‘hopping’’ is spin-independent, which is very nearly true in the systems we have considered. (The presence of spin-dependent hopping presents slight complications that are explained more fully in Appendix (B)). Fig. (6.8) illustrates Eq. (6.39) -

the indices i_L and i_R represent the atomic planes at the edge of the subsystem, so that $\mathbf{Q}_{(i_L-1, i_L)}$ is the spin flux entering the subsystem from the left, and $\mathbf{Q}_{(i_R, i_R+1)}$ the spin current leaving through the right:

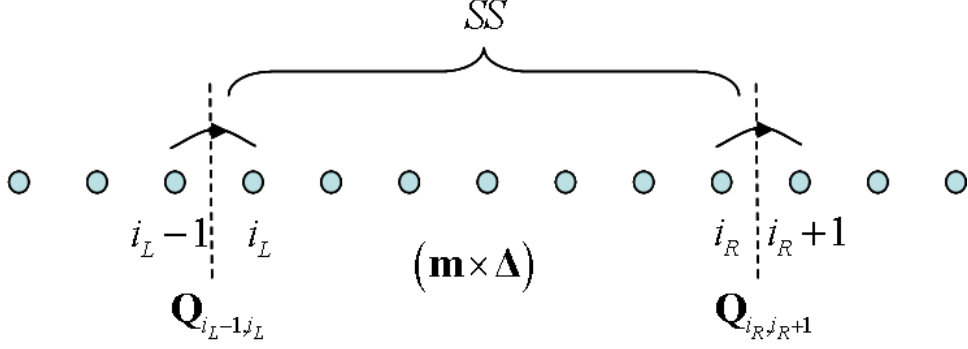


Figure 6.8: Illustration of Eq. (6.39), relating spin current fluxes to local spin precession.

We can now easily make the connection between local torques and spin currents. With the adiabatic approximation, the transport electrons satisfy a time-independent Schrödinger equation for the given magnetization configuration. In this case, $\dot{\mathbf{S}} = 0$, so that, according to Eq. (6.39):

$$(\mathbf{Q}_{(i_L-1, i_L)} - \mathbf{Q}_{(i_R, i_R+1)}) = -\text{Tr}_{SS}[\mathbf{s} \times \Delta] \quad (6.41)$$

The meaning of Eq. (6.41) is that the net spin current flux into/out of the subsystem is equal to the local precession of the spin around the exchange field in the subsystem. In Eq. (6.41), the l.h.s is the quantity conventionally associated with spin transfer torque, while the r.h.s. is the local torque - the same quantity related to magnetic stiffness for equilibrium systems. Therefore the local torque present in a non-self-consistent $[H, \rho]$ pair under bias is precisely the spin transfer torque found from evaluating spin current fluxes.

The matrix product $\mathbf{m} \times \mathbf{\Delta}$ can be decomposed on an orbital by orbital basis to reveal which orbital pairs contribute most to the torque. For example, the torque exerted by transport s electrons on the d electrons contribution to $\mathbf{\Delta}$ is

$$\mathbf{\Gamma}_{sd} = \mathbf{s}_s \times \mathbf{\Delta}_d \quad (6.42)$$

This is useful for seeing how well common toy models of spin transport (for example the $s - d$ model) represent more realistic calculations.

Finally, in the case where spin is not conserved (for example, for systems with strong spin-orbit coupling), the conservation argument that implies the torques are equal to net spin flux no longer apply. We can nevertheless evaluate spin transfer torques from the microscopic local torques. (It should be noted that stiffness parameters for equilibrium systems with strong spin orbit coupling can be calculated accurately with the energy or torque method [88].)

6.7 Implementation

It is straightforward to implement the calculations of spin transfer torque. To verify the consistency of our approach, we have evaluated the spin current operator (given by Eq. (6.40)) and the local torques in order to check that Eq. (6.41) is satisfied. As an illustration, Fig. (6.9) shows the spin current and local spin torque for a Co-Cu-Co trilayer spin valve structure. (This system is considered in detail in Ch. (7). The following data satisfy Eq. (6.41). The decay of spin transfer torques away from the Co-Cu interface as described in Sec. (6.3) is evident.

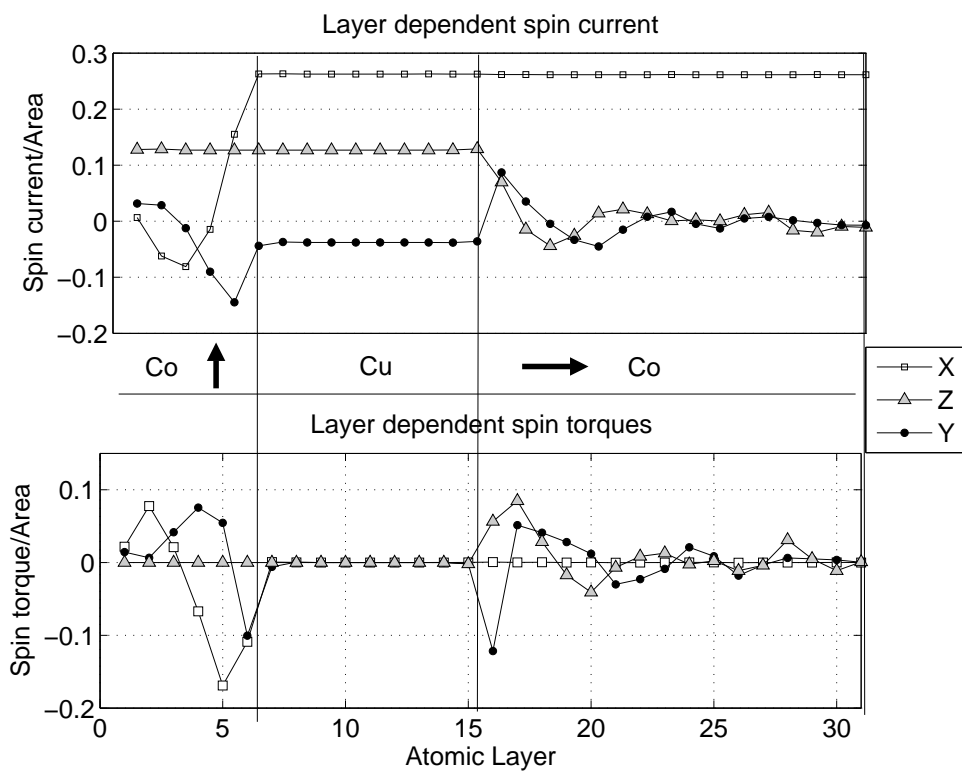


Figure 6.9: Spin current and spin fluxes in Co-Cu-Co-Cu system, with $\theta = 90^\circ$.

Chapter 7

Spin Torques in Ferromagnetic Metal structures

The contents of this chapter are partially based on the article:

P. M. Haney, D. Waldron, R. A. Duine, A. S. Núñez, H. Guo, and A. H. MacDonald, *Current-induced order parameter dynamics: Microscopic theory applied to Co/Cu/Co spin valves*, Phys. Rev. B, **76**, 024404 (2007).

7.1 Introduction

The spin valve structure composed of Co ferromagnetic layers and Cu nonmagnetic layers is a classic system for studying magnetoresistance and spin transfer effects experimentally [28, 29]. There are many theoretical treatments of this system as well [42, 89, 44], and we consider it in some detail here as a benchmark case. The two fundamental spintronic quantities a transport theory predicts are the magnetoresistance and the spin torque efficiency factor g . We calculate these quantities for a number of Co-Cu stack configurations. We also make a comparison to the results of a diffusive calculation for the same system. The aim of this chapter is both to

study properties of Co-Cu systems and, since these systems are well understood, to also understand properties of the calculations method itself.

This chapter is organized as follows: We describe technical details of our calculation and properties of bulk Co and Cu in Sec. (7.2). In Sec. (7.3), we consider how the electronic structure influences transport and STT in a [Co lead - Cu - Co lead] spin valve. In Sec. (7.4), we highlight important features of our calculation method by contrasting our results in the ballistic regime with the corresponding diffusive limit of the same system. Next we consider how calculated quantities change with the number of interfaces included; specifically, in Sec. (7.5) we compare the MR and spin transfer for a [Co lead - Cu - Co lead] trilayer (2-interface) and for a [Co lead - Cu - Co - Cu lead] (3-interface) system. Finally, in Sec. (7.6) we consider the so-called Dual Spin Filter design of [Co lead - Cu - Co - Cu - Co lead], to study a possible scheme for increasing the spin transfer efficiency.

7.2 Calculation details

In all of the various calculations of Co-Cu structures described below, we take Co and Cu to have *fcc* crystal structure, with lattice constant $a = 3.54 \text{ \AA}$. The fcc phase of Co is stabilized by stacking on the (001) substrate of Cu [90, 91]. The interface between materials is taken to be perpendicular to the [100] direction. We use norm-conserving pseudopotentials and an *s, p, d* single-zeta basis set, as described in Ch. (5). We have found excellent agreement with established band structure, density of states, and bulk conductance for Co and Cu with this basis set (see Fig. (7.1) for density of states data). For calculations on of Co-Cu layered structures, we have found that 800 *k*-points within the Brillouin zone is sufficient for convergence of the self-consistent density matrix. To calculate transmission coefficients and nonequilibrium spin densities, we have used 25,600 *k*-points. We have found that there is less than a 1 % difference in these quantities when using up to 32,400

k -points.

To get an idea of the role that electronic structure plays in the transport, we first consider the electronic properties of bulk Co and Cu separately. The Fermi surface of majority channel Co and Cu are both nearly spherical (see Fig. (2.4)). The similarity can be traced back to the fact that both materials have approximately 5.5 electrons in the majority valence shell, and in this case identical lattice structures. The Co minority channel Fermi surface is quite complex, possessing multiple sheets of complicated shape. The bulk conductance shown in Table (7.1) indicates that the minority channel has more than twice as many states at the Fermi energy. This large density of states at the Fermi level of the minority channel is the underlying reason for the ferromagnetic state of Co in the first place.

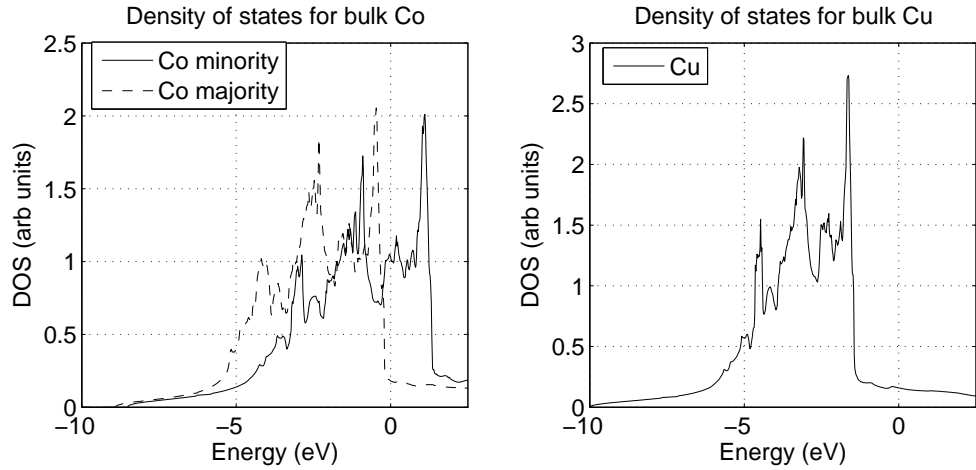


Figure 7.1: Density of states for Co and Cu.

Table (7.1) shows the spin resolved conductance and polarization for bulk Co and Cu, and a single Co-Cu interface. Previously published results are shown in parentheses. As discussed in Sec. (2.3), the spin dependent conductance (or polarization) of a single Co-Cu interface is sufficient to explain the GMR seen in

System	$G_{\text{maj}}^{\text{bare}}$	$G_{\text{min}}^{\text{bare}}$	P	$G_{\text{maj}}^{\text{Schep}}$	$G_{\text{min}}^{\text{Schep}}$	$G^{\uparrow\downarrow}$
Co	.47 (.46)	1.19 (1.08)	-.43 (-.40)	-	-	-
Cu	.56 (.58)	.56 (.58)	0	-	-	-
Co/Cu	.43 (.44)	.33 (.32)	.13 (.16)	2.53 (3.03)	0.59 (0.56)	.43

Table 7.1: Sharvin conductance per area for bulk Co and Cu, and interface conductance per area for single Co-Cu interface, shown in units of $10^{15} \Omega^{-1} \cdot m^{-2}$. Values in parentheses are taken from Ref. [42] (the lattice constant of Ref. [42] is taken to be $a = 3.61 \text{ \AA}$). The polarization in the table is taken from the bare conductance. The Schep conductance G^{Schep} and mixing conductance $G^{\uparrow\downarrow}$ are defined in Sec. (3.4.1) and (3.5). The Schep polarization has a value of 0.62.

these systems.

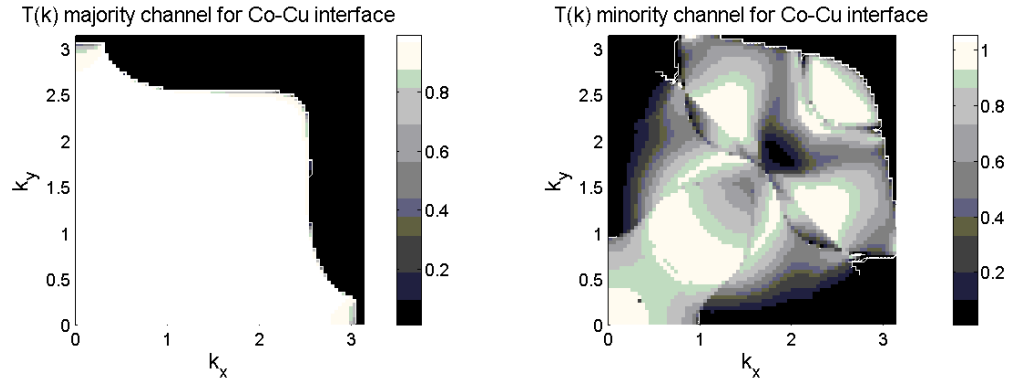


Figure 7.2: Transmission as a function of transverse wave vector. The majority channel shows almost uniform transmission, while the minority channel shows a complicated structure.

Fig. (7.2) shows the spin dependent transmission as a function of wavevector perpendicular to the current direction ¹ for a single Co-Cu interface. As expected from Fermi surface considerations, the transmission is nearly uniformly unity for the majority channel, while for the minority channel shows a rich, complicated structure. (The transmission probability is obtained by summing over bands: $T_k =$

¹All of these systems have 2-d periodicity transverse to the current direction, and therefore a 2-d Brouillon zone.

$\sum_{mn} |T_{mn}|^2$, where T_{mn} is the transmission amplitude from state (band) n to state (band) m .) The property that $T_{k_{\parallel}}^{\text{maj}} \approx 1$ for most k_{\parallel} has important consequences for calculations which assume specular scattering, as will be discussed in later sections.

7.3 Co-Cu-Co trilayer

To find the magnetoresistance and spin transfer torques present in a typical experimental geometry, we first consider the system of left Co lead, Cu spacer (6 ML), and right Co lead. We include 13 buffer Co layers of the lead in the system. Fig. (7.3) shows the geometry of the system. We are interested in the transport properties and spin torques as we vary the relative angle of magnetization between the 2 Co leads. We first perform a self-consistent calculation for the collinear Co-Cu-Co system. We then coherently rotate one of the Co leads, and find the resulting (non-self-consistent) transmission and torques (as described in sec (6.6))². In the first set of figures, we also include data points obtained by starting from the anti-parallel self-consistent collinear solution and rotating to the desired orientation. At nearly anti-parallel configurations, the differences between rotating from an initially parallel and anti-parallel state are small, and disappear rapidly as the angle is decreased away from 180°.

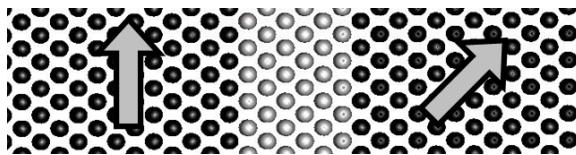


Figure 7.3: Coordinates used in trilayer (2-interface) calculation.

In Fig. (7.4), we show the conductance vs. angle. This data yields a

²We have found self-consistent rotated configurations can be obtained, but the results for transmission and torques are unchanged. This is because the interlayer exchange are very weak.

magnetoresistance of 30%. A more experimentally relevant quantity is $\Delta RA = (R_P - R_{AP})A = 0.61 \cdot 10^{-15} \Omega \cdot m^2$. This is somewhat higher than the experimental values of $\Delta RA = (0.48 \pm .02) \cdot 10^{-15} \Omega \cdot m^2$ [29]. The overall RA value for our calculation is about $1.7 \cdot 10^{-15} \Omega \cdot m^2$, compared to experimental values of $2.1 \cdot 10^{-14} \Omega \cdot m^2$ - we do not expect agreement here even in the ballistic regime since experimental stacks include several more layers than our calculation. As expected, the experimental resistance is therefore larger than the calculated resistance.

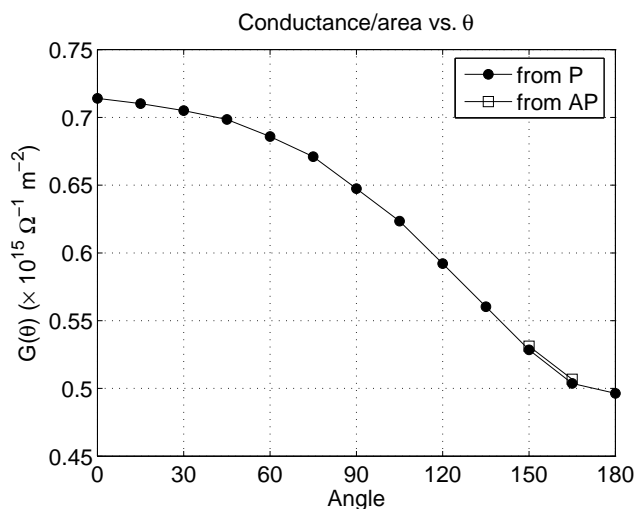


Figure 7.4: Conductance per area vs. relative layer orientation for the Co-Cu-Co trilayer. A magnetoresistance of 30% is obtained. The data labelled “from AP” represent configurations obtained by rotating away from the collinear anti-parallel ground state.

Fig. (7.5) shows the spin current polarization as a function of the Co layers’ orientation. $P = .18$ for the parallel configuration, and eventually decays to 0 at anti-parallel configuration (symmetry requires $T^{\text{maj}} = T^{\text{min}}$ in the AP configuration). The polarization is nearly constant for $\theta = 0$ to 90° . The polarization for parallel alignment ($P = .18$) is greater than the single interface polarization ($P = .12$). This is due to phase coherent effects, as described in detail in the Sec.

(7.5).

When the layers are non-collinear, the spin current in the system is no longer described by a two-channel model of independent spin-up and spin-down current. Fig. (7.5) shows the direction of the spin current in the spacer as a function of the relative orientation of the layers. The direction of the spin currents is exactly halfway in between the direction of the two Co layers. From this observation we can simply understand several aspects of the spin torques present in the system (see next section). Fig. (7.6) is a cartoon showing the spin current direction for a given magnetic configuration.

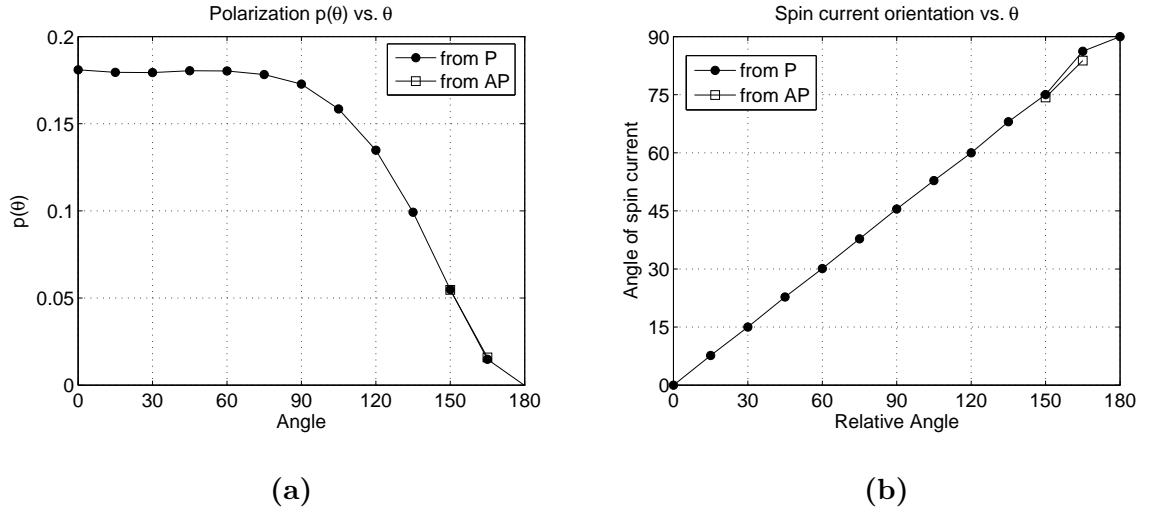


Figure 7.5: Polarization and direction of spin current versus relative layer orientation. The angle of the spin current in the spacer is $\theta/2$. $p(\pi) = 0$ as required by symmetry.

7.3.1 STT in Co-Cu-Co trilayers

We next consider the STT for the trilayer calculation. We are most interested in finding $g(\theta)$ - the angle-dependent STT efficiency. (Recall the expression for the efficiency is given by $g(\theta) = \text{STT}/I \sin(\theta)$.) In all the data presented, g has units

of $\mu_B/e = 5.78 \cdot 10^{-5} (J/T \cdot C)$. In these units, the inequality $0 \leq p \leq 1$ implies $0 \leq g \leq 2$. Physically, this means a single electron has only a certain amount spin angular momentum it can donate to the magnetization.

Before we go on to present the calculated spin transfer torques, we can anticipate their form from the data shown so far. The torque is given by the component of the spin current flux that is perpendicular to the magnetization. Since the direction of the spin current deep inside the FM is parallel with the magnetization, the spin current in the spacer determines the spin torques on the two Co layers.

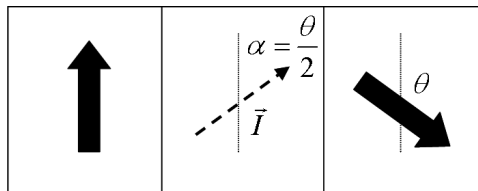


Figure 7.6: Geometric illustration of the spin current orientation in the spacer and relative layer orientation. If the polarization is assumed to be independent of θ , the increase of efficiency with θ follows simply from this geometrical consideration.

If the magnitude of the spin current is denoted by $IP(\theta)$, then its components are given as:

$$I_z = \left(\frac{1 + \cos(\theta)}{A(\theta)} \right) IP(\theta) \quad (7.1)$$

$$I_x = \left(\frac{\sin(\theta)}{A(\theta)} \right) IP(\theta) \quad (7.2)$$

$$A(\theta) = \sqrt{2(1 + \cos(\theta))} \quad (7.3)$$

As written above, the factor $A(\theta)$ ensures that the first factors in the parentheses are normalized and represent only the direction of the spin current. The efficiency

factor for the torques on both FM layers is found as:

$$g_{\text{estimate}}(\theta) = \frac{\text{STT}}{I \sin(\theta)} = \frac{P(\theta)}{A(\theta)} = \frac{P(\theta)}{2} \sec(\theta/2) \quad (7.4)$$

In his original paper on spin torques, Slonczewski derived the following explicit expression for g for a simplified model calculation [24]:

$$g_{\text{Slonc}}(\theta) = 2 \left[-4 + (1 + P)^3 (3 + \cos(\theta)) / 4P^{3/2} \right]^{-1} \quad (7.5)$$

Fig. (7.7) shows the results for g from our full NEGF calculation. Shown for comparison is the efficiency g_{estimate} (Eq. (7.4)) of our simple estimation assuming a constant $P(\theta)$, and that of Slonczewski. Both g_{estimate} and g_{Slonc} increase monotonically with angle - this is due to the fact that in both cases, the angular dependence of P is ignored. The efficiency of g_{estimate} (Eq. (7.4)) matches well with the calculated results for $\theta < 90^\circ$, demonstrating the simple geometric analysis of the spin currents works well for angles where the polarization is constant. However, at larger angle, the polarization decreases more rapidly than the angular factor $\sec(\theta/2)$ increases, leading to a net decrease in g . So far, there is no experimental evidence for a strong angular dependence of g [92].

One can make further comparison to experiment by finding the amount of torque delivered per current. This quantity can be extracted from experimental data by finding the slope of the linear relation between critical current and applied field (see Sec. (6.3.2)). The experiment in Ref. [28] gives a slope of 2.9 mA/1 T. The resulting spin torque per current (or spin torque efficiency $g(\theta)$ at $\theta = 0$) is given by

$$\frac{\alpha\gamma(1.0 \text{ T})M_s V}{2.9 \text{ mA}} = .35 \mu_B/e. \quad (7.6)$$

Here α is the bulk magnetic damping of Co, assumed to be .007, M_s is the bulk

magnetization of Co, and V is the volume of the free layer.

This small cone angle efficiency ($g(\theta = 0)$) is nearly identical to the effective efficiency determined from point-contact reversal experiments [93]. Our theoretical value, $g(\theta = 0) = 0.09$, is therefore smaller than the experimental value for Co/Cu/Co pillars by approximately a factor of 4. We make further comparisons to this efficiency for diffusive models in the next section.

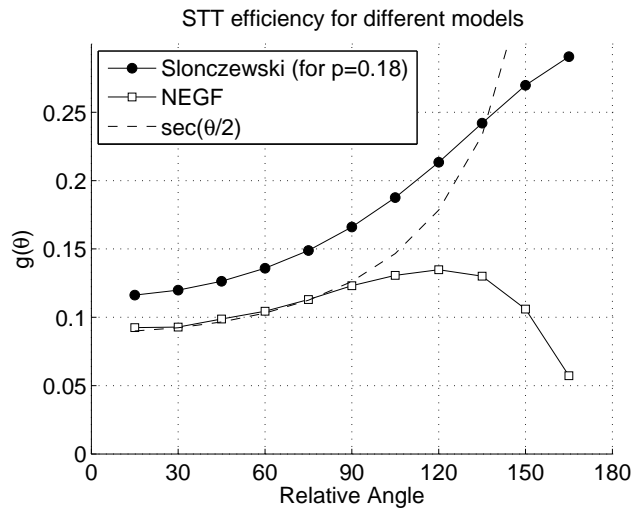


Figure 7.7: Spin transfer efficiency g for NEGF calculation, and Slonczewski and simple estimate formulas.

7.4 Ballistic vs Diffusive calculations

The calculations performed within the NEGF framework represent a purely ballistic system: phase coherent effects are fully included and the interface scattering is specular. To highlight the role of these effects, we first consider the differences between the ballistic results and the results obtained for the same system treated in the diffusive limit. As discussed in Sec. (3.5), the diffusive limit differs from the

ballistic in two important respects: there is no phase coherence, and the interface scattering is diffusive (purely non-specular). The treatment of the diffusive case is done here with the machinery of magnetoelectronics, or spin-circuit theory (SCT) [42].

SCT was described in Sec. (3.5). We briefly re-iterate here that it can be thought of essentially as Ohm’s and Kirchoff’s Laws generalized to noncollinear spin space. We consider only interface resistance, so that a trilayer spin-valve type structure can be mapped into a simple Kirchoff-like circuit:

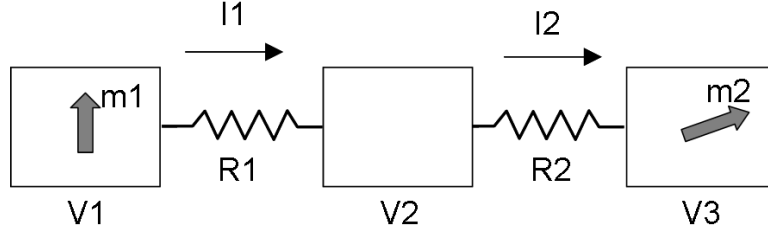


Figure 7.8: Equivalent circuit model for trilayer calculation. The “resistors” represent the interfaces.

The input parameters of the theory describing a system are simply the values of the resistivities (or of conductivities), which we have already calculated in Sec. (7.2), and the applied bias potential. The so-called “spin-mixing” conductance parameter $G_{\uparrow\downarrow} = \sum_{mn} (T_{mn}^{\uparrow})^* T_{mn}^{\downarrow}$ emerges from the noncollinear treatment of the system, and is related to the spin transfer efficiency. For the simple symmetric trilayer, we can give an explicit expression for the charge current and spin torque efficiency g_{diff} in the system as a function of θ . In terms of the parameters $G =$

$G^\uparrow + G^\downarrow$, $P = (G^\uparrow - G^\downarrow)/G$, $\eta_R = \text{Re}[G^{\uparrow\downarrow}]$, they are:

$$I = \frac{G}{2} \left[1 - P^2 \frac{\tan^2(\theta/2)}{\eta_R + \tan^2(\theta/2)} \right] V \quad (7.7)$$

$$g_{\text{diff}}(\theta) = \frac{\tan(\theta/2)}{(1 - P^2) \tan^2(\theta/2) + \eta_R} \eta_R P \quad (7.8)$$

Plugging in calculated values of these parameters from Table (7.1), we can determine the transport properties in the diffusive limit of our system. Fig. (7.9) and (7.10) contrast the conductance and spin transfer efficiency for the ballistic (NEGF) and diffusive (SCT) regimes.

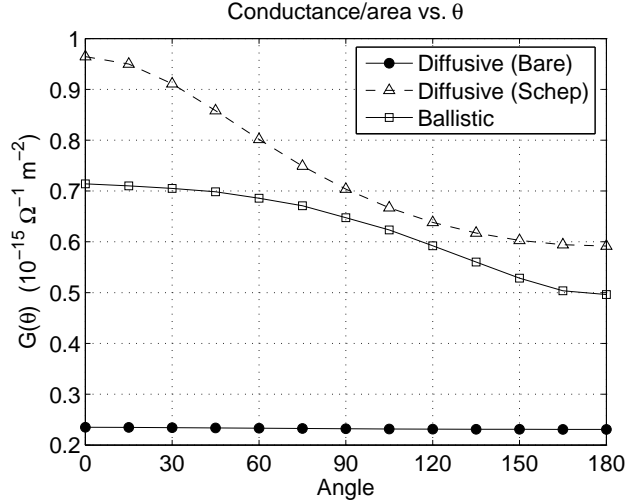


Figure 7.9: Angular magnetoresistance for two models: NEGF (ballistic) and spin circuit theory (diffusive). The Schep magnetoresistance is larger due to its omission of contact resistance.

The results are strongly dependent on which conductance parameters are chosen - the bare conductivities or the Schep interface conductivities. We include both sets of data to illustrate the large difference between the choice. As discussed in Sec. (3.4.1), the Schep conductivities are more appropriate to use for metallic

interfaces. We will comment on the differences between the NEGF ballistic result and both sets of diffusive results below.

We consider first the results obtained with G^{bare} . Here the polarization, GMR, and spin transfer efficiency are all substantially reduced. These reductions are due mostly to the loss of specular scattering (as opposed to the loss of phase coherence). If we use Eq. (3.28) to compose the single interface transmission probabilities for each k_{\parallel} channel separately (which amounts to losing phase coherence but retaining specular scattering), we obtain results similar to the NEGF ballistic calculation. The reductions in polarization and GMR occur when we compose the k_{\parallel} -averaged transmission probabilities of Table (7.1) (which constitutes fully non-specular scattering). The appropriate choice for composition method depends on the degree of specular/diffuse scattering at the interface (which in turn depends on the roughness of the interface among other things), and on the ratio of spacer thickness to mean free path. For flat interfaces and thin spacers, k_{\parallel} -resolved composition of transmission probabilities is appropriate, while for rough interfaces and/or thick spacers, k_{\parallel} -averaged composition of transmission probabilities is appropriate.

When we use G^{Sh} for the diffusive conductivities, the polarization, GMR, and spin transfer efficiency are now all substantially increased relative to the NEGF calculation. This enhancement is because the NEGF calculation includes the contact (Sharvin) resistance of the Co lead: since the Sharvin resistance is greater in the Co majority channel than minority channel, its inclusion reduces the polarization. In the diffusive calculation with G^{Sh} , this Sharvin resistance is removed, and the polarization is therefore increased to a value of $p = .62$ for the parallel configuration. As discussed in Sec. (7.3.1), the experimental efficiency is approximately $g(0) = .35$. It is seen that the diffusive calculation agrees well with this result.

To make a proper comparison with NEGF, we should subtract off the Sharvin resistance from the NEGF result. When we do so, we obtain a GMR of nearly 100%,

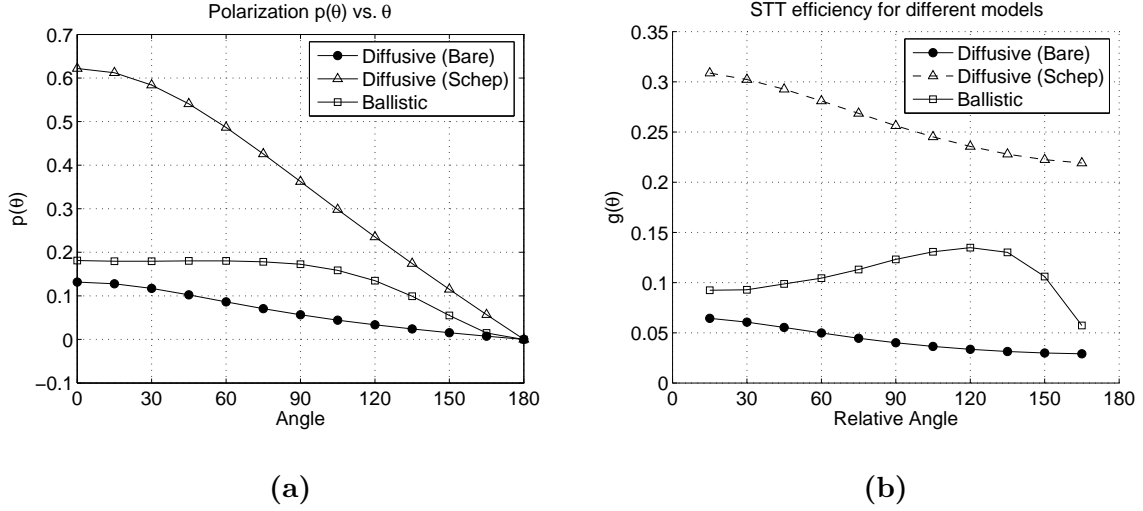


Figure 7.10: Polarization P and spin transfer g vs θ for diffusive and ballistic regimes. The initial decrease of p_{diff} causes g_{diff} to decrease monotonically.

and a polarization of nearly 1. This is due to the fact that the majority channel resistance (in the parallel alignment) is 3 orders of magnitude smaller than the minority channel, which is due to the fact that $T_{k_{\parallel}}^{\text{maj}} \approx 1$ in the parallel configuration. As discussed in Sec. (3.4.1), the experimental method (2-probe vs 4-probe) determines the appropriate choice for including or not the contact resistance. Common experimental systems for spin valves are of a 2-probe form, so that contact resistance should ultimately be included. Nonetheless it would be preferable to perform an NEGF calculation with spin-independent contact resistance, by using Cu leads, for example. In this case the contact resistance would not affect the polarization. It is however difficult computationally however to include isolated FM layers in the calculation, as they must be thicker than the spin transfer decay length (which is about 3 nm [44], see Fig. (6.4) of Sec. (6.7)).

An example of a calculation with Cu leads is found in Ref. [94]. The system is [Cu lead - Co - Cu - Co - Cu lead] and shows a parallel alignment polarization of 36%, which would yield a $g(0) = 18\%$ - approximately twice the $g(0)$ calculated

here. This demonstrates that in future studies it may important to use nonmagnetic leads in calculating spin transfer efficiencies for FM materials.

7.5 Ballistic calculation - 2 vs 3 interface results

To elucidate the role of phase-coherent scattering in ballistic calculations, we next consider a system with an added interface. The geometry is: [Co lead - (9ML) Cu - (15ML) Co - Cu lead]. Fig. (7.11) shows the atomic configuration. In Fig. (7.12), the transmission for 2 vs 3 interface system is shown. As expected, the addition of another scattering interface reduces the conductance. The value for ΔRA for 3-interface is $.74 \cdot 10^{-15} \Omega \cdot m^2$, larger than the 2-interface value (which was $0.61 \cdot 10^{-15} \Omega \cdot m^2$).

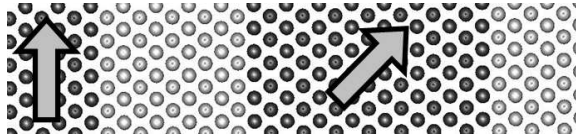


Figure 7.11: Coordinates used in 3 interface calculation.

Fig. (7.12b) shows the polarization of the 2 and 3-interface systems. In this case, the polarization is increased for 3-interfaces, and does not fall to 0 as the orientation of the layers approaches 180° . The increase in polarization can be understood from Fig. (7.13). This shows the k -resolved transmission for the parallel configuration. Because of the matching Fermi surface, the majority channel is nearly unaffected by the addition of another interface. The minority channel transmission is further complicated by another interface, and reduced overall. The additional structure of the transmission function is a result of resonant reflection, which is shown in Fig. (7.14). The original transmission is modulated by phase coherent effects, which reduce the transmission probability at certain values of k .

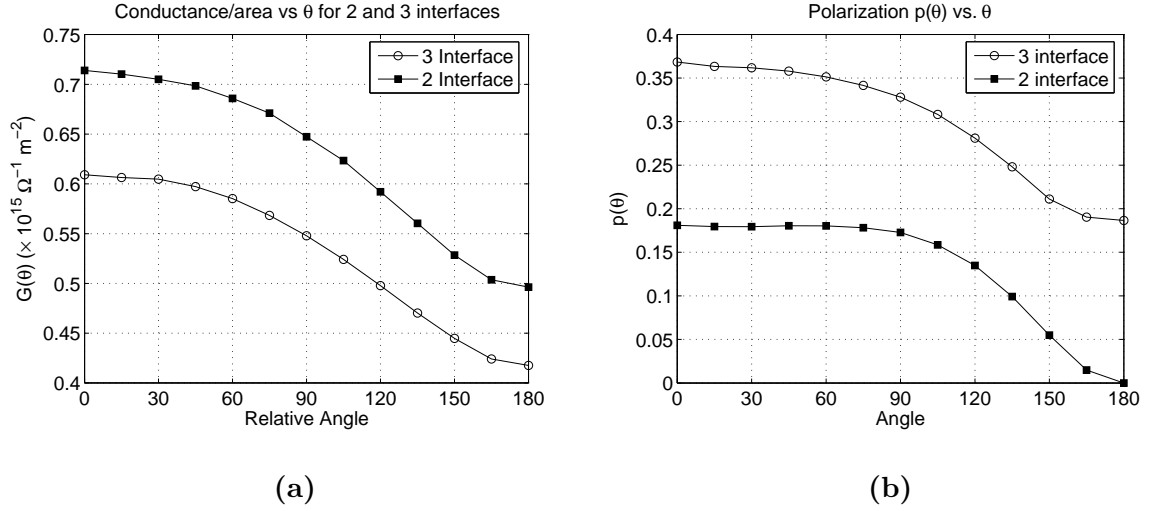


Figure 7.12: Conductance per area and polarization for 2-interface (trilayer) and 3-interface systems. As expected, the conductance is reduced and polarization increased for the 3-interface system. Also, the polarization does not decay to 0 for 3-interface AP configuration.

Fig. (7.15) next shows the spin transfer and spin transfer efficiency for the 2 and 3-interface systems. As anticipated, the larger polarization causes a generally larger spin transfer torque for the 3 interface system. However at small angle, the 2-interface system has a larger efficiency. This can be explained by the direction of the spin current. Fig. (7.17) shows the angle of spin current in the spacer layer for both systems. In the 2-interface system, the spin current angle is almost exactly $\theta/2$. In the 3-interface case, the angle grows much more rapidly, and eventually reaches 180° . This means that at AP alignment, the spin down electrons have a higher transmission. This can be traced back to phase coherent effects - as shown in Fig. (7.16), up spins undergo resonant reflection in the AP alignment, reducing their transmission with respect to down spins. This effect is manifest at smaller free layer angles as well, and is responsible for the larger angle of spin current in the 3-interface case. At small free layer angle, this results in a smaller transverse

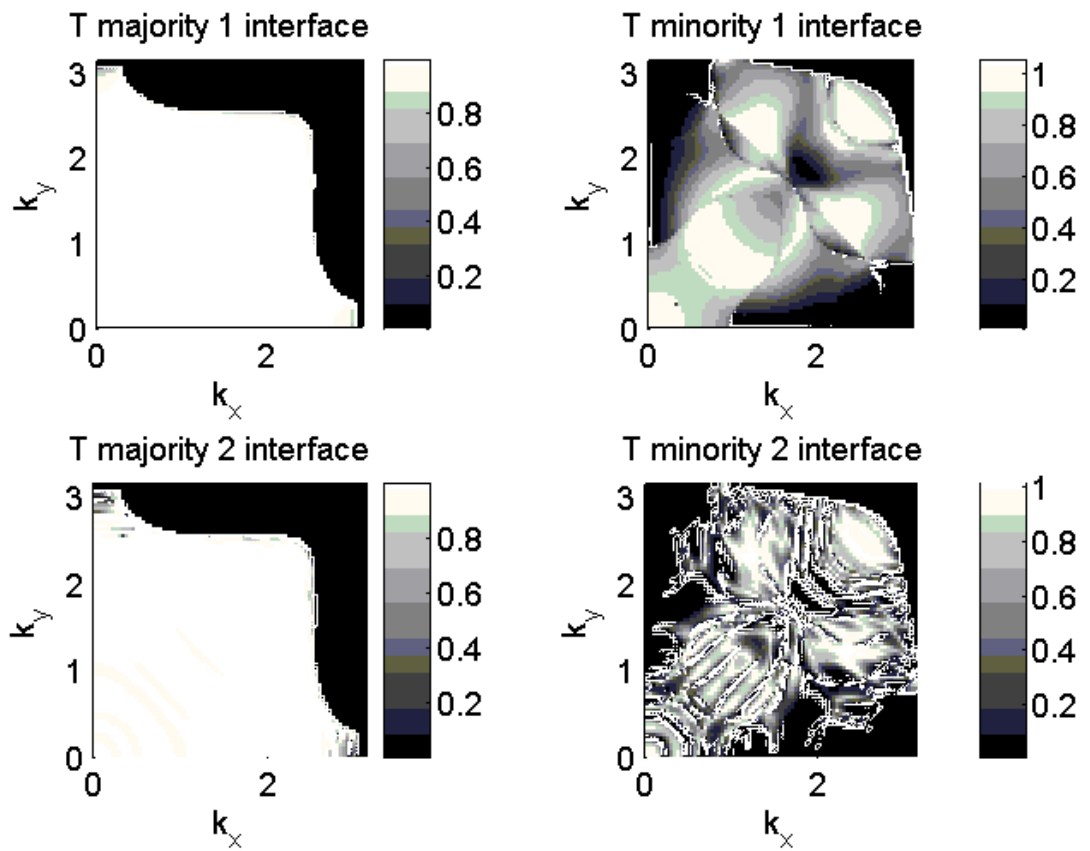


Figure 7.13: Transmission function for single interface vs. 2 interfaces. The 2 interface case is for parallel Co alignment.

component of the incoming spin current, causing a reduced efficiency with respect to the 2-interface case. At larger free layer angle, the larger polarization more than compensates for this, making the spin transfer efficiency larger for the 3-interface system.

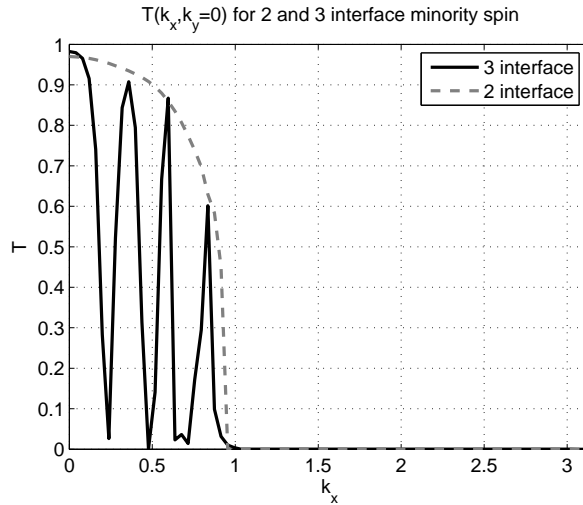


Figure 7.14: 2 vs 3 interface transmission along the k -space line $k_y = 0$, $k_x \in [0, \pi]$. The 3 interface case shows a structure related to resonant reflection.

7.6 Dual Spin Filter

Finally we consider adding yet one more interface. This time, the idea is to test a proposed configuration that is designed to increase spin transfer efficiency [95]. The system consists of [Co lead - Cu(6 ML) - Co(ML) - Cu(ML) - Co lead] (the coordinates are shown in Fig. (7.18)). The orientation of the two Co leads are taken to be anti-parallel. The idea behind the design is that the central Co layer (the free layer) is to experience a spin transfer torque from the upstream FM tending to align it, and a torque from the downstream FM tending to anti-align it. Since the upstream and downstream FM are anti-parallel, these torques act cooperatively in the same direction, thereby increasing the total torque. (A similar configuration in which Co leads are parallel is proposed to reduce the spin transfer torque).

We perform the calculation as before, and Fig (7.19) shows the spin transfer torques for the 2 and 3 interface systems, along with the DSF system. There is considerable enhancement of the efficiency, by about a factor of 3. If one considers

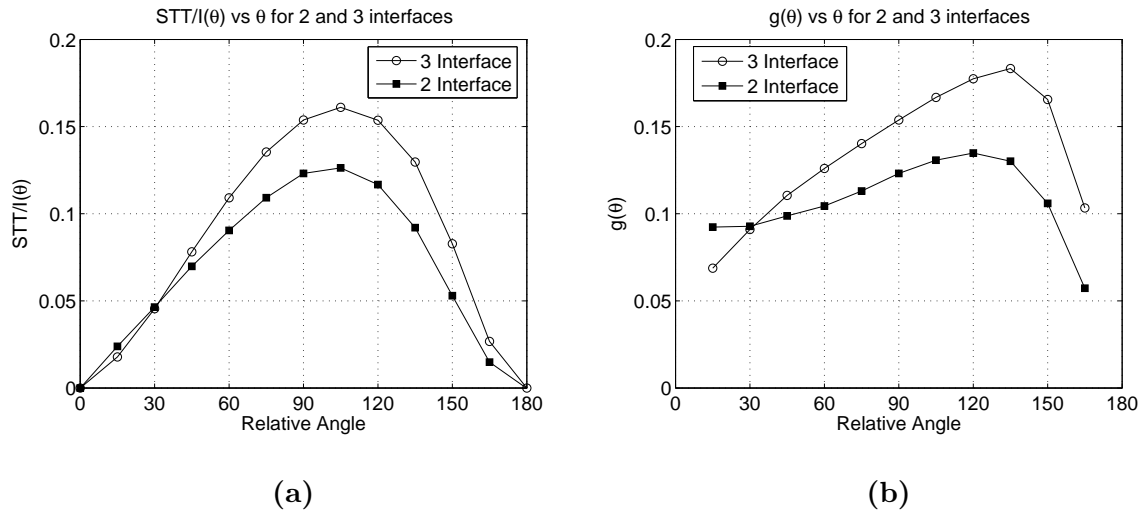


Figure 7.15: Spin transfer per current versus angle, and spin transfer efficiency vs. angle for 2-3 interface systems. The spin torque is generally larger for the 3 interface case, because of the larger polarization.

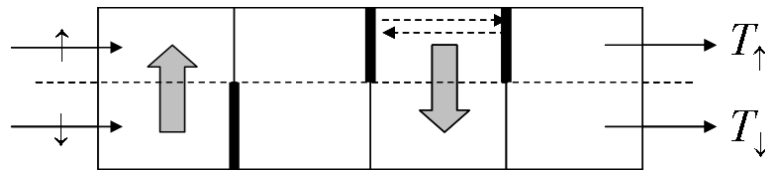


Figure 7.16: Schematic showing the resonant behavior present in the majority channel in the AP configuration. This leads to a $T_{\downarrow} > T_{\uparrow}$ in the AP configuration.

the spin torque delivered per bias voltage, the DSF system shows an enhancement of a factor of 2, which might be a naive guess of the enhancement factor. The additional interface reduces the transmission by about a factor of 1/2, so that the torque per current is then increased by a factor of 3.

Fig. (7.19) shows the layer resolved torques for the DSF system. As expected, the torques act on both interfaces of the free layer.

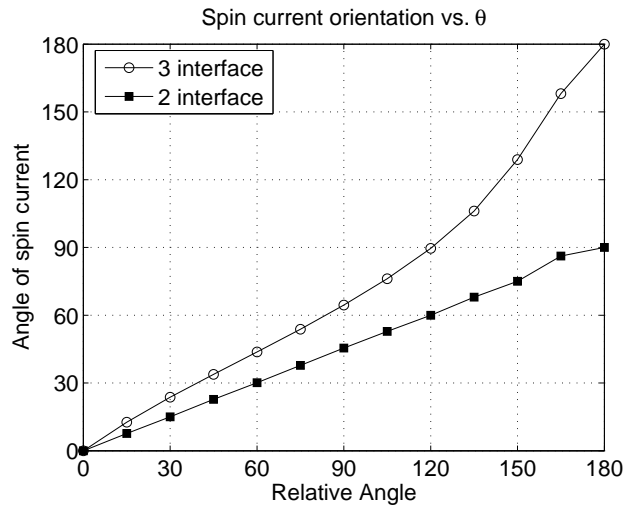


Figure 7.17: Spin current angle in the spacer vs. relative orientation for 2 and 3-interfaces. The larger angle of the 3-interface system is a consequence of resonant reflection in the majority channel.

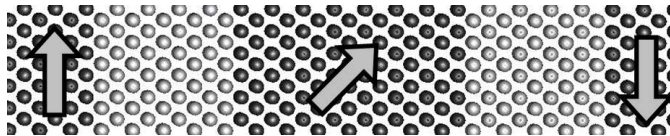


Figure 7.18: Coordinates of the DSF stack configuration.

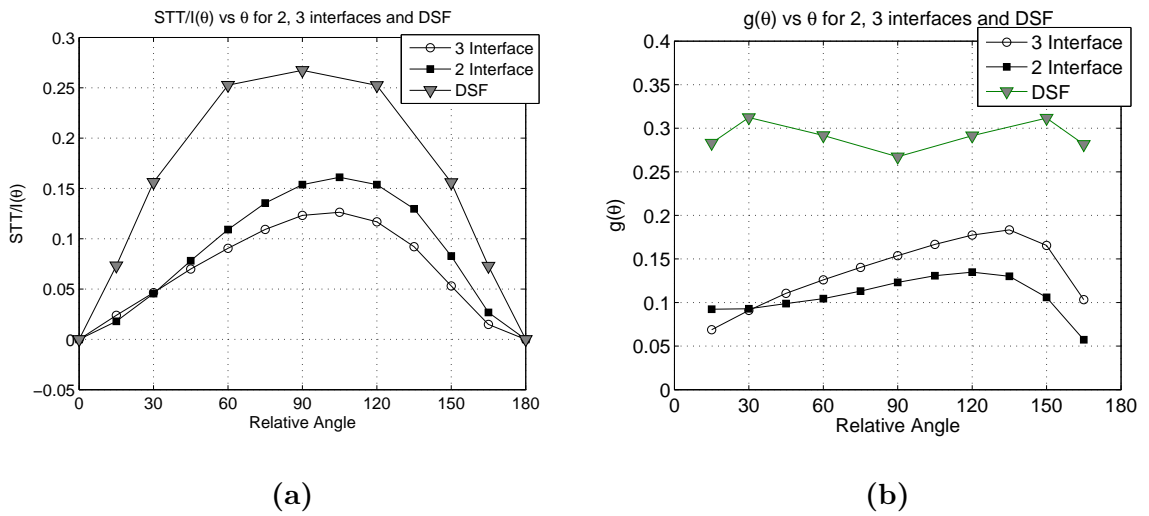


Figure 7.19: Spin transfer torque and efficiency for 2,3 interface systems and DSF system. As expected, the DSF system shows considerable enhancement of STT efficiency.

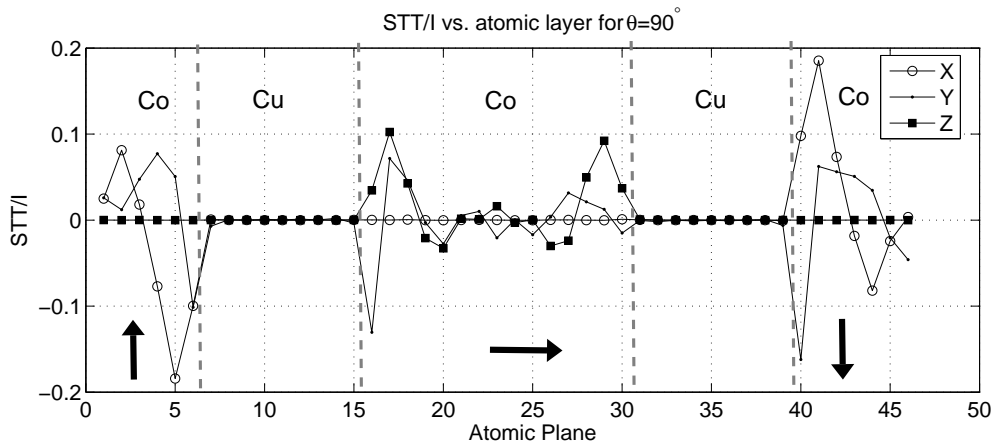


Figure 7.20: Layer resolved spin torques for DSF stack. The spin torques are localized at both interfaces of the free layer, and act cooperatively to increase the spin transfer efficiency.

Chapter 8

Spintronics in Antiferromagnets

The contents of this chapter are partially based on the articles:

Alvaro Núñez, Rembert Duine, Paul Haney, and Allan MacDonald, *Theory of spin torques and giant magnetoresistance in antiferromagnetic metals*, Phys. Rev. B, **73**, 214426 (2006).

Paul Haney, Derek Waldron, Rembert Duine, Alvaro Núñez, Hong Guo, and Allan MacDonald, *Ab initio giant magnetoresistance and current-induced torques in Cr/Au/Cr multilayers*, Phys. Rev. B, **75**, 174428 (2007).

8.1 Introduction

In this chapter we consider spintronic effects (GMR and STT) in anti-ferromagnetic systems. Some of the fundamental characteristics of these effects in anti-ferromagnets are qualitatively different than in ferromagnets. Our conception of STT as the result of local torques between nonequilibrium quasiparticles and an order parameter is especially useful in the context of anti-ferromagnets. Since the total spin of an anti-ferromagnet is 0, conservation of spin angular momentum does not uniquely

determine order parameter dynamics in the presence of a current.

To date, the role of antiferromagnets in spintronic applications has been limited to pinning a ferromagnetic layer's orientation via the exchange bias effect. (Exchange bias refers to the unidirectional anisotropy acquired by a magnetic layer when it is adjacent to an antiferromagnetic layer, and was first observed in 1956.) We indeed propose that the application of current can affect exchange bias. However we additionally propose that antiferromagnet materials alone can function as the basic building blocks of circuits that exhibit effects like GMR and CIMS. These effects in antiferromagnets are somewhat analogous to those in ferromagnets, with the staggered order parameter of the antiferromagnet playing the role of the magnetization of a ferromagnet. There are, however, a number of qualitative differences.

The organization of this chapter is as follows: in Sec. (8.2), we review some general properties of metallic antiferromagnets. In Sec. (8.3), we discuss the properties of GMR and STT present in toy models of antiferromagnets. In Sec. (8.4), we describe the results of a NEGF+DFT calculation for a realistic antiferromagnetic system.

8.2 Antiferromagnets - general properties

Antiferromagnetic materials exhibit a periodic spin density - referred to as a spin density wave (SDW) - below a critical temperature T_N (the Néel temperature). This periodicity is described by a wave vector \mathbf{Q} , which may be commensurate or incommensurate with the underlying lattice. From a microscopic point of view, antiferromagnetism in metals is usually due to approximate nesting of the Fermi surface, and the spin wave vector \mathbf{Q} is precisely the nesting vector. Examples of metallic antiferromagnets include elemental Cr [96] and the alloys NiMn [97] and IrMn [98], among others. The vanishing net magnetic moment and microscopic spin periodicity makes antiferromagnets considerably more difficult to study experimen-

tally than ferromagnets, and their existence was first directly demonstrated only in 1953 by Shull and Wilkerson using neutron scattering [99]. At temperatures below the spin-flop transition temperature T_{sf} , the direction of the spin \mathbf{S} is transverse to \mathbf{Q} ($\mathbf{S} \cdot \mathbf{Q} = 0$), while for temperatures $T_{sf} < T < T_N$, the spin is longitudinal with respect to \mathbf{Q} ($\mathbf{S} \times \mathbf{Q} = 0$). The energy bands of antiferromagnets are not spin-split, and indeed the only qualitative imprint of the ordered state on the electronic structure is the formation of a gap at the SDW vector.

Antiferromagnets have been the subject of intense study for decades [100]. Recent work includes experimental study of the time evolution of the \mathbf{Q} -domain structures in Cr [101, 102]. It is found that the domain wall structure changes due to thermal fluctuations and quantum tunnelling effects. Other research has considered SDW properties in thin films and multilayer structures. It is found that Cr can exhibit paramagnetism as well as commensurate and incommensurate SDW states, depending on the film thickness and on the adjacent materials [103, 104, 105, 106, 107]. The spintronic effects in AFM examined in this chapter may have implications for some of these recent studies.

8.3 GMR and CIT in an AFM - toy model approach

8.3.1 General properties

As discussed in Ch. 2, MR and STT effects in ferromagnets rely on the interplay between electron transport and magnetic order. The source of this interplay is the strong spin-dependent exchange-correlation potentials seen by current-carrying electrons, which leads to a spin-dependent Fermi surface. Antiferromagnets do not possess a spin dependent Fermi surface, the characteristic that is so essential to conventional spintronics, so it is clear that any MR and STT effects in AFM circuits must have a fundamentally different origin. As an initial attempt to understand

spintronic effects in an AFM, we consider a single-band tight-binding model of an AFM. The AFM order is modelled by introducing a spin-dependent exchange field that alternates in sign on every other lattice site, and points in direction $\pm \mathbf{n}$ (the full Hamiltonian is given explicitly in Eq. (8.4)). In this model, the essential properties of spintronic effects can be understood from the scattering matrix of a single AFM unit cell, as we describe below.

Invariance under simultaneous rotation of \mathbf{n} and quasiparticle spins allows us to write each transmission and reflection matrix in the scattering matrix as a sum of a triplet and a singlet parts

$$\mathcal{S} = \mathcal{S}_s + \mathcal{S}_t \mathbf{n} \cdot \boldsymbol{\tau} . \quad (8.1)$$

Because the system is invariant under simultaneous space and time inversion, the scattering matrix must be invariant under this operation. The most general form of \mathcal{S} allowed by this symmetry operation is [108]:

$$\mathcal{S} = \begin{pmatrix} r_s + r_t \mathbf{n} \cdot \boldsymbol{\tau} & t'_s \\ t_s & r_s - r_t \mathbf{n} \cdot \boldsymbol{\tau} \end{pmatrix} . \quad (8.2)$$

The transmission amplitudes from left and right are spin-independent and the reflection amplitudes from left and right differ only by spin-reversal. The parameter space is further constrained by unitarity. This allows us to write

$$\begin{aligned} r_s &= i e^{i\nu} \sin \Theta \cos \Phi ; \\ r_t &= e^{i\nu} \sin \Theta \sin \Phi ; \\ t'_s &= e^{i(\nu-\xi)} \cos \Theta ; \\ t_s &= e^{i(\nu+\xi)} \cos \Theta , \end{aligned} \quad (8.3)$$

where ξ and ν are phases that so far are independent parameters, and Θ and Φ

are the polar coordinates of a sphere of radius unity. This is the most general form for spin-dependent scattering by a integer number of periods of a one-dimensional spin-density-wave [108].

This form of the scattering matrix reveals several key properties of scattering from a single antiferromagnetic layer. First, the reflection *amplitudes* are spin-dependent, while the reflection and transmission *probabilities* are spin-independent. This indicates that a single AFM layer does not act as a spin filter, or does not induce a spin-polarized current. From the discussion of simple models of magnetoresistance in Sec. (2.3), this would suggest that there are no magnetoresistance effects. However this turns out not to be the case, as we describe in the next section.

8.3.2 AGMR in toy model

Despite the fact that a single AFM does not induce a spin-polarized current, the scattering matrix implies a nonzero MR. For a system with two antiferromagnets with respective staggered moment orientations \mathbf{n}_1 and \mathbf{n}_2 separated by an arbitrary paramagnetic spacer, the composed transmission depends on the relative orientation of \mathbf{n}_1 and \mathbf{n}_2 . This can be shown, for example, by explicitly composing two AFM scattering matrices [108].

We adopt a less general approach here and calculate antiferromagnetic giant magnetoresistance (AGMR) for a simple model of an anti-ferromagnet. We describe the system with a single-band tight-binding model:

$$\begin{aligned} \mathcal{H}_k &= -t \sum_{\langle i,j \rangle, \sigma} c_{k,i,\sigma}^\dagger c_{k,j,\sigma} + \text{h.c.} \\ &+ \sum_{i,\sigma,\sigma'} \left[(\epsilon_i + \epsilon_k) \delta_{\sigma,\sigma'} - \Delta_i \hat{\Omega}_i \cdot \vec{\tau}_{\sigma,\sigma'} \right] c_{k,i,\sigma}^\dagger c_{k,i,\sigma'} . \end{aligned} \quad (8.4)$$

Here, k denotes the transverse wave number, t the hopping amplitude and ϵ_k the transverse kinetic energy. The second term in Eq. (8.4) describes the exchange

coupling Δ_i of electrons to antiferromagnetically ordered local moments $\hat{\Omega}_i = (-)^i \mathbf{n}$ that alternate in orientation within each unit cell. In the paramagnetic regions of the model system $\Delta_i = 0$. The on-site energies ϵ_i are allowed to change across a heterojunction to represent band-offset effects.

A system to investigate MR in AFM consists of a [AFM - N spacer - AFM] trilayer. We take the SDW vector \mathbf{Q} of the AFM to be parallel to the transport direction. We label the magnetic configurations as parallel (P) or anti-parallel (AP) according to the orientation of the layers adjacent to the spacer (see Fig(8.1)).



Figure 8.1: Cartoon of N-AFM-N-AFM-N antiferromagnetic spin valve. This configuration would be labelled “Parallel”, as described in the text.

Given the above Hamiltonian, we solve the Schrödinger equation with scattering boundary conditions according to the procedure outlined in Appendix C. From the scattering state wave functions, the transmission and spin-density of the scattering state is determined. Fig. (8.2) shows the AGMR as a function of the number of spacer sites. The AGMR is oscillatory in the number of spacer sites, as in the conventional GMR case [109, 94]. In this case, the value of AGMR oscillates around 0 (in the FM case, the GMR oscillates around a nonzero value). The AGMR of a single channel k oscillates with period kL , where L is the spacer length. This is indicative of the fact that the AGMR in this model is a phase-coherent effect.

8.3.3 CIT in AFM toy model

We now consider the current induced torques present in a circuit with non-collinear antiferromagnetic elements. Again we consider a circuit with two antiferromagnets

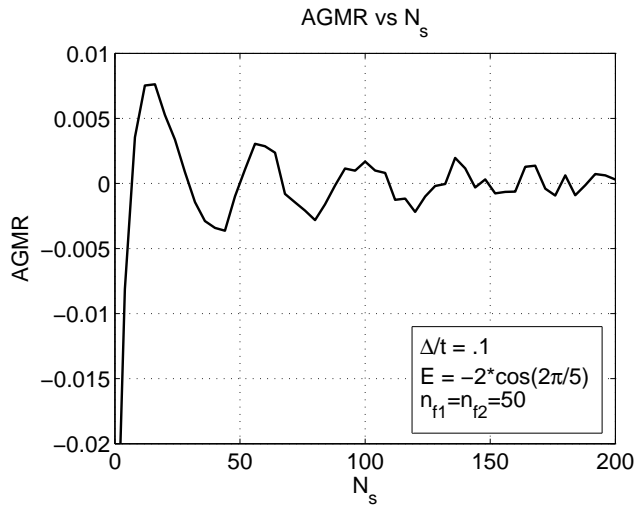


Figure 8.2: AGMR vs. spacer length for a single band 2-d toy model.

with respective staggered moment orientations \mathbf{n}_1 and \mathbf{n}_2 separated by an arbitrary paramagnetic spacer. From the form of the scattering matrix Eq. (8.3), it can be shown that the out-of-plane nonequilibrium spin density in the $\mathbf{n}_\perp \equiv \mathbf{n}_1 \times \mathbf{n}_2 / |\mathbf{n}_1 \times \mathbf{n}_2|$ direction is periodic with the lattice in the paramagnetic part of the system, and periodic with the same period as the spin density wave in the antiferromagnets [108].

As discussed in Sec. (6.6), the nonequilibrium spin density is responsible for the spin transfer torque. Therefore the spin transfer torque is *periodic* in the antiferromagnet. This is in stark contrast to the ferromagnetic case, in which the spin torques decay at the interface over a length scale on the order of $(k_\uparrow - k_\downarrow)^{-1}$ (corresponding to a value of 3 nm for Co). As we discuss later, this surprising property could potentially lead to low critical currents for induced order-parameter dynamics.

The proof of the periodicity of the out-of-plane spin density for this model is technical and unenlightening [108]. It is related to the fact that the energy bands of

an AFM are not spin-split. In Sec. (6.3) the conventional picture of spin transfer in FM is that the spin-split Fermi surface results in precessional nonequilibrium spin densities, which destructively interfere and cause the spin torques to decay rapidly away from the interface. In AFM, the nonequilibrium spin density undergoes no such precession, and the result is a non-decaying nonequilibrium spin density.

We have calculated the spin densities for the Hamiltonian of Eq. (8.4). Fig. (8.3(a)) shows the spin density for a [N-AFM-N-AFM-N]structure. In this case the AFM layers are oriented in the \hat{x} and \hat{z} directions. As expected, the out-of-plane spin density (\hat{y} component) is constant throughout the entire structure. (This calculation is for a single transverse channel). The out-of-plane spin density for a single channel is periodic in spacer length L , with period kL , indicating that it is fundamentally a phase-coherent effect, as was AGMR.

Fig. (8.3(b)) shows the spin density for a similar toy model [AFM-FM-N-FM] structure. This stack configuration is similar to that of an exchange biased spin valve. As expected, the spin transfer is localized at FM interfaces, and is constant throughout the entire AFM volume (in this calculation, we include transverse periodicity and sum over transverse channels).

Both the GMR and CITs present in toy models of this type containing AFM components rely on phase coherence. From an experimental point of view, this feature of the theory is perhaps discouraging: most experimental studies show a non-oscillatory dependence of GMR on spacer length for spin valve structures, indicating that *transport* properties do not robustly exhibit phase coherent effects [110].¹ We have modelled the effects of inelastic scattering on AFM spintronics with a spin-dependent floating probe approach similar to that of Buttiker [36], and have found that the effects do survive a moderate amount of inelastic scattering [112]. We do not go into further details on this point, however, because in the next section we will

¹In contrast, the equilibrium property of interlayer RKKY coupling is indeed oscillatory [111].

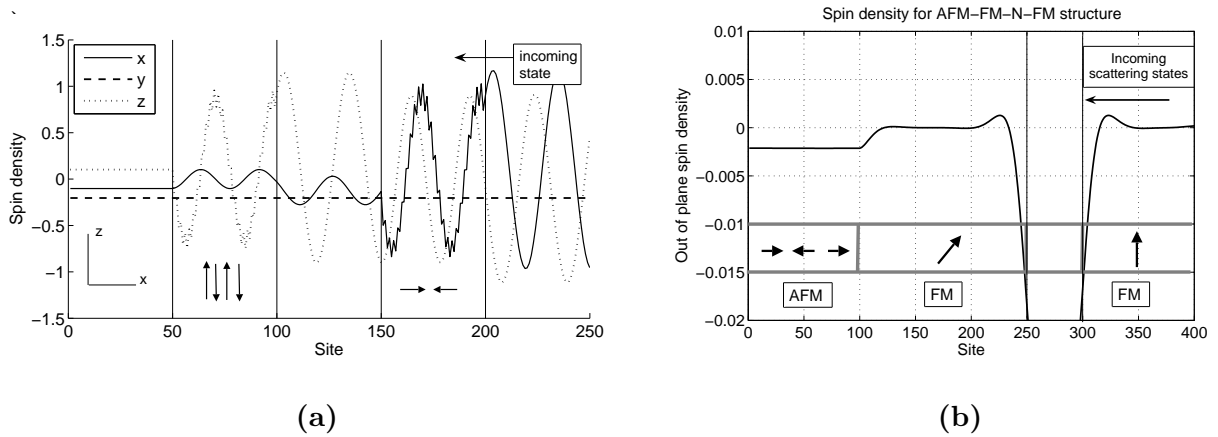


Figure 8.3: For (a): spin densities for N-AFM-N-AFM-N structure. Here $E_f = 2 \cos(.1)$, $U/t = .1$, and only single-channel is calculated. For (b): Out-of-plane spin densities (spin transfer torques) present in a AFM-FM-N-FM structure, similar to that used for exchange bias. For the data shown $E_f = 2 \cos(.5)$, $U/t = .01$, and transverse channels included.

see that in more realistic models, the role of phase coherence is not always central to spintronic effects in AFM materials.

8.4 GMR and CITs in Cr-Au-Cr

8.4.1 System details

The specific calculations we report on in this section were performed on a system with antiferromagnetic (100) growth direction *bcc* chromium (Cr) leads separated by a *fcc* gold (Au) spacer. The Cr(100)/Au(100)/Cr(100) trilayer system we consider here appears to be attractive as a model system for antiferromagnetic metal spintronics. Au/Cr multilayers and (100) growth direction epitaxy were studied some time ago both experimentally [113] and theoretically [114, 115], motivated in part by superconductivity that can occur in disordered Au/Cr films. We find that both GMR and CITs do occur in this ferromagnet-free magnetoelectronic circuit. This calculation also identifies new physics not anticipated in the toy-model stud-

ied in the previous section. The new features are associated with spin-polarized interface resonance at the Au/Cr interface and with the presence of more than one propagating Cr channel at the Fermi energy for some transverse wavevectors.

We study a circuit with semi-infinite antiferromagnetic Cr leads and a Au spacer. Cr has a *bcc* lattice structure with lattice constant 2.88 Å, while Au is *fcc* with lattice constant of 4.08 Å. The interface between these materials has a fortuitous lattice matching of two-dimensional square nets when they are grown epitaxially along the (100) direction and the Au lattice is rotated by 45° around the growth direction. In this configuration the bulk square net lattice constants differ by less than .2%. The lattice matching strains for Au on a (100) Cr substrate are therefore quite small.

The origin of antiferromagnetism in Cr is nesting between electron jack and hole neck pieces of the paramagnetic Fermi surface [96, 116]. The nesting vector \mathbf{Q} defines the spin density wave (SDW) period which is nearly commensurate with the lattice with $Qa/2\pi = .95$, where a is the lattice constant. There is evidence of antiferromagnetism in Cr thin films grown on Au substrates for coverages greater than 12 ML [117]. Density functional theory, within LSDA, has been previously used to study bulk Cr in a commensurate SDW state [118], and can predict the magnitude of the exchange splitting, the magnetic moment, and the lattice constant. For this study, we restrict our attention to Cr with a commensurate spin density wave structure in which the body center spins and cube corner spins have opposite orientations. This magnetic structure is metastable in the absence of a bias voltage for our thin film structures in the local spin-density approximation. All interfaces are perpendicular to the (100) direction.

For the GMR calculations discussed below we have used a double-zeta with polarization basis set for both Cr and Au, and have found excellent agreement with bulk band structures and density of states calculations. For the calculation of

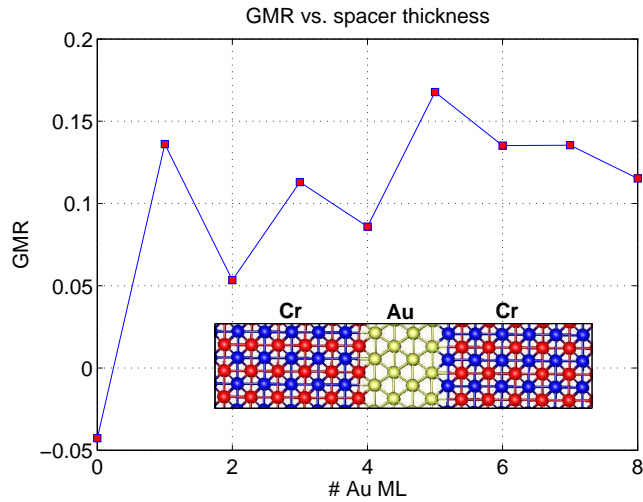


Figure 8.4: GMR as a function of spacer thickness. There is a sizable GMR for all spacer thicknesses. The inset shows the geometry for the four layer spacer configuration - up and down spins are colored red and blue (light and dark), respectively. The configuration above illustrates an anti-parallel configuration.

current induced torques, we have used a single-zeta with polarization basis set, which still retains good accuracy for bulk properties. (The reduction in basis size for the non-collinear calculation is due to memory constraints.) For the calculation of the self-consistent equilibrium density matrix, contributions from 900 k -points within the 2-d Brillouin zone have been summed. For the calculation of the conductance and current induced torques, 25600 k -points have been summed.

As before, we define parallel (P) and anti-parallel (AP) alignment below in terms of the alignment of the Cr spins in the two layers on opposite sides of the Au spacer. The inset of Fig. 1 shows the geometry and spin structure of the systems considered.

8.4.2 AGMR in Cr-Au

Fig 1. illustrates the dependence of the GMR ratio on spacer thickness. In the limit of no spacer, the GMR ratio is negative, implying larger conductances for an antiparallel configuration. This property is anticipated since the AP case at zero spacer thickness corresponds simply to ballistic conduction through bulk antiferromagnetic Cr with unit transmission coefficient for all channels, whereas the parallel configuration implies a kink in the Cr antiferromagnetic order parameter configuration which reduces the transmission. For all nonzero spacers we have studied, we find that the GMR ratio is positive. The nonzero GMR for antiferromagnetic systems is perhaps surprising at first sight; for example a simple Julliere type two-channel conductor model, in which MR is due to spin-dependent conductance in the bulk, would predict that the GMR ratio is zero for antiferromagnetic systems. For antiferromagnets GMR is, in this sense, purely an interface effect; for ferromagnets GMR is only partly (but often mainly) an interface effect.

In the case of the previous toy model antiferromagnetic calculations, GMR was due to phase coherent multiple scattering between two antiferromagnets. These effects are partially mitigated [112] at elevated temperatures by inelastic scattering which breaks phase coherence. The present ab-initio calculations reveal a new contribution to antiferromagnetic GMR, explained below, which does not rely on phase coherence. The property that realistic antiferromagnets have GMR effects that are not dependent on phase coherence is encouraging from the point of view of potential applications, since it suggests larger robustness at elevated temperatures.

In order to identify the dominant GMR mechanism of Cr/Au/Cr trilayer systems, we have performed a separate NEGF calculation for a single interface between semi-infinite bulk Cr, and semi-infinite bulk Au. The result is that there is a spin dependent conductance with magnitude $(I_{\uparrow} - I_{\downarrow})/(I_{\uparrow} + I_{\downarrow}) = -2.10\%$. The current is spin-polarized in the direction opposite to the top layer of the antiferromagnet.

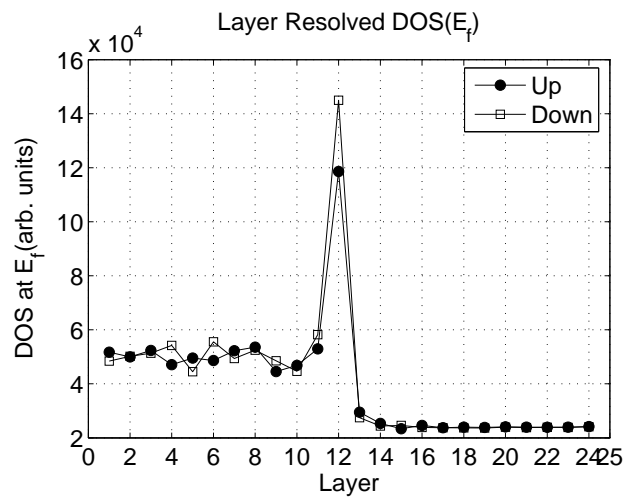


Figure 8.5: Layer and spin resolved density of states at the Fermi energy for Cr-Au single interface system. Layers 1-12 are Cr, and 13-24 are Au. The pronounced enhancement of the density-of-states in layer 12 reflects the interface resonance. The spin-polarization of the interface resonance is consistent with the fact that $T_{\downarrow} > T_{\uparrow}$ in the transport calculation.

For Cr/Au/Cr trilayers, this spin-filtering implies that the conductance is maximum when the facing layers of the antiferromagnet have the same spin-orientation, *i.e.* the P configuration has a higher conductance, even without any non-local coherence effects. This effect is absent in the single-band models that we studied earlier.

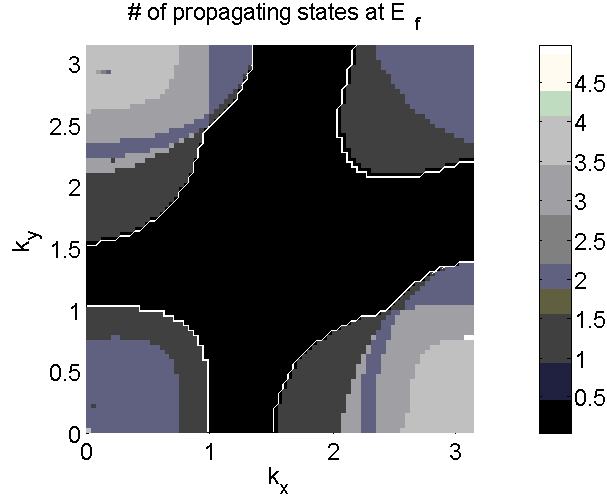


Figure 8.6: Number of propagating states in the [001] direction at the Fermi energy for bulk antiferromagnetic Cr.

To explore the origin of the spin-dependent interface resistance in greater detail, we have examined the layer and k_{\parallel} resolved local density of states of the single-interface calculation (here k_{\parallel} refers to the transverse momentum label). Fig. (8.5) shows the layer-resolved results. (In the calculation, the first 12 layers on each side of the interface are allowed to differ from the bulk. In Fig. (8.5) layers 1-12 are the Cr layers in the scattering region near the interface while layers 13-24 are the Au layers in the scattering region.) We see that there is a pronounced interface resonance on the last Cr layer; this is a consequence of the difference between the Fermi surface topologies of Cr and Au. Moreover, this state is spin polarized, with direction opposite to that of the bulk local moment. Fig. (8.6) shows the number

of propagating channels in the Brillouin zone for Cr, which demonstrates that the Fermi surface of Cr differs strongly from the nearly spherical Fermi surface of Au. In particular, there are large regions in the Brillouin zone of Cr in which there is no propagating state, whereas Au has propagating states across all of the central region of the transverse Brillouin zone. Fig. (8.7) shows the transverse wavevector-resolved Fermi-level local density of states for layers 8, 10, 12 (the last Cr layer), and 16. Layer 8 is typical of bulk Cr, while layer 16 is typical of bulk Au. Layer 12, however, shows features of both materials; in particular, populations of states within the region of the Cr Brillouin zone with no propagating modes are responsible for the localized interface resonance. Fig. (8.8) shows the total local-density of states as a function of energy for layers near the interface. The rapid relaxation toward bulk values away from the the interface is apparent. The interface layer has a highly distorted density of states function, a high density of states at the Fermi level, and a higher moment density which is responsible for a net ferromagnetic moment [114] contribution from the interface region. Apparently interruption of antiferromagnetic order both narrows the majority-spin bands and lowers the energy of minority spins in this interface layer. Hopping of down-spins from the sub-interface layer on which they are the majority to the spacer layer is enhanced by the minority spin interface resonance.

The enhanced moment density in the interface layer is accompanied by more attractive spin-up potentials on this layer and spin-dependent bonding across the Cr/Au interface. The effective hopping matrix elements across the interface have a spin-dependent contribution that is about 1% of their total values. In order to determine whether it is spin-dependent hopping or resonances related to spin-dependent site energies, we have symmetrized hopping of the interface to remove its spin dependence, and re-calculated the conductance. We find the same value for the current polarization, indicating that it is the interface resonance that is

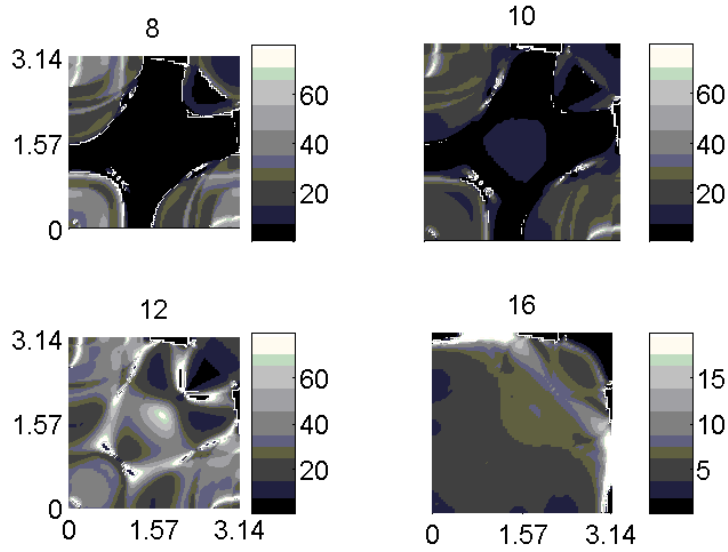


Figure 8.7: Number of propagating states in the [001] direction at the Fermi energy for bulk antiferromagnetic Cr.

largely responsible for the polarization. The fact that the GMR is due to interface resonances, rather than to phase-coherent multiple-scattering across the spacer layer, suggests that the effect will be robust at elevated temperatures.

As mentioned in Sec. (8.3), the antiferromagnet/normal interface resistance is not spin-dependent in the toy model systems. The key property of the toy model which leads to this spin-independent interface resistance is that each antiferromagnetic unit cell is invariant under a combination of space and spin inversion. The ab-initio mean-field Hamiltonian does not have this property. A spin-dependent resistance will occur in the toy model when either the hopping amplitude from spacer to the top antiferromagnetic layer is made spin-dependent or the exchange-splitting in the top layer is shifted from its bulk value. In this sense the interface resonance, while not directly responsible for transport, indirectly enables spin dependent transmission.

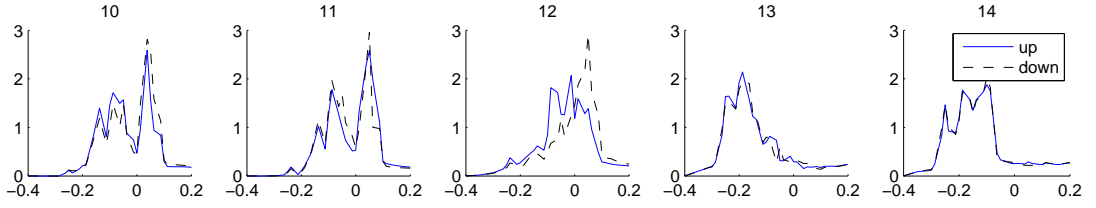


Figure 8.8: Density of states at the Fermi energy in the Brillouin zone for layers 10-14 of the single interface Cr-Au system. The DOS relaxes to its bulk shape a couple of layers away from the interface..

8.4.3 CIT in Cr-Au

We have evaluated the current induced torques for a system with a four Au monolayer spacer. The angle between the staggered moments of the Cr leads was initialized to 90° : the staggered magnetization is along the \hat{z} direction in the Cr layers to the left of the spacer and along the $-\hat{x}$ direction in the Cr layers to the right. A self-consistent non-collinear solution to the Kohn-Sham equations was obtained with this configuration. The resulting layer resolved torques, evaluated as described in Sec. 6.6, are plotted in Fig. (8.9). For this data, electron flow is from right to left lead. We find strong torques peaked in the first Cr layer, in contrast to the toy model case in which the torques were constant in magnitude and alternated in direction from layer to layer.

For the torques in Fig. (8.9), the antiferromagnetic order parameters of the two layers would rotate together in a pinwheel fashion, much as in the case of standard spin torques in ferromagnets. If the right lead's order parameter were pinned in some fashion (for example by exchange coupling the layer to a ferromagnet), then for electron flow from right to left lead, the direction of the left lead's interfacial layer will tend to anti-align with that of the right lead's interfacial layer. This is consistent with a negative spin polarization induced by the interfacial resonance states found in the single interface calculation.

To shed light on the origin of the new antiferromagnet current-induced-torque physics revealed by these ab-initio calculations we focus on differences between the toy-model case, in which analytic calculations are possible, and the realistic Au/Cr case. Because the equilibrium torques that impose the antiferromagnetic order will always be much stronger than the current-induced torques, we are mainly interested in the sum of the layer resolved torques which drives the antiferromagnetic order parameter and therefore competes only with anisotropy torques. The perfectly staggered torque obtained in the toy model case arises from an out-of-plane current-induced spin density that is spatially constant within each antiferromagnet. (Here in-plane refers to the plane spanned by the orientations of the two antiferromagnetic layers and out-of-plane refers to the perpendicular direction, the \hat{y} -direction in our case.) The constant out-of-plane current-induced spin density in the toy model can be partially explained by the fact that Bloch wave vectors of up and down spin states are not spin-split in antiferromagnets. It follows that a linear combination of transmitted up and down spins have a transverse spin density that is position-independent. (In contrast to the ferromagnetic case, in which the transverse spin density of a particular channel shows spatial oscillations with a period given by $(k_{\uparrow} - k_{\downarrow})^{-1}$) [89].

To see where this physics breaks down in our calculation, consider Fig. (8.6), which shows that a particular transverse channel has 1-4 possible values of k_z . For those channels with a single k_z value at the Fermi energy, we find that the contribution to the transverse spin density is spatially constant. Evidently the toy model does a good job of describing this type of transverse channel, suggesting that our earlier conclusion that there is a bulk contribution to the staggered spin-torque in an antiferromagnet does have general validity. The present calculations emphasize, however, that there is also an interface contribution coming dominantly from channels with more than one k_z value at the Fermi energy. In this case the transmitted

wave function is a linear combination of states with different k_z values. These states interfere with each other to produce an oscillating transverse spin density. Summing over many channels with different oscillation periods of the transverse spin density leads to a rapid decay of the transverse spin density, exactly as in the case for ferromagnets [89]. A material with a simpler, single valued Fermi surface would not have this interface contribution to the total staggered torque. The complex Fermi surface is necessary to stabilize the AFM order via nesting in the first place, however. In our case, the interface torque dominates the total staggered torque. It is nevertheless substantial, totalling $.049 \mu_B/e$.

To estimate the critical current for switching the antiferromagnetic order parameter, we take the anisotropy of bulk Cr with spins pointing along the \mathbf{n} direction as:

$$E(\mathbf{n}) = K_1(\hat{\mathbf{z}} \cdot \mathbf{n})^2 + 4K_2(\hat{\mathbf{x}} \cdot \mathbf{n})^2(\hat{\mathbf{y}} \cdot \mathbf{n})^2 \quad (8.5)$$

where [119] $K_1 = 10^3 \text{ J m}^{-3}$, and $K_2 = 10 \text{ J m}^{-3}$, and take the magnetic damping parameter to be $\alpha = 0.1$ [119]. Here K_1 is positive for $T > T_{sf} = 123.5K$, and \mathbf{Q} , the spin density wave vector, is taken to be in the z-direction. Near the fixed point, $\mathbf{n} = \hat{\mathbf{x}}$, the damping torque per area is then $\Gamma = \alpha\gamma(K_1 + 4K_2)t$, where t is the thickness of the layer. (Note that antiferromagnets possess no demagnetizing field, so that the anisotropy does not include shape anisotropy and is due only to magnetocrystalline anisotropy.) The current required to have the current-induced-torque overcome damping is therefore $.049(\mu_b/e)\Gamma \approx 6.3 \cdot 10^{18}t(A/m^3)$. (In this we assume that the transfer torque efficiency calculated at $\theta = 90^\circ$ is the same as that for small or large angle.) Typical values for critical current densities in ferromagnets are up to 100 times larger, primarily because of the large demagnetizing fields present in ferromagnets. We therefore expect that it will be possible to achieve current induced switching in a circuit containing only antiferromagnetic elements.

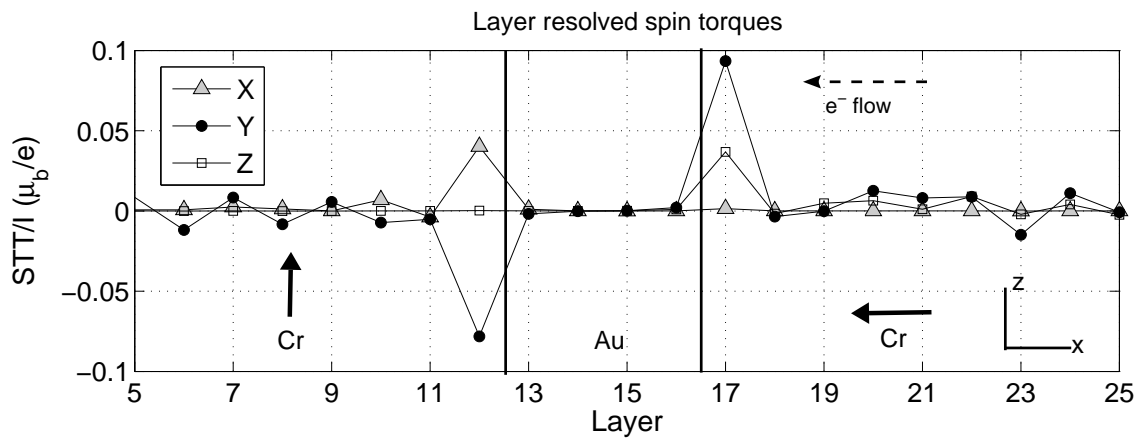


Figure 8.9: Layer resolved current induced torque per current. The (X,Y,Z) directions in the legend refer to the directions of the induced torques. The solid arrows in the figure refer to the orientation of the Cr interface spin. The torque is localized in the first layer of the Cr.

Chapter 9

Spin Torques Between FM and AFM layers.

9.1 Introduction

In the previous chapters, we considered the torques present in spin valve structures with two FM or two AFM layers separated by a nonmagnetic spacer. We next consider a hybrid system with a FM layer adjacent to an AFM layer. As discussed in Sec. (2.5), this configuration is used in applications for shifting the hysteresis loop of the FM via the exchange bias effect. There is experimental evidence consistent with the notion that spin torques at an AFM-FM interface may effect exchange bias [120], motivating the present study.

Another important aspect of this system is that the AFM layer adjacent to the interface is compensated, or has 0 net spin. This also distinguishes the present calculation from that of the previous chapter, in that the SDW vector \mathbf{Q} is perpendicular to the current (whereas the previous chapter considered \mathbf{Q} parallel to current). We will see that this configurations highlights the qualitative distinctions of spin transfer torques in AFM versus conventional FM STT.

The specific choice of materials in our calculation is the antiferromagnetic alloy NiMn and ferromagnetic Co. We describe the equilibrium properties of this system in Sec. (9.2.1). In Sec. (9.2.2), we discuss the spin transfer torques that occur - the STT are of a qualitatively different character than in conventional FM STT. Whereas conventional STT varies as $\sin \theta$, where θ is the angle between layer orientations, we find a torque with $\sin 2\theta$ dependence. In Sec. (9.3), we explore general implications of this new form of spin torque. We find very unusual qualitative features for the behavior of a ferromagnetic layer under this torque, including the stabilization of the ferromagnetic orientation out of the easy plane, and stabilization of ferromagnetic orientation opposite the applied field direction. Sec. (9.4) considers the effect of torque on the switching field of FM layer in exchange bias the AFM-FM system.

9.2 NiMn-Co – Equilibrium properties

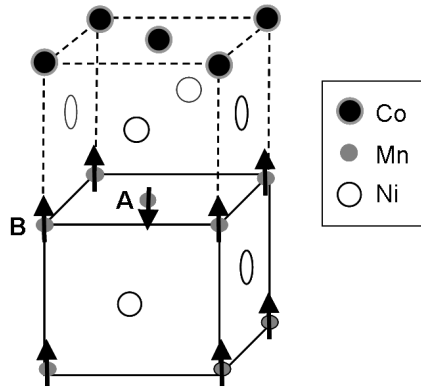


Figure 9.1: Coordinates and spin structure for Co-NiMn interface.

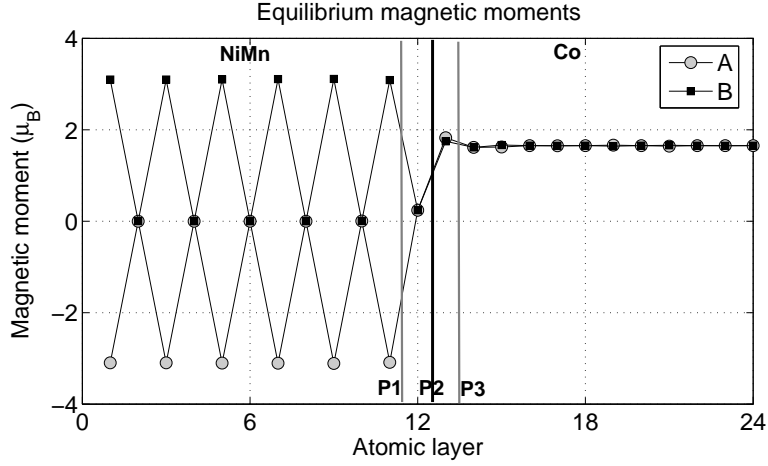


Figure 9.2: Magnetic moment on each sublattice. Layer 12 is terminating Ni layer of NiMn. The vertical lines labelled “A, B, and C” represent choices of planes which subdivide the system, as explained in the text.

9.2.1 General properties

The materials used in this study are antiferromagnetic NiMn and ferromagnetic Co. The structure of the interface is shown in Fig. (9.1). This system has been studied before in the context of calculating exchange interactions and their effect on the magnitude of exchange bias [121]. The crystal structure of NiMn is face centered tetragonal in which the Ni and Mn layers alternate in the (001) direction [97]. In our calculation, we use $a = 3.697 \text{ \AA}$, with c/a ratio of 0.9573. Following Ref. [121], we use a crystal structure of Co that matches with NiMn, with c/a ratio taken to conserve the experimental atomic volume of hexagonal Co. The interface with the Co is in the (001) direction, and in our calculation the NiMn terminates with a Ni layer. The Ni atoms are approximately nonmagnetic, while the Mn atoms form a compensated antiferromagnetic 2-dimensional lattice within each plane. We label the two oppositely oriented sublattices *A* and *B* (see Fig. (9.1)). Fig. (9.2) shows the resulting layer-resolved magnetic moment for each sublattice. (Here layers \leq

12 are NiMn, with odd layers Mn, and even layers Ni, and layers ≥ 13 are Co.) The magnetic moment on Mn atoms is approximately $3.1 \mu_B$ ¹, consistent with the previous result in Ref. [121] of $3.2 \mu_B$, both of which are smaller than the experimental value of $3.8 \mu_B$ [97]. The Co moment is $1.65 \mu_B$, and the terminating Ni layer acquires a small net moment of $0.24 \mu_B$.

9.2.2 Spin transfer torques in AFM-FM system

To find the spin torques in the system, it is necessary to introduce non-collinearity between the FM and AFM layers. To do so, we choose a plane and rotate the magnetic orientation on one side of the plane, leaving the other side's magnetization fixed. The choices of plane we use are shown in Fig. (9.2), and are labelled P1, P2, and P3 (for rotating layers ≥ 12 , 13, and 14, respectively). Unless otherwise explicitly stated, results shown are for choice P2, in which all of the Co layers are rotated and all NiMn layers kept fixed. With a rotated magnetic configuration, we find the spin torques present in the nonequilibrium systems as in the previous two chapters.

As in previous systems, exchange interactions between magnetic moments are dominant, so that the order parameter is driven coherently by current-induced torques. Because the AFM layers consist of a staggered spin configuration, its order parameter is rotated by torques which differ by a sign on the 2 sublattices (see Fig. (9.3)).

Fig. (9.4) shows the total torques on the AFM and FM layers vs. angle. We define the θ as the angle between the FM orientation and the z -axis. There is a dramatic difference from the standard ferromagnetic spin torque case: usually the spin torques goes as $\sin \theta$, whereas here there is an approximately $\sin 2\theta$ behavior.

¹Apparently the larger electronegativity of Ni results in a full shell for Ni (8→10). The loss of 2 electrons in the Mn shell (7→5) results in a magnetic moment of about 3 for Mn, according to Hund's rules

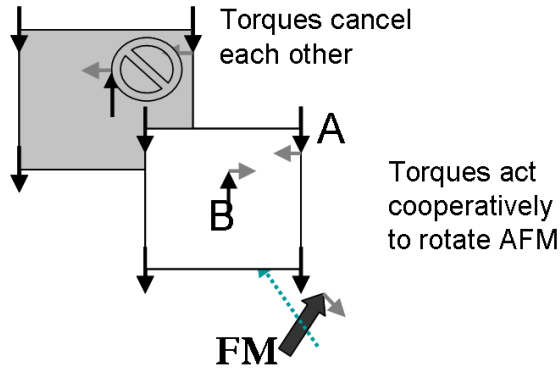


Figure 9.3: Illustration of the need for torques to differ by sign on the A and B sublattices in order to rotate the AFM moment. The torques are shown with gray arrows. For current from FM to AFM, the torque pulls the AFM axis toward the FM, and the FM perpendicular to the AFM axis.

The physical picture of these torques is that for electrons flowing from FM to AFM, the torque tends to align the axis of AFM with the FM orientation, while for electron flow from AFM to FM, the torques tend to make the AFM axis perpendicular to the FM, within their common plane (shown in Fig. (9.3)).

The existence of these torques (at least on the FM) and their form can be anticipated on general grounds. For the collinear configuration, the spin polarization is nonzero: $P = (G_{\uparrow} - G_{\downarrow}) / (G_{\uparrow} + G_{\downarrow}) = 6.4\%$. Not surprisingly, spins parallel with the FM transmit more easily. A spin-polarized current in collinear magnetic systems generally implies the presence of spin transfer torques on ferromagnetic layers when the system deviates slightly from collinearity. Fig. (9.5 (a)) shows the direction of this spin torque on the FM for small θ . By symmetry, the current is completely aligned with the FM for $\theta = 90^\circ$, therefore the spin torque vanishes.² For $\theta > 90^\circ$, the spin-polarization and resulting spin transfer torque changes sign, as shown in

²The non-vanishing numerical value for torque at $\theta = 90^\circ$ is due to the fact that the interface Ni layer has a small net uniform moment.

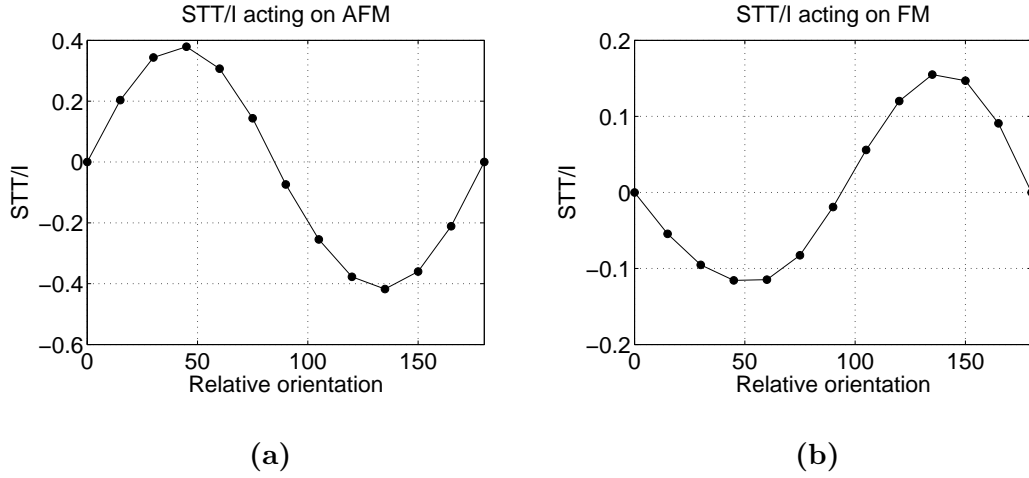


Figure 9.4: Spin torque per current on FM and AFM layers for compensated interface.

in Fig. (9.5 (c)). Therefore the torque on the FM must behave approximately as $\sin 2\theta$.

This general argument rests on the notion of spin torques arising from spin currents. For the AFM layer, this notion is no longer useful: the net spin of a single AFM layer is 0, and we will see in the following data that the AFM order parameter in a layer is only driven for vanishing net spin flux.

Fig. (9.2.2) shows the layer resolved torques on sublattices A and B for several different relative layer orientations. There is a trend in which the sublattices in the AFM layer closest to the FM (layer 11) experience an approximately equal and opposite torque, while the subsequent Mn layer (layer 9) sublattices experience approximately the same torque. In Fig. (9.7), we plot the torques acting on the sublattices in these first two Mn layers vs. angle. The net torques act on the first layer, and approximately cancel on subsequent layers. The torque from an individual transverse channel does not show this generic property or trend; it is only observed after averaging over the Fermi surface. It remains unclear to what extent this trend is an accident, or the result of something more fundamental.

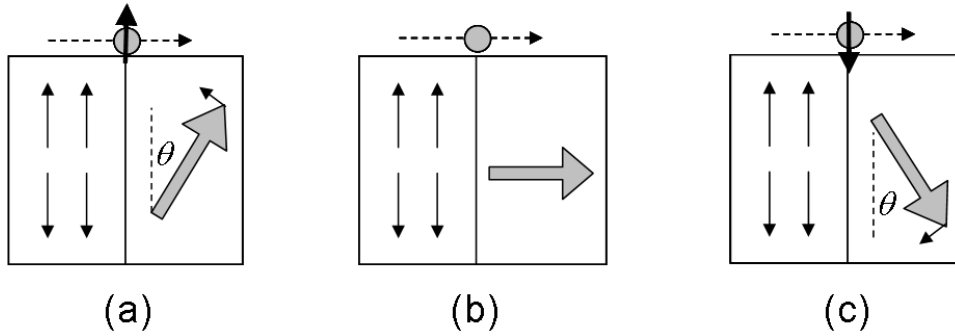


Figure 9.5: Cartoon showing the spin transfer torques present in a compensated AFM - FM interface. (a) The presence of the ferromagnet leads to spin-polarized current and STT for small θ . (b) At $\theta = 90^\circ$, the current's spin polarization is due only to the FM, as seen from symmetry considerations, and there is no torque. (c) For $\theta > 90^\circ$, the sign of current polarization and spin transfer torque changes.

The spin torques on the AFM operate in an entirely distinct manner from the conventional FM case. We find vanishing net spin flux into the first Mn layer, yet a nonzero spin torque. On the other hand, there is a net spin current flux into the second Mn layer, yet exchange interactions lead to a vanishing spin torque. Here the perspective of torques arising from instantaneous misalignment of the magnetization with the current-induced exchange-correlation field is especially useful.

In Fig. (9.8) we show the torques present on the FM and AFM layer for different choices of system division. The labelling P1, P2, and P3 are denoted in Fig. (9.2), and correspond to rotating the magnetization for layers ≥ 13 , 14, and 15, respectively. For cuts P1 and P2, the surface between the two rotated layers is compensated, and both cases reveal a $\sin 2\theta$ behavior. On the other hand, for cut P3 the surface layer is a uniformly magnetized Co layer - an uncompensated interface. Here the torque on the FM is more $\sin\theta$ -like. As a general rule then, it seems as though the extent of compensation on the interface is correlated with the $\sin 2\theta$ nature of the spin torque.

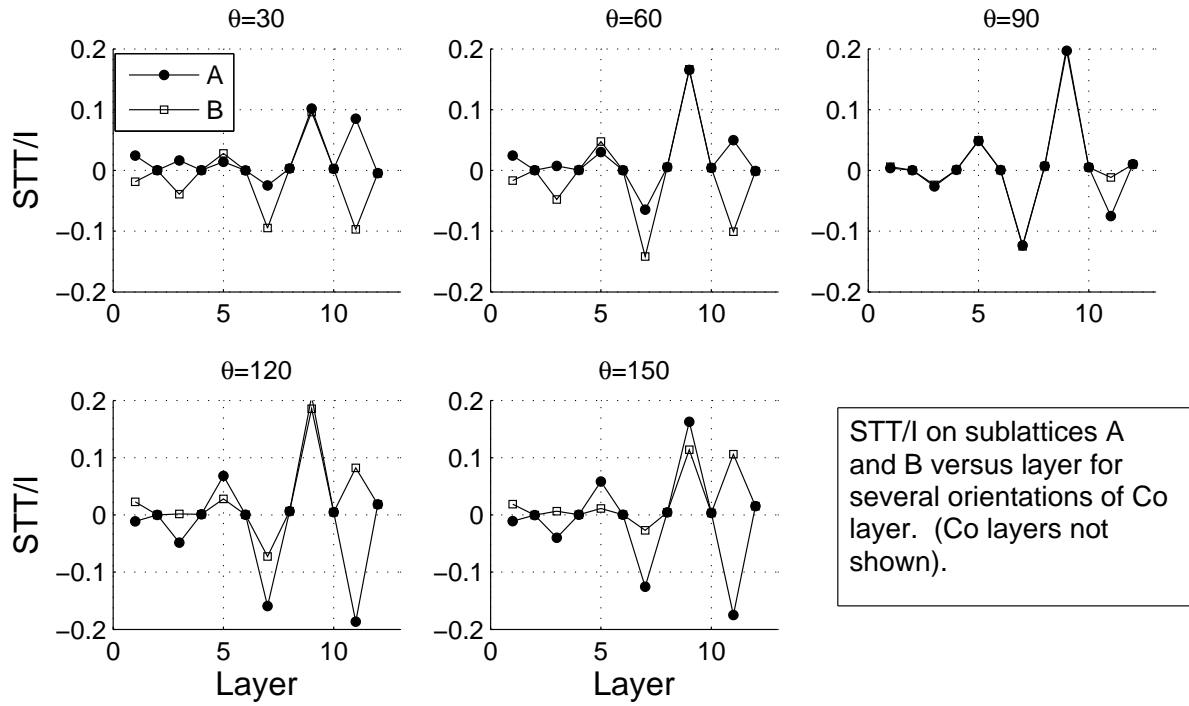


Figure 9.6: Torques on sublattices A and B vs. layer, for several different relative orientations.

9.3 Effect of $\sin 2\theta$ torque in single domain magnetics

Now we consider the implications of this qualitatively different form of the spin transfer torque for the stability and dynamics of a magnetic layer. Here we suppose the AFM layer is fixed with axis in the \mathbf{n}_2 direction, and consider how the orientation of a FM layer \mathbf{n}_1 evolves with time. Noting that $\sin 2\theta = 2 \cos \theta \sin \theta$, the current induced torque calculated in the previous section takes the following form (omitting

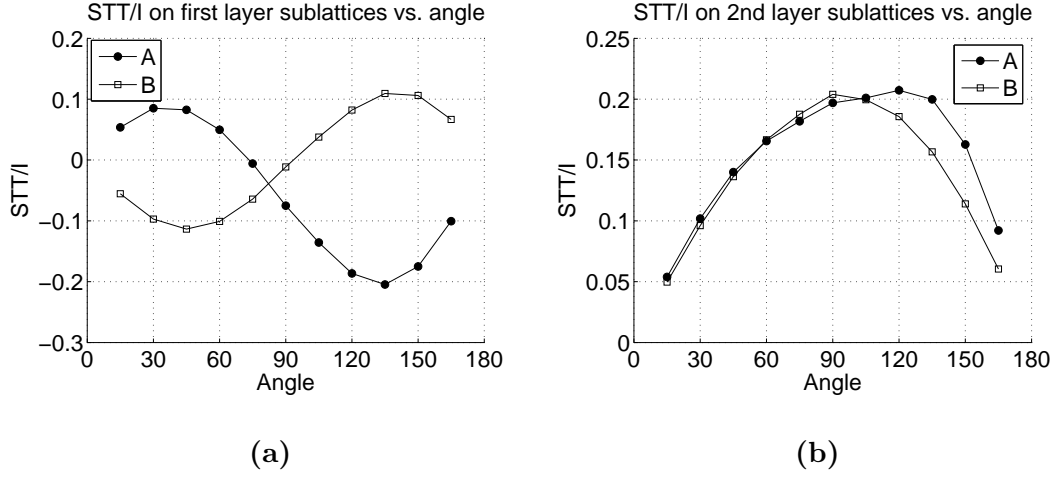


Figure 9.7: Torques on the first two layers of Mn. On the first layer, the torques cooperate, while on the second layer, they cancel each other.

some constant prefactors)³:

$$\Gamma_{\text{STT}} = 2gI \cos \theta (\mathbf{n}_1 \times \mathbf{n}_2 \times \mathbf{n}_1). \quad (9.1)$$

We are interested in exploring the dynamics that follow from such a torque. The phase diagram of stability and dynamical modes of the LL equation + Slonczewski torque is well studied analytically [122] and numerically [123, 124], and we discuss this standard phase diagram in following section (Sec. (9.4)). Our attempt here is to perform a similar type of analytic and numerical analysis for the current induced torque described above, of $\sin 2\theta$ type.

The system we have in mind is slightly different than the AFM-FM system of the previous section. It is shown in Fig. (9.9), and has a spacer layer to remove the complicated and largely unknown direct exchange interactions between the AFM and FM. The FM possesses a hard axis from shape anisotropy, and is subject to an

³There is also an in-plane torque which follows a $\sin \theta$ behavior, however its impact on the following discussion is not significant.

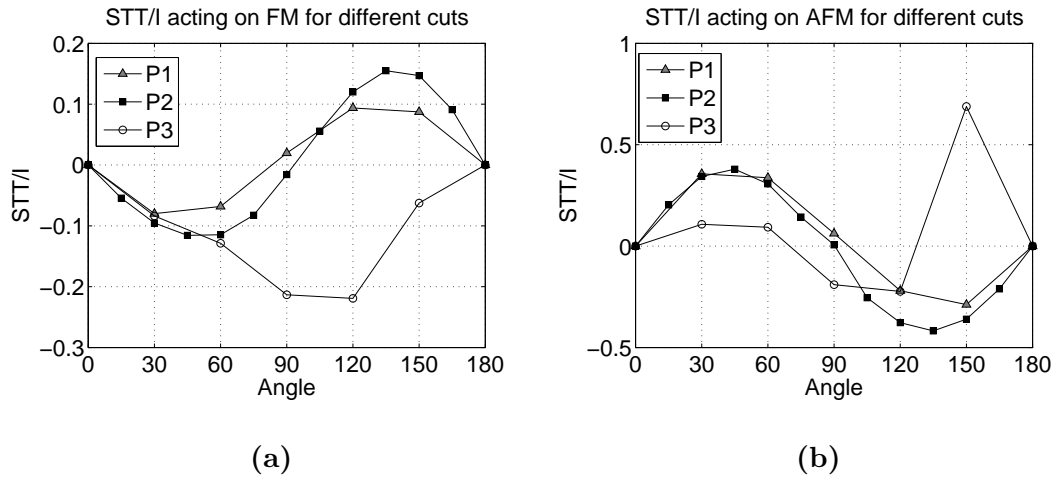


Figure 9.8: Torques vs. angle on FM and AFM layer for different choices of system cuts. An interface with compensated moment (cuts A and B) shows a $\sin 2\theta$ behavior, while an interface with uncompensated moment (cut C) shows a more $\sin \theta$ behavior.

applied field and spin torques of the form $\sin 2\theta$. We omit easy-axis anisotropy - its inclusion doesn't substantially change the picture described below. We suppose that the AFM orientation is fixed.

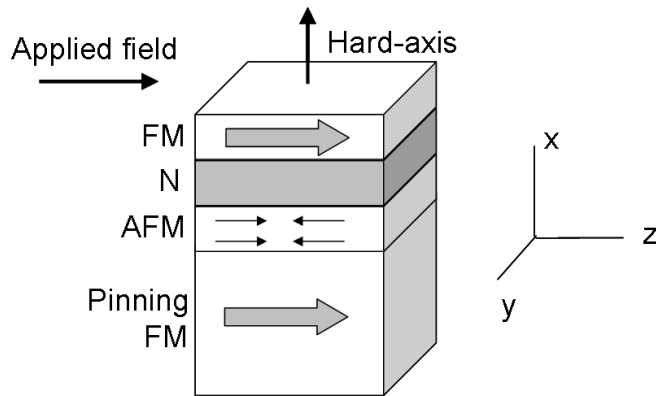


Figure 9.9: System to consider the implications of $\sin 2\theta$ torque. The field and AFM axis point in the \hat{z} -direction, and the hard axis is in the \hat{x} -direction.

Landau Lifshitz equation and dimensionless units

To integrate the Landau-Lifshitz numerically, we use a dimensionless time variable $\tau = \gamma\mu_0 M_s t$, where γ and M_s denote the gyromagnetic ratio and saturation magnetization, respectively. In these units, the applied field H is scaled by the demagnetization field $H_d = \mu_0 M_s$, and we denote the dimensionless applied field by $h_{app} = H/\mu_0 M_s$. For typical ferromagnets such as Co, $\mu_0 M_s \sim 1$ T, so the value of dimensionless applied field nearly corresponds to its dimensionful value in Tesla.

The form of spin torque in the Landau Lifshitz equation is

$$|\Gamma_{STT}| = \frac{gJ\mu_B}{M_s\ell e} \sin 2\theta \equiv H_{st}, \quad (9.2)$$

where J is current density, ℓ is the FM layer thickness, e is electron charge, and g is the spin transfer efficiency. The form of this prefactor is explained in Sec. (6.3). Fig. (9.4) shows that $g \sim 0.1$ for the FM. The dimensionless spin torque is also scaled by $\mu_0 M_s$, and if we assume a FM thickness of 3 nm and $M_s = 1.3 \cdot 10^6$ A/m, the dimensionless spin transfer torque prefactor, denoted by h_{st} , is proportional to J and is given by:

$$h_{st} \equiv \frac{H_{st}}{\mu_0 M_s} = J (A/m^2) (5.2 \cdot 10^{-15}). \quad (9.3)$$

In the following results, h_{st} varies between ± 0.05 , corresponding to current densities between $\pm 9.6 \times 10^{12} A/m^2$, which is similar to current densities attained in experiments [28]. (The conversion of the dimensionless h_{st} into a real current density for a material with demagnetization field of 1 T is $J = (h_{st}t) \times 3.8 \cdot 10^9 A/cm^2$, where t is the thickness of the FM layer in nm.)

Coordinates for solutions of the Landau Lifshitz equation

Studying the properties of the system analytically is facilitated by a convenient choice of coordinates. For describing motion on a unit sphere, we follow the procedure described in Ref. [122] and use the following coordinate system (Shown in Fig. (9.10)):

$$\begin{aligned} e_\phi &= (-\sin \phi, \cos \phi, 0) ; \\ e_\theta &= (-\cos \theta \cos \phi, -\cos \theta \sin \phi, \sin \theta) . \end{aligned} \quad (9.4)$$

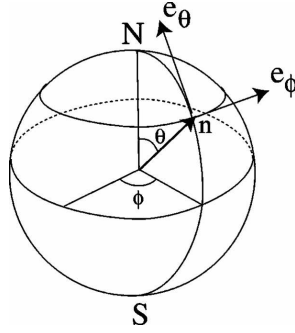


Figure 9.10: Coordinates used for magnetic orientation and torques.

In these coordinates, the Landau-Lifshitz equation takes the form [122]:

$$\begin{pmatrix} \dot{\phi} \\ \dot{\theta} \end{pmatrix} = \frac{1}{1 + \alpha^2} \begin{pmatrix} 1/\sin(\theta) & -\alpha/\sin(\theta) \\ -\alpha & -1 \end{pmatrix} \begin{pmatrix} \Gamma_\phi \\ \Gamma_\theta \end{pmatrix}, \quad (9.5)$$

where the torques are expressed in terms of the ϕ, θ components:

$$\begin{aligned} \Gamma_\phi &= (\mathbf{\Gamma} \cdot e_\phi) ; \\ \Gamma_\theta &= (\mathbf{\Gamma} \cdot e_\theta). \end{aligned} \quad (9.6)$$

The Cartesian form of the current induced torques, assuming that the AFM layers is pinned in the \hat{z} direction, is given by:

$$\begin{aligned}\mathbf{\Gamma}_{\text{STT}} &= H_{st} (-n_x n_z^2, -n_y n_z^2, (1 - n_z^2) n_z) \\ &= H_{st} (-\sin \theta \cos \phi \cos^2 \theta, -\sin \theta \sin \phi \cos^2 \theta, \sin^2 \theta \cos \theta).\end{aligned}\quad (9.7)$$

The physical picture of this form of the torque is that for negative current ($H_{st} < 0$), the torque tends to align the magnetization perpendicular to \hat{z} , while for positive current, the torque tries to align the magnetization with \hat{z} .

For the particular case considered here, we also include the demag field $H_d = \mu_0 M_s$, which acts as a hard axis in the \hat{x} direction ($\mathbf{H}_d = -|H_d| n_x$), and an applied field H which points in the \hat{z} direction. These torques then take the Cartesian form:

$$\mathbf{H} = (-H_d n_x, 0, H); \quad (9.8)$$

$$\begin{aligned}\Rightarrow \mathbf{\Gamma}_{\text{tot}} &= (-H n_y, H n_x + H_d n_x n_z, -H_d n_x n_z) + \mathbf{\Gamma}_{\text{STT}} \\ &= (-H \sin \theta \sin \phi, H \sin \theta \cos \phi + H_d \sin \theta \sin \phi \cos \theta, \\ &\quad -H_d \sin \theta \cos \phi \cos \theta) + \mathbf{\Gamma}_{\text{STT}}.\end{aligned}\quad (9.9)$$

Expressing the total torque in the coordinates of Eq. (9.4) results in:

$$\begin{aligned}\Gamma_\theta &= -\frac{1}{2} \sin(\theta) \sin(2\phi) H_d + \sin(2\theta) H_{st}; \\ \Gamma_\phi &= \sin(\theta) H + \frac{1}{2} \sin(2\theta) \cos^2(\phi) H_d.\end{aligned}\quad (9.10)$$

Solutions to Landau Lifshitz equation

Equilibrium points satisfy $\Gamma_\phi = 0$ and $\Gamma_\theta = 0$. Not all equilibrium points are stable; if the magnetization is slightly perturbed from an equilibrium, it is stable only if it decays back into the equilibrium point. The procedure for determining the stability

of an equilibrium point is describe in Appendix D. Here we specify the equilibrium points and their regions of stability. We then verify numerically that these are indeed stable solutions.

Solution 1: We first consider $H_{st} < 0$, or a spin transfer torque that tends to make the FM perpendicular to the AFM axis. An equilibrium point is given by:

$$\begin{aligned}\theta &= \pm \frac{\pi}{2} + \frac{H}{H_d} ; \\ \phi &= \frac{-2HH_{st}}{H_d^2} .\end{aligned}\tag{9.11}$$

This describes a magnetization that points approximately out of the plane. The region of stability for this solution is:

$$H_{st} \leq \frac{\alpha H_d}{2} \left(\frac{2 \cos^2 h - h \sin h}{h \sin h - \cos 2h} \right) .\tag{9.12}$$

The stable solution is possible for only a finite range of applied field, with the asymptotic stable applied field found from Eq. as the solution to

$$h \sin h = 1 - 2 \sin^2 h .\tag{9.13}$$

This has the solution of $h = 0.608$, implying that for applied field greater than $\mu_0 M_s(0.608)$, the out-of-plane configuration is never stable.

Solution 2: The other solution for $H_{st} < 0$ is simply $m_z = \pm \hat{z}$, describing simple alignment of the magnetization with the applied field. The stability of this solution is given by:

$$\begin{aligned}m_z &= \frac{H}{|H|} ; \\ H_{st} &\geq \frac{\alpha}{2} \left(-|H| - \frac{H_d}{2} \right) .\end{aligned}\tag{9.14}$$

Solution 3: We next find solutions for $H_{st} > 0$. For $0 \leq H \leq H_d$, there are configurations in which the magnetization is approximately anti-aligned with the applied field. They are given by:

$$\begin{aligned}\theta &= \cos^{-1}\left(\frac{-H}{H_d}\right); \\ \phi &= \frac{-2H_{st}H}{H_d^2}.\end{aligned}\tag{9.15}$$

These solutions are stable for a range of applied fields and currents:

$$H_{st} \geq -\frac{\alpha H_d}{2} \left(\frac{h^2 - 2}{3h^2 - 1} \right)\tag{9.16}$$

Solution 4: For $H_{st} > 0$ and $H \geq H_d$, the equilibrium solutions consist of $m_z = \pm 1$. The solution and stability condition for the magnetization anti-aligned with the field are:

$$\begin{aligned}m_z &= \frac{-H}{|H|}; \\ H_{st} &\geq \frac{\alpha}{2} \left(|H| - \frac{H_d}{2} \right).\end{aligned}\tag{9.17}$$

Fig. (9.11) shows the x and z components of the magnetization as a function of applied field and current, determined numerically. We have taken the damping $\alpha = .01$, and the applied field and spin transfer torque are scaled by the demagnetization field, as described earlier. Also shown is the magnitude of the power spectrum peak of $z(t)$ (labelled “P_Z”) - a nonzero value indicates a precessing solution. Also shown is the stability boundaries defined by Eqs. (9.12),(9.14),(9.16),(9.17). The numerics verify the stability of the unusual out-of-plane and field-anti-aligned solutions.

We first discuss the physical picture for the stable out-of-plane configuration under negative current. The origin for the instability of the easy-plane configuration

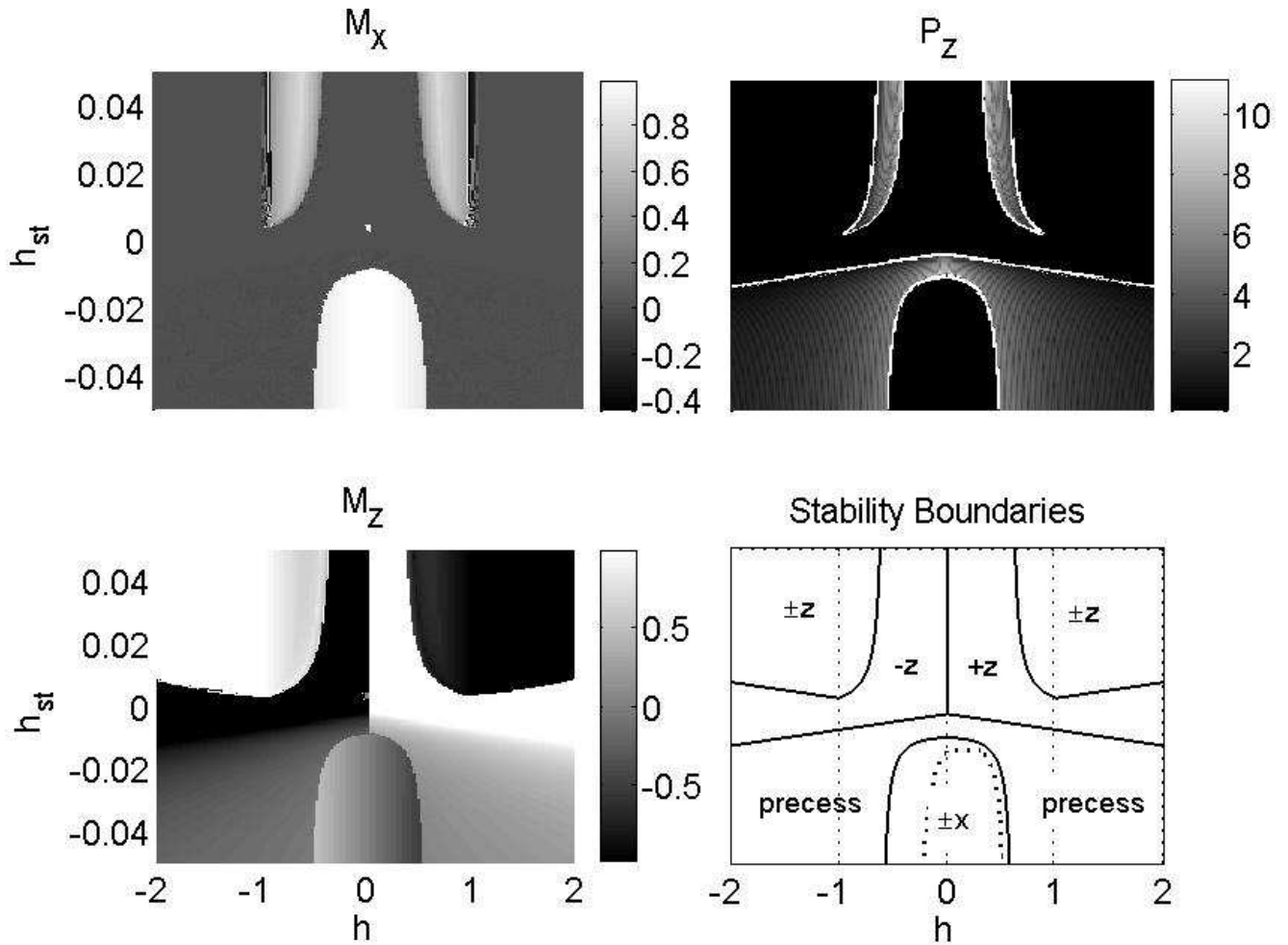


Figure 9.11: Magnetic configuration (M_x, M_z) and peak of power spectrum P_z (arbitrary units) versus applied field and current. Also shown is stability boundaries found analytically (the labels $\pm x, \pm z$ refer also to solutions which point approximately in these directions). The stability boundary plot also shows the reduced out-of-plane solution space for negative to positive field sweep with a dashed line.

can be understood from Fig. (9.12). Here the AFM axis is labelled $\hat{u} = \hat{z}$ and the magnetization is \hat{m} , and we consider small excursion from the plane. For simplicity we first consider no external field. If a small fluctuation drives the magnetization out

of plane, it will precess about the hard axis and eventually damp back into the easy plane. The presence of the $\sin 2\theta$ torque, however, tends to make the magnetization perpendicular to \hat{u} within their common plane. As \hat{m} precesses around the hard-axis, this torque vector has a component Γ_x which points out of the $y - z$ plane. If the angle between \hat{z} and the in-plane component of \hat{m} is β , the magnitude varies as $\Gamma_x = 2H_{st}m_x \sin^2 \beta$, as shown in the figure. The crucial point is that this torque is always positive throughout the precession. When this torque exceeds the damping, the out-of-plane configuration is stabilized. The eventual out-of-plane orientation is $+\hat{x}$ or $-\hat{x}$ depending on the direction of the initial fluctuation out of the plane. The presence of an applied field changes the trajectory of the magnetization upon an excursion from the easy-plane. For a sufficiently large applied field, the torque is unable to stabilize the out-of-plane configuration, and the magnetization undergoes simple precession around the \hat{z} -axis (double check that).

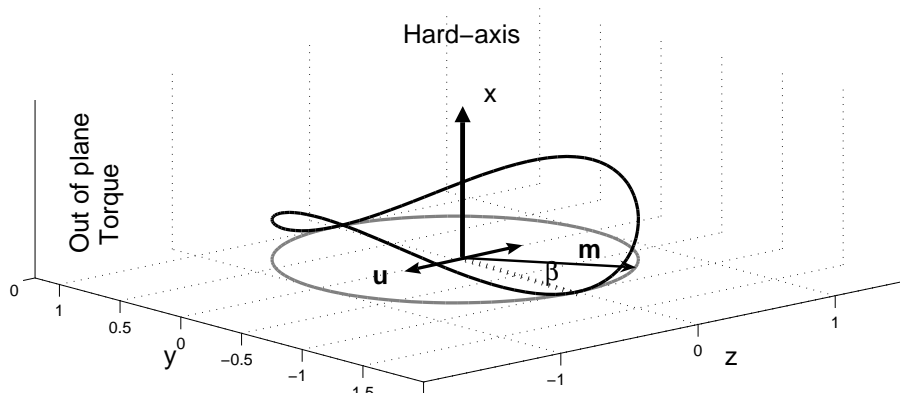


Figure 9.12: Saddle shape shows the out of plane torque vs β for small excursions from the $y - z$ plane. The torque is always positive.

The data for each (h, h_{st}) point of Fig. (9.11) is obtained beginning from an initial condition close to the solution given by Eq. (9.11). These equilibrium solutions are not universal attractors, and are attained for a subset of initial con-

ditions. To see the effect of initial conditions, we have also swept the applied field from negative to positive for each applied current, using the slightly perturbed final coordinates of a trajectory as the initial condition for the next value of applied field. The out-of-plane solution space is reduced, shown by the dotted line in Fig. (9.11) in the stability boundaries plot .

We next consider the physical picture configuration in which magnetization points opposite to the applied field for $H_{st} > 0$. This state only occurs if the magnetization is initially close to anti-aligned to the applied field. The reason for its stability is that this form of the spin torque does not distinguish between $+\hat{z}$ and $-\hat{z}$ - it merely tends to make to direct the FM to the nearest available \hat{z} -axis. The region for such a solution is shown in Fig. (9.11), labelled $\pm z$. It is seen that the applied field must be sufficiently large for this solution to be stabilized. The exact condition for stability is

$$|H| \geq \frac{H_d}{\sqrt{3}} . \quad (9.18)$$

It may be surprising that a sufficiently large field is required to stabilize an anti-aligned configuration. The reason is that for a small applied field, the reversal process consists mostly of a precession about the hard-axis and takes place near the easy plane. This hard-axis-precession-assisted reversal is too strong for the spin torque to inhibit. On the other hand, for large applied field, the precession is mostly around the applied field, and the reversal is due mostly to damping. The spin torque is able to compete with and prevent this damping-dominated reversal process.

To see this state experimentally, it is necessary to initialize the magnetization in a direction nearly anti-aligned to an applied field. One possibility is to initialize the magnetization in the $-\hat{z}$ direction with a negative field, apply a large positive current, and then sweep to a sufficiently large positive field. If the sweeping time is fast enough so that the magnetization remains close to the anti-aligned state, then

the magnetization should remain in the $-\hat{z}$ state. The required sweep rate is on the order of $\gamma\alpha \sim 10^{-10}$ T/s.

Experimental considerations

We now comment on the experimental possibilities of seeing these effects. In the preceding analysis, we assume that the AFM is fixed. This can be accomplished by placing a large FM adjacent to the AFM, so that the AFM is pinned via the exchange bias effect. The presence of this pinning FM may influence the dynamics of the free FM, but its signature should be very distinct from the influence of the AFM layer on the free FM.

We first consider the stabilization of the out-of-plane configuration. A virtue of this effect is that the surface of the AFM need not be single domain for its observation. As long as the magnetization of the AFM is compensated and points in the plane, different orientations of domains at the AFM surface should cooperatively push the FM out of the plane. For the stabilization of the field anti-aligned FM configuration, it is necessary to have a AFM surface with an axis pointing mostly along a single direction. If averaging over domains reduces the average orientation magnitude to f ($f=1$ for single domain, $f=0$ for uniform distribution of domain orientations), the critical field required to stabilize the anti-aligned configuration will increase as approximately $1/f$.

9.4 Effect on switching field

The way in which to incorporate the spin transfer torques present at an AFM-FM interface into a model of FM field driven switching is not clear. We mention here a number of approaches for the sake of comparing to experimental data [120]. The data with which we compare is deceptively simple: the switching field changes linearly with current, for both positive and negative current. We will first consider the effect

of current on a model of exchange bias. Next we consider how a conventional $\sin\theta$ torque acting between a partially compensated AFM and FM changes the switching field of the FM. It turns out that neither mechanism can capture the experimental data, but we include the calculations here for the sake of demonstrating how simple explanations for the effect seem to be deficient.

9.4.1 Effect on exchange bias model

We consider a specific model of exchange bias, and how spin torques change the behavior of the model. The data of Ref. [32] indicate that the origin of exchange bias for IrMn is the presence of pinned moments, as described in Sec. (2.5). The average orientation of the pinned moments determines the unidirectional exchange field. In our model, we suppose that the pinned moment directions are taken from a uniform distribution, with a specified maximum angle, as indicated in Fig. (9.13). The distribution and net moment are therefore parameterized by a single variable β . The average moment for a given β is simply given by:

$$\begin{aligned}\langle m_z \rangle &= \frac{1}{2\beta} \int_{-\beta}^{\beta} \cos\theta d\theta \\ &= \frac{\sin\beta}{\beta}.\end{aligned}\tag{9.19}$$

In this model of exchange bias, the magnitude of exchange bias is proportional to the average of the uncompensated, pinned moments along the bias direction - precisely $\langle m_z \rangle$.

If spin torque acts directly on these pinning moments to change their distribution, the net moment of the AFM layer will change, and the exchange bias will change by the same proportion. We find the effect of spin torques on the distribution in the next section.

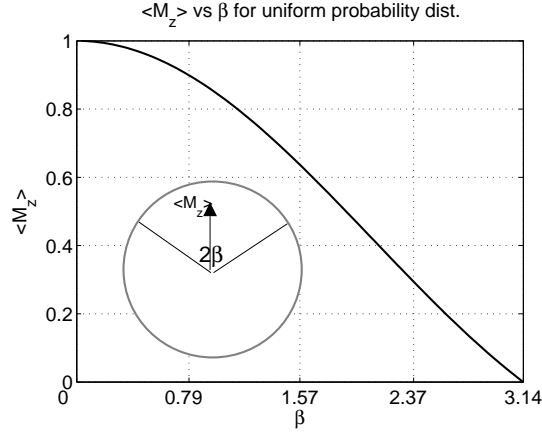


Figure 9.13: For a uniform distribution of spin orientations spanning $\theta \in [-\beta, +\beta]$, the average \hat{z} -component is $(\sin \beta)/\beta$, plotted above.

9.4.2 Effect of current on uniform spin distribution

Using the BJZ coordinate system for an applied field in the $(\sin \xi, 0, \cos \xi)$ direction, the torques are given by:

$$\begin{aligned}\Gamma_\theta &= B \sin \xi \sin \phi + B_{st} \sin \theta ; \\ \Gamma_\phi &= B (\sin \theta \cos \xi - \cos \theta \cos \phi \sin \xi) .\end{aligned}\quad (9.20)$$

The equilibrium points of the above are given by:

$$\begin{aligned}\theta &= \pm \xi ; \\ \phi &= \frac{-B_{st}}{B} .\end{aligned}\quad (9.21)$$

Carrying out the procedure to find the stability of these fixed points as described before results in the stability condition $B_{st} < \frac{\alpha B}{\cos \xi}$. The orientations are therefore

given by:

$$\theta = \begin{cases} \xi & \text{for } B_{st} < \frac{\alpha B}{\cos \xi} \\ -\xi & \text{for } B_{st} > \frac{\alpha B}{\cos \xi} \end{cases} \quad (9.22)$$

The physical picture of the action of STT on a spin with pinning field orientation ξ with respect to the fixed layer is as follows: the STT is most effective for smaller ξ , and when the STT is sufficiently large to overcome damping, it induces a switch to the direction $-\xi$. Fig. (9.14) shows a numerical check of the above solutions for stability. The numerics verify the stability and switching condition of Eq. (9.22).

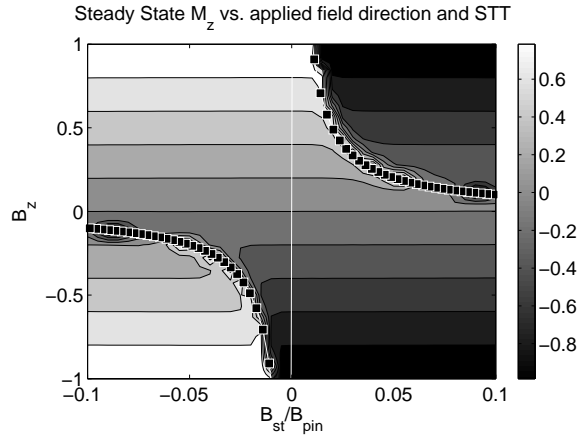


Figure 9.14: Numerical check of the solution to LL+Slonczweski equation with tilted pinning field. The black squares indicate the stability boundary determined analytically.

So for a distribution of spins and a given spin torque B_{st} , only a subset will undergo switching, those that satisfy the condition of Eq. (9.22). This means that

spins will switch if their orientation satisfies the criterion:

$$\xi < \cos^{-1} \left(\frac{\alpha B}{B_{st}} \right) \equiv \xi^* . \quad (9.23)$$

This modifies the distribution, and therefore modifies the average value of m_z . In the formula below, we start with the original averaged m_z , then subtract off the portion of the distribution that has switched, and replace it with its switched value. If we assume $B_{st} > 0$, the modification of the distribution can be understood from Fig. (9.15). The resulting average value of m_z is:

$$\begin{aligned} \langle m_z \rangle &= \frac{\sin \beta}{\beta} - \frac{2}{2\beta} \int_{-\xi^*}^{\xi^*} \cos(\theta) d\theta ; \\ \Rightarrow \langle m_z \rangle &= \begin{cases} \frac{\sin \beta}{\beta} - \frac{2}{\beta} \sqrt{1 - \left(\frac{\alpha B}{B_{st}} \right)^2} & \text{for } \xi^* < \beta \\ -\frac{\sin \beta}{\beta} & \text{for } \xi^* > \beta \end{cases} \end{aligned} \quad (9.24)$$

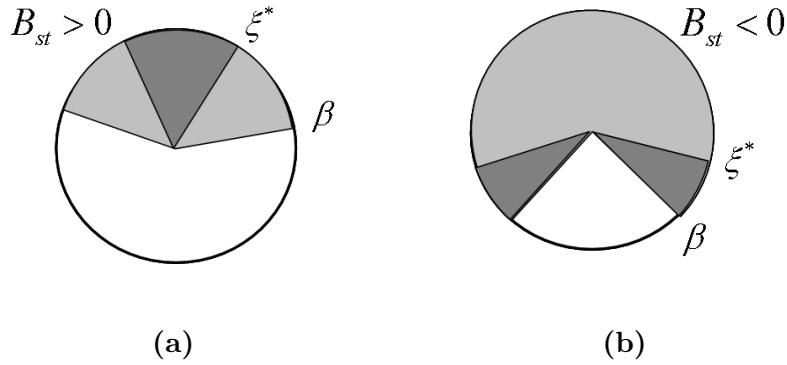


Figure 9.15: (A) Set of switched moments are shown in darker gray for a given distribution and $B_{st} > 0$. (b) Dark gray shows set of switched moments for $B_{st} < 0$; here only moments sufficiently close to $\theta = \pi$ undergo switching.

For $B_{st} < 0$, only moments whose pinning field satisfies $\xi > \pi/2$ switch (again refer to Fig. (9.15)). The condition for switching for these moments is the

$\theta \in [\xi^*, \beta]$. The average then becomes:

$$\begin{aligned} \langle m_z \rangle &= \frac{\sin \beta}{\beta} - \frac{2}{\beta} \int_{\xi^*}^{\beta} \cos(\theta) d\theta \\ &= -\frac{\sin \beta}{\beta} + \frac{2}{\beta} \sqrt{1 - \left(\frac{\alpha B}{B_{st}}\right)^2}. \end{aligned} \quad (9.25)$$

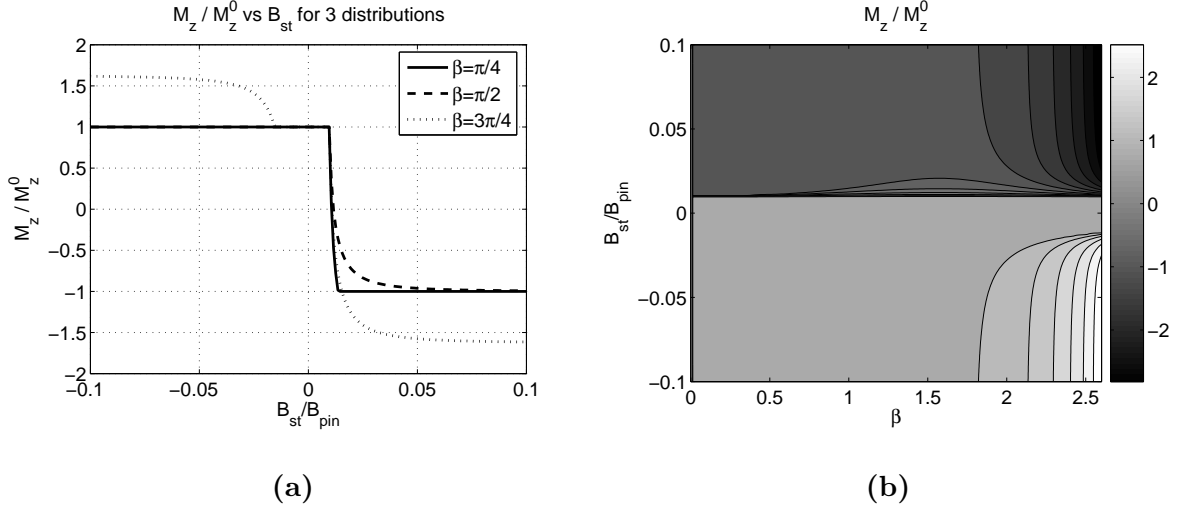


Figure 9.16: (a) Ratio of $\langle M_z \rangle / \langle M_z^0 \rangle$ vs. B_{st} / B_{pin} for 3 moment distributions - a value of +1 signifies no change to exchange bias, and -1 signifies a reversed exchange bias orientation. (b) shows a contour plot of $\langle M_z \rangle / \langle M_z^0 \rangle$ vs B_{st} / B_{pin} and β .

Fig. (9.16 (a)) shows the average value of M_z for various distributions and applied currents. There is a threshold current of $B_{st} > \alpha B_{pin}$ for any modification of M_z to occur. For $\beta < \pi/2$, a negative current does not affect the distribution at all. For B_{st} slightly greater than αB_{pin} , the average orientation of M_z changes sign, which would result in a reversal of the exchange bias field. This is not at all seen experimentally, indicating that this is not a good model for the experimental results.

9.4.3 Direct torque on FM

We now consider effect on the switching field of a ferromagnet from a conventional spin transfer torque. When the ferromagnet possesses only uniaxial anisotropy, the switching field is easily obtained:

$$B_{sw} = \pm K + \frac{B_{st}}{\alpha} . \quad (9.26)$$

However, the addition of easy-plane anisotropy complicates the (I,B) phase diagram. This has been studied in detail analytically and numerically, and there is very good agreement between experimental and theoretical results. We include numerical results of our own for the sake of contrasting to the phase diagram of the $\sin 2\theta$ case and for comparing to experimental data for current modulated switching field. Fig. (9.11) shows the M_z component of the magnetization versus applied field and current, for both forward and backward applied field sweeps. In this calculation, there is a uniaxial anisotropy of .01, so that for $B_{st} = 0$, there is hysteresis between the two field sweeps. The current affects the switching field only above a critical current $B_{st} > \alpha H_d/2$, and for only one sign of the current. This is due to the known, and curious fact that spin transfer torque is able to assist the magnetization from escaping a local minimum and therefore reduce the switching field; however it does not retard the escape process, and so does not increase the switching field. This is shown schematically in Fig. (9.18).

Fig. (9.19) shows the resulting hysteretic magnetization loops for several applied currents. This plot emphasizes the fact the spin transfer torque shifts only one of the switching branches, in accord with the previous discussion.

For this reason, a simple spin transfer interaction between the AFM and FM is unable to explain the data of Ref. [120], because in the data, the switching field of both branches is shifted, and the switching field of 1 branch changes for both

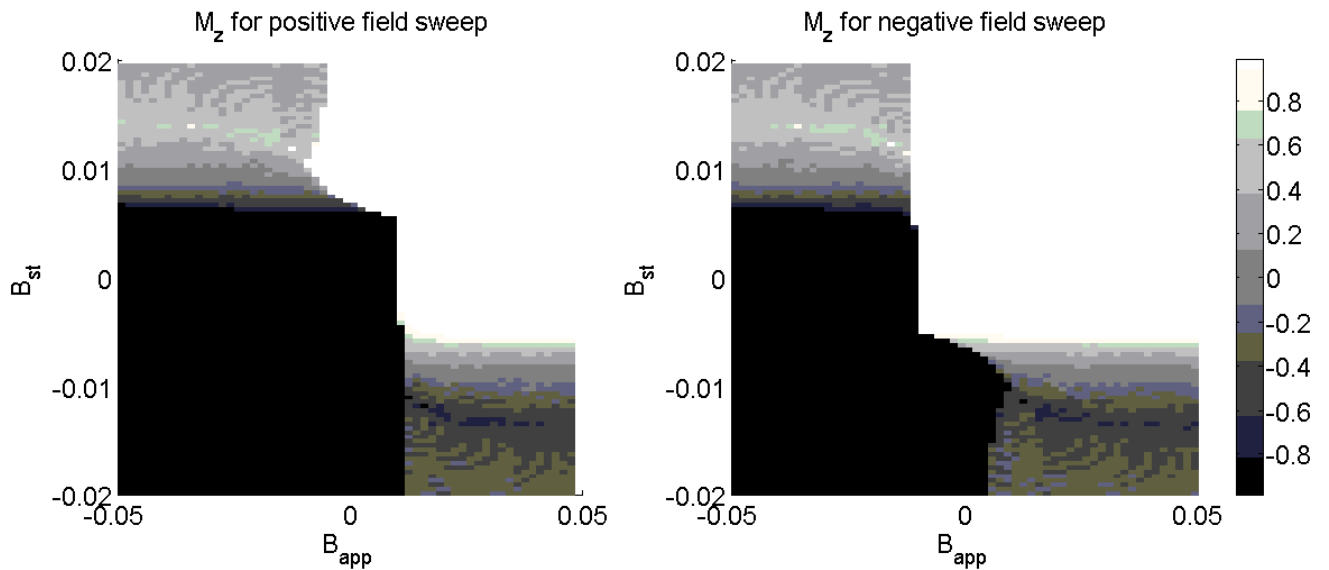


Figure 9.17: M_z vs applied field and current, for forward and backward field sweeps.

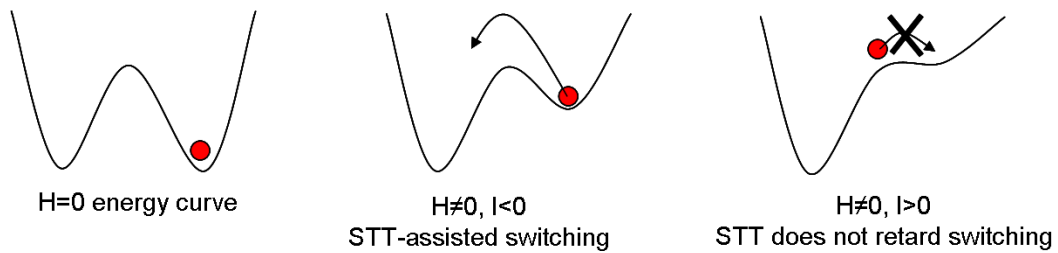


Figure 9.18: Illustration of the role of STT for field-induced magnetization switching of an easy plane FM: STT can assist the switching, reducing the switching field; however STT can not retard switching.

positive and negative current.

Clearly then more refined models of the exchange interaction between the AFM and FM, and the effect of STT on this interaction are needed in moving forward. This likely represents a difficult line of work, as exchange bias interactions are very complicated and still the subject of much debate [125].

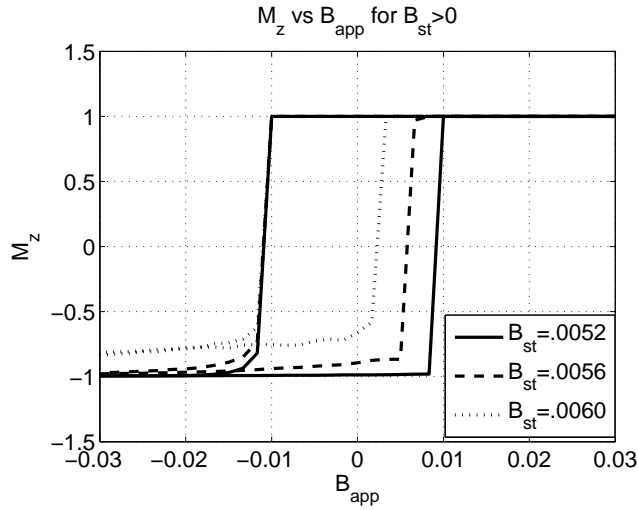


Figure 9.19: Hysteresis loops for several values of spin transfer torque. Only 1 branch is shifted by the spin transfer torque.

9.5 AGMR in compensated AFM systems

In this section we briefly review some results for a system composed of two compensated antiferromagnets NiMn, separated by a Cu spacer. The system geometry consists of NiMn layers, each of which terminates with the antiferromagnetic, compensated Mn layer, with 6 ML of Cu atoms in between. The 2d lattice of the facing Mn layers are offset from each other, as shown in Fig. (9.20). As before, the collinear self-consistent ground state is obtained, and one of the layers magnetic orientation is rotated. Subsequently the transmission is calculated.

Fig. (9.21) shows the transmission versus θ . ($\theta = 0$ corresponds to the spin lattice structure shown in Fig. (9.20)). There is a striking behavior, in which the transmission is lowest, and approximately equal for $\theta = 0, 90, 180$. The data is likely fit to a function of the form $T(\theta) = |\sin(2\theta)|$. For both $\theta = 0, 180$, the current is unpolarized, $T_{\uparrow} = T_{\downarrow}$. We suspect that the difference in conductance as the relative orientation is varied is due to phase coherent effects, as in the toy model

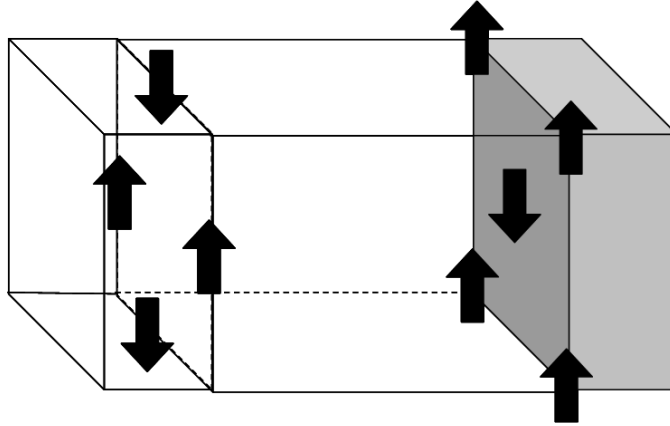


Figure 9.20: The lattice structure of the NiMn-Cu-NiMn system. There are 6 ML of Cu (atoms not shown explicitly), and the terminating Mn layers 2d lattices are offset in real space, as shown.

of AGMR present in the last chapter. It is not known if the angular dependence is a generic properties of compensated antiferromagnets, and it is also not clear if the fact that the transmission is minimized for collinear and perpendicular orientations is general. It is the suspicion of this author that the angular behavior is generic within a phase coherent regime, and that the location of transmission minima/maxima is not general, but model specific. These constitute important issues for further study.

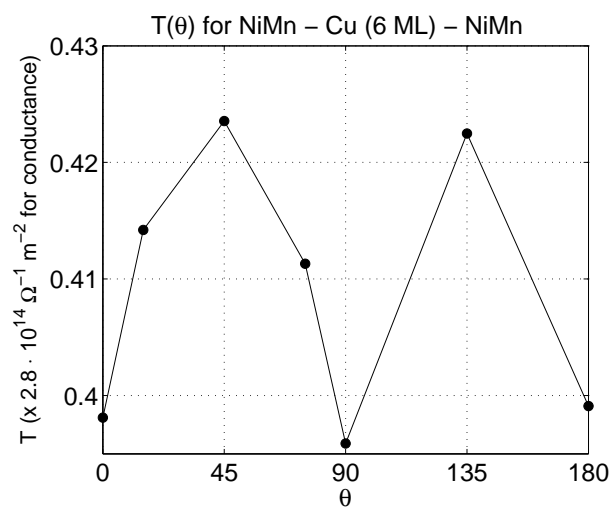


Figure 9.21: Conductance vs. relative orientation for two compensated antiferromagnets. The conductance is minimized (or resistance maximized) for $\theta = 0, 90, 180$. The difference in conductance is likely due to phase-coherent effects.

Chapter 10

Conclusion.

In this thesis, we implemented a general formulation of current induced torques into a NEGF+DFT code. With this, we found the torques present in realistic structures containing both FM and AFM materials. This is the first direct calculation of current induced torques from first principles. We found that spin transfer torques exist in AFM, and are qualitatively different than in FM. We predict a new phase diagram for the magnetic configuration versus applied field and current for a AFM-FM hybrid structure.

The current induced torque is derived from the misalignment between nonequilibrium quasiparticle spin and the local magnetic condensate. This formulation does not rely on conservation of spin angular momentum arguments, and is therefore applicable to antiferromagnets and materials with strong spin-orbit coupling. There are a number of future directions that this work can go. Here we describe some of them:

1. The effect of current on exchange bias can be studied in more detail. There are a number of fairly complex models of exchange bias, which rely on domain structure of the antiferromagnet interface [126]. It is possible that the effect of spin transfer on exchange bias is only properly understood in the context of these more

elaborate models.

2. We found that the application of a bias voltage can induce magnetization dynamics when a circuit contains noncollinear magnetic configurations. That leads to the question as to whether a bias voltage change other properties of the magnetization besides its direction? For example, can it change the transition temperature [127]? The exchange calculator enables us to do this calculation. Usually exchange is found from change in energy upon small rotation, but we find it as a torque. This brings up the deeper question of the role of the equilibrium quantity energy in nonequilibrium situations [128].

3. Another type of system to consider carefully is one in which spin is not conserved, specifically a system with strong spin orbit coupling. We have implemented spin orbit coupling into our code following Ref. [129], and so we can find the torques present in such a system. One potentially enlightening route is define a *total* angular momentum current and see if torques from nonequilibrium spin densities correspond to net angular momentum flux [130].

4. Finally, the NEGF formalism is highly flexible, and can accurately model molecular systems. This brings up the obvious question as to whether or not spin transfer torques would be manifest in magnetic molecules. Magnetic molecules are a rich subject matter in their own right. If a magnetic molecule were sandwiched between leads with noncollinear magnetization, certainly one would expect some measure of spin transfer torque to be exerted on the molecule's magnetization. It is possible that this torque will have unique features because of the reduced dimensionality of the molecular system. Recall that the standard picture of spin torque relies on the decay of spin torques away from the interface, which in turn relied on the interference of many transverse channels' spin densities. With a 1-d or 0-d system, such interference will not occur, so that qualitatively different physics may emerge in such systems. The most experimentally viable choice of molecule to study

is an important consideration in moving forward on this topic.

Appendix A

Exchange-Correlation Parameterizations

For the LSDA exchange-correlation functional, we have implemented that of Perdew and Zunger, described in Ref. [70]. Here we give its details. The potential is written in terms of the total density n and polarization ζ :

$$n = (4\pi r_s^3/3)^{-1} \tag{A.1}$$

$$\zeta = (n_\uparrow - n_\downarrow)/n \tag{A.2}$$

The form of the exchange-correlation potential is:

$$v_{xc}^\uparrow = - \left(\frac{6n_\uparrow}{\pi} \right)^{1/3} + \mu_c + f(\zeta)(\mu_c^P - \mu_c^U) + (\epsilon_c^P - \epsilon_c^U)(1 - \zeta) \frac{df}{d\zeta} \tag{A.3}$$

$$v_{xc}^\downarrow = - \left(\frac{6n_\downarrow}{\pi} \right)^{1/3} + \mu_c + f(\zeta)(\mu_c^P - \mu_c^U) + (\epsilon_c^P - \epsilon_c^U)(1 - \zeta) \frac{df}{d\zeta} \tag{A.4}$$

Where f is

$$f(\zeta) = \frac{(1+\zeta)^{4/3} + (1-\zeta)^{4/3} - 2}{2^{4/3} - 2} \quad (\text{A.5})$$

The expressions for the correlation contribution to the potential are:

$$\epsilon_c(r_s, \zeta) = \epsilon_c^U(r_s) + f(\zeta) [\epsilon_c^P(r_s) - \epsilon_c^U(r_s)], \quad (\text{A.6})$$

$$\begin{aligned} \mu_c^\sigma(r_s, \zeta) = & \mu_c^U(r_s) + f(\zeta) [\mu_c^P(r_s) - \mu_c^U(r_s)] + \\ & [\epsilon_c^P(r_s) - \epsilon_c^U(r_s)] [\text{sgn}(\sigma) - \zeta] \frac{df}{f\zeta} \end{aligned} \quad (\text{A.7})$$

The parameters appearing in the Eq. (A.7) and (A.7) are given below. The superscript i runs over U and P :

$$\epsilon_c^i = \gamma_i / (1 + \beta_1^i \sqrt{r_s} |\beta_2^i r_s|) \quad (\text{A.8})$$

$$\mu_c^i = \left(1 - \frac{r_s}{3} \frac{d}{dr_s}\right) \epsilon_c^i = \epsilon_c^i \frac{(1 + \frac{7}{8} \beta_1^i \sqrt{r_s} + \frac{4}{3} \beta_2^i r_s)}{(1 + \beta_1^i \sqrt{r_s} + \beta_2^i r_s)} \quad (\text{A.9})$$

$$\epsilon_c^i = A_i \ln r_s + B_i + C_i r_s \ln r_s + D_i r_s \quad (\text{A.10})$$

$$\mu_c^i = A_i \ln r_s + (B_i - \frac{1}{3} A_i) + \frac{2}{3} C_i r_s \ln r_s + \frac{1}{3} (2D_i - C_i) r_s. \quad (\text{A.11})$$

$A_{U,P}$ and $B_{U,P}$ are constants:

$$A_U = 0.0311$$

$$B_U = -0.048$$

$$A_P = 0.01555$$

$$B_P = -0.0269 \quad (\text{A.12})$$

Appendix B

Derivations for equilibrium and nonequilibrium spin torques

B.1 Exchange parameters from energy and torques.

Here we prove that the expression for exchange parameters found in Ref. [83] is identical to the expression for the torque associated with a non-self-consistent $[H, \rho]$ pair. We start with a collinear ground state:

$$\rho_0 = \frac{1}{2}(\rho^0 + m\tau_z) \quad (\text{B.1})$$

$$H_0 = H^0 + \frac{1}{2}\Delta\tau_z \quad (\text{B.2})$$

We now rotate some portion of the magnetization by an angle θ , which gives a new Hamiltonian H_1 :

$$\begin{aligned} H_1 &= H_0 + \delta H \\ \delta H &= \frac{\Delta}{2} ((1 - \cos(\theta))\tau_z + \sin(\theta)\tau_x). \end{aligned} \quad (\text{B.3})$$

Now we would like to find the instantaneous resulting spin density. This is found from the new density matrix ρ_1 :

$$\rho_1 = \frac{1}{\pi} \int \text{Im} \left(\frac{1}{E^{(+)} - H_1} \right) dE \quad (\text{B.4})$$

Considering only the integrand $G(E) = (E^{(+)} - H_1)^{-1}$. We can find an approximate expression for G by expanding to second order in θ :

$$G_1(E) = (E - H_0 - \delta H)^{-1} \quad (\text{B.5})$$

$$G_1(E) = G_0 (1 - \delta H G_0)^{-1} \approx G_0 (1 + \delta H G_0 + (\delta H G_0)^2) \quad (\text{B.6})$$

Eq. (B.6) determines the instantaneous spin density in the presence of the perturbed magnetization configuration described by Eq. (B.3). The resulting torque is then

$$\mathbf{\Gamma} = \mathbf{\Delta}_1 \times \mathbf{m}_1 \quad (\text{B.7})$$

$$\Rightarrow \Gamma^y = \Delta_1^x m_1^z - \Delta_1^z m_1^x \quad (\text{B.8})$$

$$= \frac{\Delta \sin(\theta)}{32} \{ 8m + 6m^2 \Delta + 3m^3 \Delta^2 - 2\Delta G_0^2 - 4m^2 \Delta (1 + m\Delta) \cos(\theta) + m^3 \Delta^2 \cos(2\theta) \} \quad (\text{B.9})$$

This has the form $\sin(\theta)$ as expected. Dividing the sin factor, and taking the limit of $\theta \rightarrow 0$

$$\Gamma^y / \sin(\theta) = \frac{\Delta}{16} (m(4 + m\Delta) - \Delta G_0^2) \quad (\text{B.10})$$

Finally, making the replacement $G_0 = G_\uparrow + G_\downarrow$, $m = G_\uparrow - G_\downarrow$, and including the integral over energy gives:

$$\frac{\Gamma^y}{\sin(\theta)} = \frac{1}{4\pi} \int \text{Im} (\Delta(G_\downarrow - G_\uparrow) + \Delta G_\uparrow \Delta G_\downarrow) dE \quad (\text{B.11})$$

This reproduces the result of Leichtenstein for the stiffness. This verifies that our approach for calculating stiffness from instantaneous torques is equivalent to calculating $\partial E/\partial \mathbf{m}$ directly.

B.2 Spin current operator

Here we give a derivation of Eq. (6.38), which relates the spin current flux to magnetization precession around nonequilibrium spin density.

$$\begin{aligned}\rho_{i'i;s's} &= \frac{1}{2}[\rho_{i'i}^{(0)}\delta_{s's} + \vec{m}_{i'i} \cdot \vec{\tau}_{s's}]. \\ H_{i'i;s's} &= H_{i'i}^{(0)}\delta_{s's} - \frac{1}{2}\vec{\Delta}_{i'i} \cdot \vec{\tau}_{s's}.\end{aligned}\tag{B.12}$$

In the 2x2 submatrix which is diagonal in orbital space (or the on-site term), the prefactors of the pauli matrices are real. (Physically these prefactors are related to the spin polarization of the orbital and the effective magnetic field for ρ and H , respectively.) For 2x2 submatrices off-diagonal in orbital index, the prefactors (such as $\rho^{(0)}$ and \vec{m}) are complex. Any hermitian matrix may be decomposed in the manner above. We are ultimately interesting in spin current. To find the expression for the spin current operator, we consider the following:

$$\dot{\rho} = \frac{1}{i\hbar}[H, \rho]\tag{B.13}$$

$$\dot{s}^i = \text{Tr}[\rho H \tilde{\sigma}^i - H \rho \tilde{\sigma}^i]\tag{B.14}$$

Where the trace is in spin space. Using the following:

$$[\sigma^i, \sigma^j] = i\epsilon_{i,j,k}\sigma^k \quad (\text{B.15})$$

$$\{\sigma^i, \sigma^j\} = \delta_{ij} \quad (\text{B.16})$$

$$\sigma^{i2} = 1 \quad (\text{B.17})$$

$$\sigma^{i3} \sim \sigma^i \quad (\text{B.18})$$

$$\text{Tr}[\sigma^i] = 0 \quad (\text{B.19})$$

Considering only the cross term of B.14 with both spin-dependent contributions (\vec{m} and $\vec{\Delta}$), and taking the z-component of the spin time derivative:

$$\text{Tr}[(\tilde{\mathbf{m}} \cdot \tilde{\boldsymbol{\tau}})(\tilde{\Delta} \cdot \boldsymbol{\tau})\sigma^z - (\tilde{\Delta} \cdot \boldsymbol{\tau})(\tilde{\mathbf{m}} \cdot \tilde{\boldsymbol{\tau}})\sigma^z] \quad (\text{B.20})$$

In each of the above, if the z-component of one of $\vec{m}, \vec{\Delta}$ is taken, and the other component is taken to be $j \neq z$, one is left with $\text{Tr}[\sigma_j] = 0$ (from B.17). If both components of $\vec{m}, \vec{\Delta}$ are z, then left over is $\text{Tr}[\sigma_z] = 0$. Hence only the following terms contribute:

$$[(m^x \Delta^y)_{ii} + (m^y \Delta^x)_{ii} - (\Delta^y m^x)_{ii} - (\Delta^x m^y)_{ii}]i(\sigma^z)^2 \quad (\text{B.21})$$

Implicit in the above is an orthogonal basis set (in saying that the density present on site i is ρ_{ii}). Rewriting the above, and including the trace and $1/i\hbar$ prefactor from Eq. (B.14):

$$\frac{1}{4\hbar} \text{Tr} \left[\sum_j (m_{ij}^x \Delta_{ji}^y - m_{ij}^y \Delta_{ji}^x + \Delta_{ij}^y m_{ji}^x - \Delta_{ij}^x m_{ji}^y) \right] \quad (\text{B.22})$$

Now consider the cross terms in which only one factor is spin-dependent, and again restricting attention on the z-component (for example: $\text{Tr}[(\tilde{\mathbf{m}} \cdot \tilde{\boldsymbol{\tau}})\text{H} -$

$H(\tilde{\mathbf{m}} \cdot \tilde{\boldsymbol{\tau}}\sigma_z]$). The only component of \vec{m} that survives the trace over $(\vec{m}\sigma_z)$ is the z -component (since $\sigma_z^2 = 1$). Hence the relevant terms are as follows:

$$\frac{1}{2i\hbar} \text{Tr} \left[\sum_j [\mathbf{H}_{ij}^{(0)} m_{ji}^z - m_{ij}^z \mathbf{H}_{ji}^{(0)} + \Delta_{ij}^z \rho_{ji}^{(0)} - \rho_{ij}^{(0)} \Delta_{ji}^z] \right]$$

Clearly cross terms with both spin-independent factors will vanish under the trace. Thus, combining the two nonzero factors, one obtains:

$$\begin{aligned} \dot{S}_i^z = \text{Tr} \left[\frac{1}{2i\hbar} \sum_j [\mathbf{H}_{ij}^{(0)} m_{ji}^z - m_{ij}^z \mathbf{H}_{ji}^{(0)} + \Delta_{ij}^z \rho_{ji}^{(0)} - \rho_{ij}^{(0)} \Delta_{ji}^z] + \right. \\ \left. \frac{1}{4\hbar} \sum_j (m_{ij}^x \Delta_{ji}^y - m_{ij}^y \Delta_{ji}^x + \Delta_{ij}^y m_{ji}^x - \Delta_{ij}^x m_{ji}^y) \right] \quad (\text{B.23}) \end{aligned}$$

Extending the expression to other vector components may be done simply by cyclic permutation of indices.

B.2.1 Spin-dependent hopping

In the charge current, it makes no difference if you consider the current flowing from site i to $i + 1$ versus the current flowing from $i + 1$ to site i . They are equivalent, with only a minus sign difference. It turns out when you have non-collinear spin current, and spin-dependent hopping, the two are not quite equivalent. The difference between the two is very small, so for practical purposes, they may as well be the same. However, for completeness let me explain the origin of the difference. In the following, I'll have a convention where “ I_L ” refers to where the source is to the left of the target, and “ I_R ” refers to the opposite case (the source to right of the target). For normal charge current, and collinear spin current, the label of source and target is arbitrary, and normally the current calculated by “ I_L ” and “ I_R ” are the same, with only a sign difference. When one has spin-dependent hopping, “ I_L ”

and “ I_R ” may differ. This is shown explicitly in the following calculation for general hopping between 2 sites 1 and 2:

$$I_L : \rho_{12}H_{21} - H_{12}\rho_{21} \quad (\text{B.24})$$

$$I_R : \rho_{21}H_{12} - H_{21}\rho_{12} \quad (\text{B.25})$$

where, as above, $H_{12} = H_{12}^{(0)} + \vec{\Delta}_{12} \cdot \vec{\tau}$, where $H_{12}^{(0)}, \vec{\Delta}_{12}$ are complex, and $H_{21} = H_{12}^\dagger, \vec{\Delta}_{21} = \vec{\Delta}_{12}^\dagger$. Computing the above two expressions for spin current, one finds, and condensing notation into $\rho_{12} = \rho + \vec{\rho}, \rho_{21} = \rho^* + \vec{\rho}^*$ (and using $(\vec{m} \cdot \vec{\tau})(\vec{s} \cdot \vec{\tau}) = (\vec{m} \cdot \vec{s}) + i\vec{\tau} \cdot (\vec{m} \times \vec{s})$):

$$\vec{I}_L = \rho H^* + (\vec{\rho} \cdot \vec{H}^*) + i\vec{\tau}(\vec{\rho} \times \vec{H}^*) + \rho(\vec{H}^* \cdot \vec{\tau}) + H^*(\vec{\rho} \cdot \vec{\tau}) \quad (\text{B.26})$$

$$- [H\rho^* + (\vec{H} \cdot \vec{\rho}^*) + i\vec{\tau} \cdot (\vec{H} \times \vec{\rho}^*) + H(\vec{\rho}^* \cdot \vec{\tau}) + \rho^*(\vec{H} \cdot \vec{\tau})]$$

$$\vec{I}_R = \rho^* H + (\vec{\rho}^* \cdot \vec{H}) + i\vec{\tau}(\vec{\rho}^* \times \vec{H}) + \rho^*(\vec{H} \cdot \vec{\tau}) + H(\vec{\rho}^* \cdot \vec{\tau}) \quad (\text{B.27})$$

$$- [H^*\rho + (\vec{H}^* \cdot \vec{\rho}) + i\vec{\tau} \cdot (\vec{H}^* \times \vec{\rho}) + H^*(\vec{\rho} \cdot \vec{\tau}) + \rho(\vec{H}^* \cdot \vec{\tau})]$$

We find that:

$$\vec{I}_L + \vec{I}_R = 2i\vec{\tau} \cdot [(\vec{\rho} \times \vec{H}^*) - (\vec{H} \times \vec{\rho}^*)] = 4\text{Im}[\vec{\tau} \cdot (\vec{H}^* \times \vec{\rho})] \quad (\text{B.28})$$

Clearly the expected identity $I_L = -I_R$ holds for collinear, or spin-independent hopping (or current). The inequality in the case of noncollinear and spin-dependent hopping can be understood in the following intuitive sense (...). It should be noted, however, that this contribution to the net current is very small compared to the other contributions (even after summing over thousands of transverse channels) - so it has been checked (*at least in my Co-Cu baseline system*) that ignoring the distinction between “L” and “R” leads to no practical consequence. The physical

origin of the difference can be understood intuitively with the cartoons shown below:

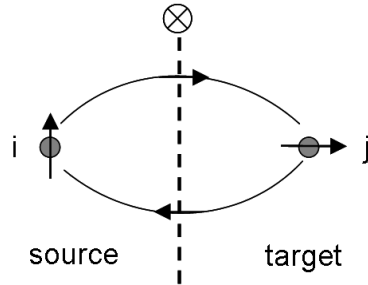


Figure B.1: Spin-dependent noncollinear hopping between two sites i and $i + 1$. The spin is rotated by the “hopping” effective magnetic field (points into the page).

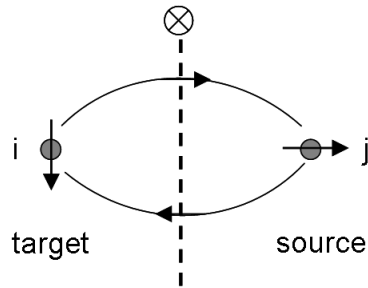


Figure B.2: Spin-dependent noncollinear hopping between two sites i and $i + 1$. When you reverse the labels of “source” and “target”, the sign of the current changes, but in this case, the sense of rotation of the spin changes as well. This is the source of the violation of $I_L = -I_R$. The difference is usually very small.

Appendix C

Toy scattering formulation

Schrödinger's equation with scattering boundary conditions can be solved for toy models with the following scheme. The Hamiltonian is given by

$$\begin{aligned} \mathcal{H}_k &= -t \sum_{\langle i,j \rangle, \sigma} c_{k,i,\sigma}^\dagger c_{k,j,\sigma} + \text{h.c.} \\ &+ \sum_{i,\sigma,\sigma'} \left[(\epsilon_i + \epsilon_k) \delta_{\sigma,\sigma'} - \Delta_i \hat{\Omega}_i \cdot \vec{\tau}_{\sigma,\sigma'} \right] c_{k,i,\sigma}^\dagger c_{k,i,\sigma'} . \end{aligned} \quad (\text{C.1})$$

Here, k denotes the transverse wave number, t the hopping amplitude and ϵ_k the transverse kinetic energy. For simplicity in illustrating the method, we take $\Delta_i = 0$. The boundary condition is an outgoing Bloch state.

$$c_n = e^{ikn} \quad (\text{C.2})$$

$$c_{n-1} = e^{ik(n-1)} \quad (\text{C.3})$$

The wave function is then defined, and can be constructed directly from a real-space representation of the Schrödinger equation:

$$c_i = \frac{c_{i+1}}{t} (E - U_{i+1}) - c_{i+2} \quad (\text{C.4})$$

$$c_1 = \tilde{R}e^{-ik} + \tilde{I}e^{ik} \quad (\text{C.5})$$

$$c_2 = \tilde{R}e^{-2ik} + \tilde{I}e^{2ik} \quad (\text{C.6})$$

Given the wave function at points 1 and 2, Eqs. (C.5) and (C.6) can be easily solved for \tilde{I}, \tilde{R} . This determines the reflection and transmission amplitude.

$$t = \frac{1}{\tilde{I}} \quad (\text{C.7})$$

$$r = \frac{\tilde{R}}{\tilde{I}} \quad (\text{C.8})$$

To consider systems with antiferromagnetic leads, it is necessary to project the asymptotic wave function on to the Bloch state of a antiferromagnet. If the unit cell of an antiferromagnet is given as:

$$H_{\pm}^k = \begin{pmatrix} \pm U & t(1 + e^{2ik}) \\ t(1 + e^{-2ik}) & \mp U \end{pmatrix} \quad (\text{C.9})$$

The \pm subscript refers to up and down spin. The eigenvectors are given in terms of

a basis with labels $|1\rangle, |2\rangle$ (see Fig. (C.1):

$$u_{\pm}^E = \frac{\pm u - \sqrt{u^2 + (2t \cos(k))^2}}{t(1 + e^{2ik})} \quad (\text{C.10})$$

$$u^O = 1 \quad (\text{C.11})$$

$$\begin{pmatrix} \psi_{\uparrow} \\ \psi_{\downarrow} \end{pmatrix} = A \begin{pmatrix} u^O|1\rangle + u_{+}^E|2\rangle \\ u^O|1\rangle + u_{-}^E|2\rangle \end{pmatrix} \quad (\text{C.12})$$

Where the factor A ensures a normalized wave function.

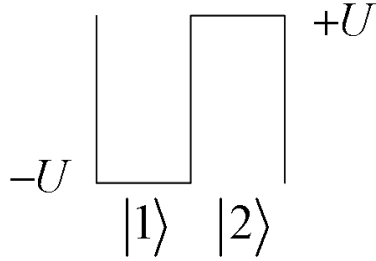


Figure C.1: Unit cell of antiferromagnet (shown for up spin, the down spin has opposite signs for U .)

Appendix D

Stability analysis of Landau Lifshitz equation

In spherical coordinates, the Landau-Lifshitz equation takes the form [122]:

$$\begin{pmatrix} \dot{\phi} \\ \dot{\theta} \end{pmatrix} = \frac{1}{1 + \alpha^2} \begin{pmatrix} 1/\sin(\theta) & -\alpha/\sin(\theta) \\ -\alpha & -1 \end{pmatrix} \begin{pmatrix} \Gamma_\phi \\ \Gamma_\theta \end{pmatrix}, \quad (\text{D.1})$$

where the torques are expressed in terms of the ϕ, θ components:

$$\begin{aligned} \Gamma_\phi &= (\mathbf{\Gamma} \cdot \mathbf{e}_\phi); \\ \Gamma_\theta &= (\mathbf{\Gamma} \cdot \mathbf{e}_\theta). \end{aligned} \quad (\text{D.2})$$

Equilibrium points satisfy $\Gamma_\phi = 0$ and $\Gamma_\theta = 0$. Not all equilibrium points are stable; if the magnetization is slightly perturbed from an equilibrium, it is stable only if it decays back into the equilibrium point. To find its stability, we first

evaluate the Jacobian, defined as:

$$\hat{V} = \begin{pmatrix} \partial\Gamma_\phi/\partial\phi & \partial\Gamma_\phi/\partial\theta \\ \partial\Gamma_\theta/\partial\phi & \partial\Gamma_\theta/\partial\theta \end{pmatrix}. \quad (\text{D.3})$$

This leads to the stability matrix \hat{D} as described in Ref. [122]:

$$\hat{D} = \frac{1}{1+\alpha^2} \begin{pmatrix} 1/\sin(\theta) & -\alpha/\sin(\theta) \\ -\alpha & -1 \end{pmatrix} \hat{V}. \quad (\text{D.4})$$

The eigenvalues of \hat{D} , labelled λ_1, λ_2 determine the stability of the equilibrium point. When the eigenvalues are complex conjugates, with negative real part, the equilibrium is stable. The stability boundary is therefore determined from

$$\text{Re}[\lambda_{1,2}] = 0. \quad (\text{D.5})$$

For the case considered here, we can expand to first order in H_{st}/H_d and find an explicit expression for the region of stability for the solution given by Eq. (D.5) in terms of $h = H/H_d$.

Bibliography

- [1] S. Parkin, X. Jiang, C. Kaiser, A. Panchula, K. Roche, and M. Samant. *Proceedings of IEEE*, 91:661, 2003.
- [2] S. Sanvito. *cond-mat/0503445*, 2005.
- [3] N. W. Ashcroft and N. D. Mermin. *Solid State Physics*. Brooks/Cole, 1976.
- [4] P. W. Anderson. *Science*, 177:393, 1972.
- [5] J.P. Eisenstein and A.H. MacDonald. *Nature*, 432:691, 2004.
- [6] E. Rossi, A.S. Núñez, and A.H. MacDonald. *Phys. Rev. Lett.*, 95:266804, 2005.
- [7] M. Mierzejewski and M. M. Maska. *Phys. Rev. B*, 73:205103, 2006.
- [8] Slaughter et al. *IEEE International Electron Devices Meetings*, 7.1:35, 2005.
- [9] A.S. Núñez and A.H. MacDonald. *Solid State Commun.*, 31:139, 2006.
- [10] J. M. Soler, E. Artacho, J. D. Gale, A. García, J. Junquera, P. Ordejón, and D. Sánchez-Portal. *J. Phys: Cond. Matt.*, 14:1745, 2002.
- [11] I. Žutić, J. Fabian, and S. Das Sarma. *Rev. Mod. Phys.*, 76:323, 2004.
- [12] T. McGuire and R. Potter. *Magnetics and IEEE Transactions on*, 11:1018, 1975.

- [13] T. Jungwirth, Jairo Sinova, J. Maek, J. Kucera, and A. H. MacDonald. *Rev. Mod. Phys.*, 78:809, 2006.
- [14] T. Jungwirth, Q. Niu, and A. H. MacDonald. *Phys. Rev. Lett.*, 88:207208, 2002.
- [15] Michael Fowler. http://galileoandeinstein.physics.virginia.edu/more_stuff/E&M_Hist.html.
- [16] R. Skomski and J. M. D. Coey. Institute of Physics Publishing Ltd., 1999.
- [17] T. Valet and A. Fert. *Phys. Rev. B* 48 and 7099, 48:7099, 1993.
- [18] W. H. Butler, X.-G. Zhang, T. C. Schulthess, and J. M. MacLaren. *Phys. Rev. B*, 63:054416, 2001.
- [19] K. Tsukagoshi, B. W. Alphenaar, and H. Ago. *Nature*, 401:527, 1999.
- [20] J. R. Petta, S. K. Slater, and D. C. Ralph. *Phys. Rev. Lett.*, 93:136601, 2004.
- [21] D. Waldron, P. Haney, B. Larade, A. MacDonald, and H. Guo. *Phys. Rev. Lett.*, 96:166804, 2006.
- [22] Z.H. Xiong, Di Wu, Z. Vally Vardeny, and Jing Shi. *Nature*, 427:821, 2004.
- [23] Ó Mermer et. al. *Phys. Rev. B*, 72:205202, 2005.
- [24] J. Slonczewski. *J. Magn. Magn. Mat.*, 62:123, 1996.
- [25] L. Berger. *Phys. Rev. B*, 54:9353, 1996.
- [26] M. Tsoi, A.G.M. Jansen, J. Bass, W.C. Chiang, M. Seck, V. Tsoi, and P. Wyder. *Phys. Rev. Lett.*, 81:493(E), 1998.
- [27] M. Tsoi, A.G.M. Jansen, J. Bass, W.C. Chiang, V. Tsoi, and P. Wyder. *Nature*, 406:46, 2000.

- [28] J.A. Katine, F.J. Albert, R.A. Buhrman, E.B, Myers, and D.C. Ralph. *Phys. Rev. Lett.*, 84:3149, 2000.
- [29] F.J. Albert, N.C. Emley E.B, Myers, D.C. Ralph, and R.A. Buhrman. *Phys. Rev. Lett.*, 89:226802, 2002.
- [30] M.R. Pufall, W.H. Rippard, and T.J. Silva. *App. Phys. Lett.*, 83:323, 2003.
- [31] W. H. Weiklejohn and C. P. Bean. *Phys. Rev.*, 102:1413, 1956.
- [32] H. Ohldag, A. Scholl, F. Nolting, E. Arenholz, S. Maat, A. T. Young, M. Carey, and J. Stohr. *Phys. Rev. Lett.*, 91:017203, 2003.
- [33] R. Landauer. *IBM J. Res. Develop*, 1:233, 1957.
- [34] R. Landauer. *Phil. Mag.*, 21:863, 1970.
- [35] A. D. Stone and A. Szafer. *IBM J. Res. Develop.*, 32:384, 1988.
- [36] M. Buttiker, Y. Imry, R. Landauer, and S. Pinhas. *Phys. Rev. B*, 31:6207, 1985.
- [37] A. Szafer and A. D. Stone. *Phys. Rev. Lett.*, 62:300, 1989.
- [38] H. Van Houten and C. Beenakker. *cond-mat/0512609*, 1996.
- [39] B. J. van Wees, H. van Houten, C. W. J. Beenakker, J. G. Williamson, L. P. Kouwenhoven, D. van der Marel, and C. T. Foxon. *Phys. Rev. Lett.*, 60:848, 1988.
- [40] S. Datta. *Electronic Transport in Mesoscopic Systems*. Cambridge University Press, 1995.
- [41] K. M. Schep, J. van Noof, P. J. Kelly, G. E. Bauer, and J. E. Inglesfield. *Phys. Rev. B*, 45:10805, 1997.

- [42] A. Brataas, G. E. Bauer, and P. J. Kelly. *Phys. Rep.*, 427:157, 2006.
- [43] A. Brataas, Yu. V. Nazarov, and G. E. W. Bauer. *Phys. Rev. Lett.*, 84:2481, 2000.
- [44] J. Zhang and P. M. Levy. *Phys. Rev. B*, 71:184426, 2005.
- [45] J. Schwinger. *J. Math. Phys.*, 2:402, 1961.
- [46] L. V. Keldysh. *Sov. Phys. JETP*, 20:1018, 1965.
- [47] L. Kadanoff and G. Baym. *Quantum Statistical Mechanics*. Perseus Books.
- [48] A. L. Fetter and J. D. Walecka. *Quantum Theory of Many-Particle Systems*. McGraw-Hill College, 1971.
- [49] J. W. Negele and H. Orland. *Quantum Many-Particle Systems*. Westview Press, 1998.
- [50] Piers Coleman. *The evolving monogram on Many Body Physics*.
<http://www.physics.rutgers.edu/~coleman/>.
- [51] A. Pekka-Jauho. *J. Phys.: Conference Series*, 35:313, 2006.
- [52] F. S. Khan, J. H. Davies, and J. W. Wilkins. *Phys. Rev. B*, 36:2578, 1987.
- [53] C. Caroli, R. Combescot, P. Nozieres, and D. Saint-James. *J. Phys. C*, 4:916, 1971.
- [54] J. Taylor, H. Guo, and J. Wang. *Phys. Rev. B*, 63:245407, 2001.
- [55] M. P. Lopez Sancho and J. Rubio. *J. Phys. F*, 15:851, 1975.
- [56] A. P. Jauho, N. S. Wingreen, and Y. Meir. *Phys. Rev. B*, 50:5528, 1994.
- [57] P. Hohenberg and W. Kohn. *Phys. Rev.*, 136:864, 1964.

- [58] R.G. Parr and W. Yang. *Density-Functional Theory of Atoms and Molecules*. Oxford University Press, 1989.
- [59] W. Kohn and L.J. Sham. *Phys. Rev.*, 140:1133, 1965.
- [60] R.O. Jones and O. Gunnarsson. *Rev. Mod. Phys.*, 61:689, 1989.
- [61] D. R. Hamann, M. Schluter, and C. Chiang. *Phys. Rev. Lett.*, 43:1494, 1979.
- [62] N. Troullier and José Luis Martins. *Phys. Rev. B*, 43:1993, 1991.
- [63] E. Artacho, D. Sánchez-Portal, P. Ordejón, A. García, and J. M. Soler. <http://www.uam.es/departamentos/ciencias/fismateriac/siesta/>. The Siesta and ATOM packages are available for download on this page.
- [64] L. Kleinman and D.M. Bylander. *Phys. Rev. Lett.*, 48:1425, 1982.
- [65] X. Gonze, P. Kackell, and M. Scheffler. *Phys. Rev. B*, 41:12264, 1990.
- [66] E. Anglada, J. Soler, J. Junquera, and E. Artacho. *Phys. Rev. B*, 66:205101, 2002.
- [67] E. Artacho, D. Sánchez-Portal, P. Ordejón, A. García, and J. M. Soler. *Phys. State. Sol. (b)*, 215:809, 1999.
- [68] W. H. Press, B. P. Flannery, S. A. Teukolsky, and W. T. Vetterling. *Numerical Recipes*. Cambridge University Press, 1992.
- [69] P. Pulay. *J. Comput. Chem.*, 3:556, 1982.
- [70] J. P. Perdew and Alex Zunger. *Phys. Rev. B*, 23:5048, 1981.
- [71] H. Goldstein. *Classical Mechanics*. Addison-Wesley Publishing Company and Inc., 1922.
- [72] G. S. Beach et. al. *Phys. Rev. Lett.*, 97:057203, 2006.

- [73] J. Grollier, P. Boulenc, V. Cros, A. Hamzi, A. Vaurs, A. Fert, , and G. Faini. *App. Phys. Lett.*, 83:509, 2003.
- [74] A. Yamaguchi, T. Ono, S. Nasu, K. Miyake, K. Mibu, and T. Shinjo. *Phys. Rev. Lett.*, 92:077205, 2004.
- [75] Y. B. Bazaliy, B. A. Jones, and S.-C. Zhang. *Phys. Rev. B*, 57, 1998.
- [76] J. Fernandez-Rossier, M. Braun, A. S. Nú nez, and A. H. MacDonald. *Phys. Rev. B*, 69:174412, 2004.
- [77] V. P. Antropov, M. I. Katsnelson, B. N. Harmon, M. van Schilfgaarde, and D. Kusnezov. *Phys. Rev. B*, 54:1019, 1996.
- [78] Z. Qian and G. Vignale. *Phys. Rev. Lett.*, 88:056404, 2002.
- [79] V. P. Antropov, M. I. Katsnelson, M. van Schilfgaarde, and B. N. Harmon. *Phys. Rev. Lett.*, 75:729, 1995.
- [80] Q. Niu and L. Kleinman. *Phys. Rev. Lett.*, 80:2205, 1998.
- [81] Q. Niu, X. Wang, L. Kleinman, W. Liu, D. M. C. Nicholson, and G. M. Stocks. *Phys. Rev. Lett.*, 83:207, 1999.
- [82] M. Methfessel and J. Kubler. *J. Phys. F: Met. Phys.*, 12:141, 1982.
- [83] A. I. Leichtenstein, M. I. Katsnelson, V. P. Antropov, and V. A. Gubanov. *J. Magn. Magn. Mat.*, 67:65, 1987.
- [84] M. Pajda, J. Kudrnovský, I. Turek, V. Drchal, and P. Bruno. *Phys. Rev. B*, 67:174402, 2001.
- [85] Anh Kiet Nguyen, Hans Joakim Skadsem, and Arne Brataas. *cond-mat/0606498*, 2006.

- [86] M. Di Ventura, Y. C. Chen, and T. N. Todorov. *Phys. Rev. Lett.*, 92:176803, 2004.
- [87] T. N. Todorov, J. Hoekstra, and A. P. Sutton. *Phil. Mag. B*, 421:421, 2000.
- [88] J. Kudrnovský, I. Tured, V. Drchal, F. Máca, P. Weinberger, and P. Bruno. *Phys. Rev. B*, 69:115208, 2004.
- [89] M. D. Stiles and A. Zangwill. *Phys. Rev. B*, 66:014407, 2002.
- [90] Ch. Morawe, A. Abromeit, N. Metoki, P. Sonntag, and H. Zabel. *J. Mater. Res.*, 9:570, 1994.
- [91] F. J. Lamelas, C. H. Lee, Hui He, W. Vavra, and Roy Clarke. *Phys. Rev. B*, 40:5837, 1989.
- [92] A. Hamzic J.M. George H. Jaffres J. Grollier, V. Cros and A. Fert. *App. Phys. Lett.*, 78:3663, 2001.
- [93] M. R. Pufall, W. H. Rippard, and T. J. Silave. *App. Phys. Lett.*, 83:323, 2003.
- [94] J. Mathon, A. Umerski, and M. Villeret. *Phys. Rev. B*, 55:14378, 1997.
- [95] Y. Huai, M. Pakala, Z. Diao, and Y. Ding. *App. Phys. Lett.*, 87:222510, 2005.
- [96] W. M. Lomer. *Proc. Phys. Soc. London*, 80:489, 1962.
- [97] L. Pál, E. Krén, G. Kádár, P. Szabó, and T. Tarnóczy. *J. App. Phys.*, 39:538, 1968.
- [98] A. Sakuma, K. Fukamichi, K. Sasao, and R. Y. Umetsu. *Phys. Rev. B*, 78:024420, 2003.
- [99] C.G. Shull and M.K. Wilkinson. *Rev. Mod. Phys.*, 25:100, 1953.
- [100] E. Fawcett. *Rev. Mod. Phys.*, 60:209, 1988.

- [101] O.G. Shpyrko et. al. Direct measurement of antiferromagnetic domain fluctuations. *Nature*, 447:68, 2007.
- [102] P.G. Evans, E.D. Isaacs, G. Aeppli, Z.Cai, and B. Lai. *Science*, 295:1042, 2002.
- [103] H. Zabel. *J. Phys: Condens. Matter*, 11:9303, 1999.
- [104] E.E. Fullerton, J.L. Robertson, A.R.E. Prinsloo, and S.D. Bader H.L. Alberts. *Phys. Rev. Lett.*, 91:237201, 2003.
- [105] H. Zabel. *J. Phys. Condens. Matter*, 13, 2001.
- [106] D.T. Pierce, J. Unguris, R.J. Celotta, and M.D. Stiles. *J. Magn. Magn. Mater.*, 200:290, 1999.
- [107] E.E. Fullerton, S.D. Bader, and J.L. Robertson. *Phys. Rev. Lett.*, 77:1382, 1996.
- [108] A. S. Nunez, R. A. Duine, Paul Haney, and A. H. MacDonald. *Phys. Rev. B*, 73:214426, 2006.
- [109] J. Mathon, A. Umerski, and M. Villeret. *Phys. Rev. B*, 55:14378, 1997.
- [110] V. S. Speriosu, B. Dieny, P. Humbert, B. A. Gurney, and H. Lefakis. *Phys. Rev. B*, 44:5538, 1991.
- [111] S. S. P. Parkin, R. Bhadra, and K. P. Roche. *Phys. Rev. Lett.*, 66:2152, 1991.
- [112] R. A. Duine, P. M. Haney, A. S. Nunez, and A. H. MacDonald. *Phys. Rev. B*, 75:014433, 2007.
- [113] G. Zajac, S.D. Bader, and R.J. Friddle. *Phys. Rev. B*, 31:4947, 1985.
- [114] C. L. Fu and A. J. Freeman. *Phys. Rev. B*, 313:1611, 1986.

- [115] C. L. Fu, A. J. Freeman, and T. Oguchi. *Phys. Rev. Lett.*, 54:2700, 1986.
- [116] A. W. Overhauser. *Phys. Rev.*, 128:1437, 1962.
- [117] D.G. O'Neill and J.H. Weaver. *Phys. Rev. B*, 37:8122, 1988.
- [118] R. Hafner, D. Spišák, R. Lorenz, and J. Hafner. *Phys. Rev. B*, 54:184432, 2002.
- [119] E.W. Fenton. *J.Phys. F: Met. Phys.*, 8:689, 1978.
- [120] Z. Wei, A. Sharma, A. S. Nunez, P. M. Haney, R. A. Duine, J. Bass, A. H. MacDonald, and M. Tsoi. *Phys. Rev. Lett.*, 98:116603, 2007.
- [121] T. C. Schulthess and W. H. Butler. *J. App. Phys.*, 83:7225, 1998.
- [122] Ya. B. Bazaliy, B. A. Jones, and Shou-Cheng Zhang. *Phys. Rev. B*, 69:094421, 2004.
- [123] Jiang Xiao, A. Zangwill, and M. D. Stiles. *Phys. Rev. B*, 72:014446, 2005.
- [124] J. Z. Sun. *Phys. Rev. B*, 62:570, 2000.
- [125] J. Nogués, J. Sort, V. Langlais, V. Skumryeva, J. S. Munoz S. Surinach, and M.D. Baro. *Phys. Rep.*, 422:65, 2005.
- [126] D. Seuss et al. *Phys. Rev. B*, 67:054419, 2003.
- [127] S. Ganguly, L. F. Register, S. Banerjee, and A. H. MacDonald. *Phys. Rev. B*, 71:245306, 2005.
- [128] A. Mitra, I. Aleiner, and A. J. Millis. *Phys. Rev. Lett.*, 94:076404, 2005.
- [129] L. Fernández-Seivane, M. A. Oliveira, S. Sanvito, and J. Ferrer. *J. Phys.: Condens. Matter*, 18:7999, 2006.

- [130] Xin Jiang, Li Gao, J. Z. Sun, and S. S. P. Parkin¹. *Phys. Rev. Lett.*, 97:217202, 2006.

Vita

Paul Michael was born in Columbus, Ohio on October 4th, 1976, the son of Michael and Jane Haney. He received the Bachelor of Science degree in Physics and Mathematics from the Ohio State University in May of 2000. He worked for one year at Johns Hopkins Medical Institutes, and in August of 2002 he entered the Graduate School of the University of Texas at Austin.

Permanent address: UT at Austin, Physics Department,
1 University Station,
Austin, TX 78712

This dissertation was typeset with L^AT_EX[†] by the author.

[†]L^AT_EX is a document preparation system developed by Leslie Lamport as a special version of Donald Knuth's T_EX Program.